Universität Stuttgart

Geodätisches Institut

GOCE Data and Gravity Field Model Filter Comparison

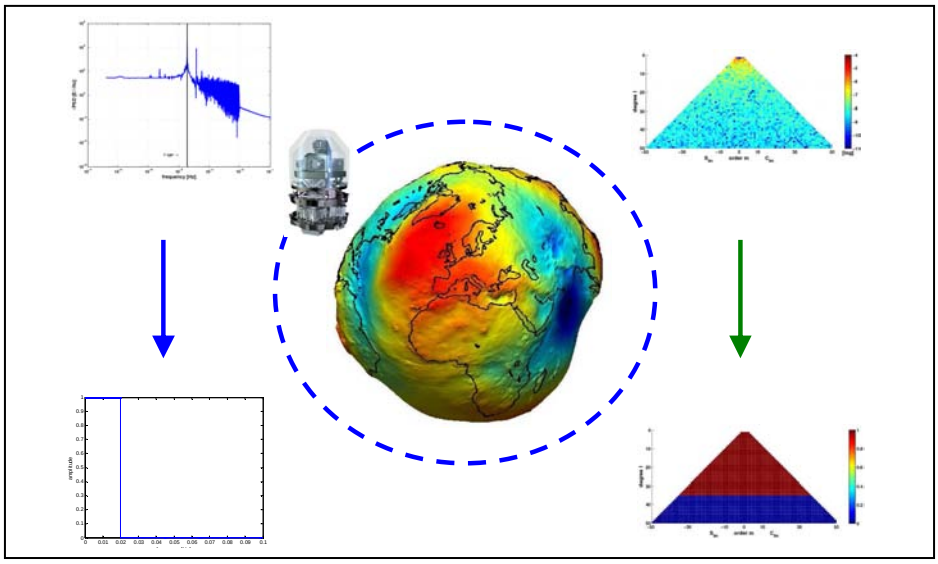

Studienarbeit im Studiengang

Geodäsie und Geoinformatik

an der Universität Stuttgart

Carina Raizner

Stuttgart, Dezember 2007

Betreuer:
Roger Haagmans
Head of Solid Earth Unit, ESA/ESTEC, Noordwijk, Niederlande

Dr.techn. Dipl.-Ing. Gernot Plank
ESA/ESTEC, Noordwijk, Niederlande

Dr.-Ing. Michael Kern
ESA/ESTEC, Noordwijk, Niederlande

Prüfer:
Prof. Dr.-Ing. Nico Sneeuw
Universität Stuttgart

Selbständigkeitserklärung

Hiermit erkläre ich, Carina Raizner, dass ich die von mir eingereichte Studienarbeit zum Thema

GOCE data and gravity field model filter comparison

selbstständig verfasst und ausschliesslich die angegebenen Hilfsmittel und Quellen verwendet habe.

Datum, Ort: _____

Unterschrift: _____

(Carina Raizner)

ABSTRACT

GOCE data and gravity field model filter comparison

New approaches with respect to space borne gravity observations are expected to significantly improve the overall knowledge of the Earth's gravity field and its geoid. The Gravity field and steady-state Ocean Circulation Explorer (GOCE) is the first Core Earth Explorer Mission of the ESA Living Planet Programme. This new satellite mission based on the concept of satellite gradiometry is designed to support applications in Earth physics, oceanography and geodesy with an accurate and detailed global model of the Earth's gravity field and its geoid.

One of the main problems in the use of the GOCE data is that the retrieval algorithms need along-track filtering on one hand and/or the implementation of spherical filters on the other. The match between these along-track one-dimensional filters and the spherical two-dimensional ones is far from obvious. Thus, the objective of this study is to investigate the influences of these two filter types by analyzing the differences between simulated GOCE reference and filtered data. Apart from closed-loop tests in order to check the consistency and correctness of the data and software used, the testing procedure for along-track as well as spherical filtering is implemented as follows. First, a global reference model is used for data generation which yields a reference signal along the orbit. By applying a one-dimensional along-track filter to these synthetic satellite data, a filtered global model is retrieved. On the other hand, the synthetic satellite data can be also generated after applying spherical filters to the global reference model. The outcome is a filtered global model estimated from these synthetic satellite data. The influences of both filter types are assessed by comparing the reference and filtered signals along the orbit as well as by comparing the reference and filtered models on the ground. Additionally, the properties of both filter types can be varied.
In order to examine the empirical relation between along-track and spherical filters, transfer functions of the filters are investigated in a second step of this study. The transfer function for the spherical filter in the model domain is the ratio between reference and filtered signal which represents a corresponding one-dimensional along-track filter in the signal domain. On the other hand, computing the ratio between reference and filtered model estimated from the along-track filtered signal relates the one-dimensional filter in the signal domain to a two-dimensional spherical filter in the model domain.

The outcome of the study will be very useful for explaining some of the differences between current global model retrieval philosophies and will also be applicable to other satellite missions and data types in the future.

Keywords:
satellite gradiometry · closed-loop tests · along-track filtering in signal domain · spherical filtering in model domain · empirical transfer functions

ZUSAMMENFASSUNG

Vergleich zwischen „along-track" und isotropen Spektralfiltern im Rahmen der GOCE–Datenprozessierung

Neue satellitengestützte Ansätze zur Beobachtung des Schwerefelds werden beträchtlich zur Verbesserung der Kenntnisse über das globale Schwerefeld der Erde und des Geoids beitragen. Der „Gravity field and steady-state Ocean Circulation Explorer" (GOCE) gehört zur ersten „Core Earth Explorer Mission" des "ESA Living Planet Programme". Diese neue Satellitenmission, die auf dem Konzept der Satellitengradiometrie basiert, wird ein genaues und detailliertes globales Model des Erdschwerefelds und des Geoids liefern, das hauptsächlich Anwendungen in der Geophysik, Ozeanographie und Geodäsie finden wird.

Eines der grundlegenden Probleme bei der Prozessierung von GOCE Daten mit verschiedenen Lösungsansätzen ist einerseits der Bedarf an „along-track" Filterung und / oder andererseits die Anwendung von isotropen Spektralfiltern. Die Beziehung zwischen diesen eindimensionalen „along-track" und den zweidimensionalen isotropen Filtern liegt nicht unmittelbar auf der Hand. Das Ziel dieser Studienarbeit ist deshalb zunächst die Untersuchung der Einflüsse der beiden Filter hinsichtlich der Differenzen zwischen simulierten Referenzdaten von GOCE und den gefilterten Daten.

Um die Konsistenz und Richtigkeit der verwendeten Daten und Software zu überprüfen, werden zunächst sogenannte closed-loop Tests durchgeführt. Im Anschluss werden verschiedenen Testverfahren für die „along-track" und die isotrope Filterung wie folgt implementiert. Der erste Schritt ist die auf einem globalen Referenzmodell basierende Generierung eines synthetischen Referenzsignals entlang des Orbits. Anschließend wird ein eindimensionaler „along-track" Filter auf dieses Signal angewandt und daraus ein gefiltertes globales Modell berechnet. Alternativ kann das synthetische Satellitensignal auch erst generiert werden, nachdem das globale Referenzmodell isotrop gefiltert wurde. Basierend auf diesem Satellitensignal wird dann ein neues gefiltertes globales Modell geschätzt. Die Einflüsse der beiden Filter können durch einen Vergleich zwischen synthetischen Referenz- und gefilterten Signalen entlang des Orbits sowie zwischen Referenz- und gefilterten Modellen beurteilt werden. Zusätzlich, können die Eigenschaften der beiden Filter variiert werden.

Im zweiten Teil dieser Arbeit werden die empirischen Transferfunktionen der Filter hergeleitet, um die empirische Relation zwischen „along-track" und isotropen Filtern zu überprüfen. Die Transferfunktion der isotropen Filter im Modellbereich kann über das Verhältnis zwischen Referenz- und gefiltertem Signal berechnet werden und entspricht einem eindimensionalen „along-track" Filter im Signalbereich. Die Herleitung des Verhältnisses zwischen Referenz- und gefiltertem Modell auf der anderen Seite, erlaubt die Herstellung eines Zusammenhangs zwischen einem ein-dimensionalen Filter im Signalbereich und einem zwei-dimensionalen Filter im Modellbereich.

Das Ergebnis dieser Studienarbeit könnte beispielsweise dazu verwendet werden, um einige Unterschiede zwischen den momentan gebräuchlichen Auswertestrategien des globalen Modells zu klären. Die vorgestellten Testverfahren könnten in Zukunft auch für andere Satellitenmissionen und Datentypen eingesetzt werden.

Schlüsselwörter:
Gradiometrie · closed-loop Tests · „along-track" Filterung im Signalbereich · isotrope Filterung im Modellbereich · empirische Transferfunktionen

PREFACE

The research for this study was carried out during an internship at ESTEC in Noordwijk, the Netherlands, from June 2007 to November 2007. In these six months, I had the unique chance to get an insight into the European Space Research and Technology Centre which is the technical heart of the European Space Agency (ESA). The objective of this practical training period was to work on a research topic with respect to the Gravity field and steady-state Ocean Circulation Explorer (GOCE). Hereby, I was attached to the Solid Earth Unit (EOP-SME) of the Mission Science Division within the Science and Applications Department which belongs to the Directorate of Earth Observation Programmes. In this professional surrounding and with the support of my supervisors, I was able to prepare this study which deals with the "GOCE data and gravity field model filter comparison".

In the first place, I want to use this opportunity to express my deepest gratitude to my supervisors, R. Haagmans, Head of the Solid Earth Unit, as well as Dr. G. Plank and Dr. M. Kern, for their help and support throughout my internship. Their patience towards my work and their continuous advices and guidance are highly appreciated. I also want to sincerely thank Dr. M. Drinkwater, Head of Mission Science Division, and Dr. Volker Liebig, Director of Earth Observation, for their efforts to make my internship at ESTEC possible. Furthermore, I would like to express my gratitude to my supervisor at the University of Stuttgart, Dr. N. Sneeuw, Head of Institute of Geodesy, for his additional comments and suggestions for improving the quality of the study.
I also wish to thank my dear friend, Dr. Matthias Weigelt. His continuous encouragement and patience to answer countless questions as well as the thorough proofreading is highly appreciated.
My stay abroad in the Netherlands was financially supported by the "Verein der Freunde des Studiengangs Geodäsie und Geoinformatik der Universität Stuttgart". I want to express my gratitude to the chairman A. Hils and the members.
Without my colleagues in the Mission Science Division and without all my friends among the Young Graduate Trainees and back home in Stuttgart, the stay at ESTEC had not been the same. Thank you very much for your constant support, your understanding and the good times.

Last but not least, I am very thankful to my dear parents, my sister and my brother. Without their unceasing love, encouragement, support and faith in me, I could not have done it.

List of Tables

List of Figures

Table Of Contents

1 INTRODUCTION

The global Earth's gravity field and its geoid are the key components in the investigation of structure and dynamics of the Earth's interior system. The determination of a highly accurate gravity field with high spatial resolution contributes in answering many theoretical and practical problems which appear in the following applications:

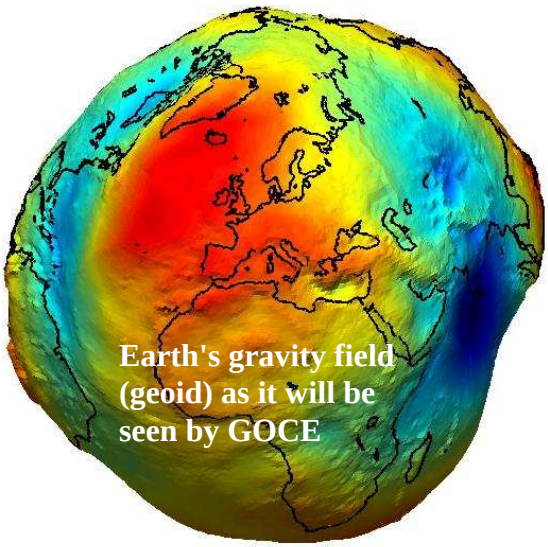

Solid-Earth Physics:
Physics of the interior structure of the Earth

Oceanography
Dynamics of the oceans with respect to absolute ocean circulation and interactions of continents, ice and ocean in sea-level

Geodesy
Precise orbit determination and unification of height systems

Satellites provide the means to obtain a global and homogeneous gravity field within a reasonable time period. As before other satellite gravity observation missions such as CHAMP and GRACE, the Gravity Field and Steady-State Ocean Circulation Explorer (GOCE) will provide a global model of the Earth's gravity field and of its geoid on a global scale. The geoid (the surface of equal gravitational potential of a hypothetical ocean at rest) serves as the classical reference for all topographical features. The objective of these new missions is to use specific observation techniques in order to improve the geoid in terms of spatial resolution and accuracy. The main drawback of such a space mission, so far, is the attenuation of the gravity field at satellite altitude. The driving innovation of GOCE will be a gradiometer which counteracts the attenuation effect by measuring the second derivatives of the Earth's gravitational potential, the so-called gravity gradients. The attenuation effect can be seen as applying a "lowpass" filter to the gravitational potential on the ground and can be reversed by applying a "differentiator" to the signal measured at satellite altitude.

There are mainly two approaches to determine an approximation of the Earth's gravitational field in terms of spherical harmonics from satellite gradiometry (Rummel et al., 1993):

- In the *time-wise approach*, the gravitational field estimation is based on the solution of the equations of motion by linear least-squares adjustment whereas the measurements are viewed as a discrete time series.
- The *space-wise approach* solves the gravitational field by means of a geodetic boundary value problem related to the Earth's surface. The measurements are considered as only being dependent on the position and they are interpolated into a regular grid on a reference sphere beforehand.

In both approaches, the measurements need to be modified in certain ways. For example, in the space-wise approach the measurements need to be interpolated on a regular grid which yields a loss of information due to the smoothing property of the interpolation. It is comparable to the application of a lowpass filter to the data set. Consequently and in general, the usage of one particular retrieval algorithm will result in an inherent modification of the data. The same effect can be simulated by either along-track filtering of a one-dimensional signal or by a spherical filter in the spectral domain and thus the relation can be better understood by investigating such filters. However, the connection between one-dimensional along-track and two-dimensional spherical filters is far from obvious.

Thus, the objective of this study is to investigate the influences of these two filter types by analysing the differences between simulated GOCE reference and filtered data. Before the filters can be investigated, a closed-loop simulation forms the computational framework of this work. Naturally, it needs to be assured that the closed-loop errors lie within the numerical accuracy of the computer. The first task is the application of one-dimensional along-track filters to a time series of synthetic gradiometer data and the assessment of its influence on the time series itself and on the corresponding spherical harmonic spectrum. Similarly, the effects of a spherical filter in the spectral domain need to be investigated. Additionally, the properties of both filter types can be varied. The final task is the direct relation of both filter types which is theoretically possible in an analytical way but practically tedious. Therefore, in an attempt to bypass these difficulties the link is established by empirical transfer functions, instead.

The study is organized in the following way:

- **Background:** Section 2 provides a short overview of the mathematical description of the Earth's gravitational field and will introduce the most important aspects about the Gravity Field and Steady-State Ocean Circulation Explorer (GOCE) mission. In order to understand the different effects caused by the filters, the basics of along-track and spherical filtering will also be explained shortly with respect to two different filter types which are the ideal boxcar and the Butterworth filter.

- **Testing procedures:** After describing the software and the input dataset, the actual implementation of the closed-loop, along-track filtering and spherical filtering tests is shown by means of flowcharts. The explanation of the empirical connection of the transfer functions for along-track and spherical filtering will be also part of section 3.

- **Discussion of Results:** Finally, the results of the implemented filters will be analysed with respect to various quantities in section 4. These include the square rooted power spectral density (PSD) estimates of the filtered signal compared to those of the reference signal. The differences between filtered and original data with respect to spherical harmonics and other quantities such as geoid heights, gravity anomalies and gravity gradients, will be also investigated. The comparison between the different filters is based on different aspects as for example the varying effects if using different filter types applied to along-track, cross-track or radial signal components or if changing the filter cut-off frequencies or degrees. The most revealing results are shown in section 4. For completeness, the interested reader can find difference plots of all kinds of different test scenarios in the appendix.
  The second part of section 4 deals with the derivation of filter transfer functions in order to examine the relation between along-track and spherical filters empirically. In the case of along-track filtering, computing the proportion between reference and filtered spherical harmonic coefficients leads to the corresponding spherical filter transfer function. For spherical filtering, it is the other way round. The relation between reference and filtered time series represents the along-track filter transfer function due to applying a spherical filter.

2 BACKGROUND

2.1 Theory and mathematical background

As already mentioned in the introduction, the Earth's gravity field is one of the most important sources of information needed for the determination of the structure and dynamics of the Earth. Consequently, scientists aim to derive models for the global gravity field which are as accurate as possible. This section gives an overview of the mathematical background of gravity field determination. For more details, the reader is referred to Hofmann-Wellenhof and Moritz (2005).

The quantity describing the global gravity field is the gravity potential W which is the sum of the gravitational potential V due to the gravity of all masses and the centrifugal potential Z due to Earth rotation:

$$W = V + Z \tag{2.1}$$

Here, the more dominant gravitational potential [m^2/s^2] is of main interest. It can be represented by a spherical harmonic (SH) series (Hofmann-Wellenhof and Moritz, 2005):

$$V(r,\theta,\lambda) = \frac{GM}{R}\sum_{\ell=0}^{\infty}\left(\frac{R}{r}\right)^{\ell+1}\sum_{m=0}^{\ell}\bar{P}_{\ell m}(\cos\theta)\left(\bar{C}_{\ell m}\cos m\lambda + \bar{S}_{\ell m}\sin m\lambda\right) \tag{2.2}$$

where the spherical coordinates of the spacecraft in satellite applications are θ, λ and $r = R+h$ with the satellite altitude h, GM the gravitational constant (G) times mass (M) of the Earth with its mean radius R, $\bar{P}_{\ell m}$ the normalized Legendre function and $\bar{C}_{\ell m}$ and $\bar{S}_{\ell m}$ the dimensionless spherical harmonic (SH) coefficients. The first summation runs from the zero degree ℓ to infinity but is usually truncated at the maximum resolvable degree $\ell = L_{max}$. This degree corresponds approximately to the spatial resolution of $D[km] = 20000/L_{max}$ half-wavelength in kilometres.
The second summation runs from a zero order m up to the actual degree ℓ which means that $m \le \ell$.

Let us assume that the SH coefficients $\bar{C}_{\ell m}$ and $\bar{S}_{\ell m}$ are known. Then the gravitational potential V can be computed by Eq. (2.2), which is generally referred to as *spherical harmonic synthesis*. Other gravity quantities can be derived by small variations of this equation, such as taking derivatives for instance. These gravity functions include the geoid heights N (measured in metres above the reference ellipsoid), the gravity anomalies Δg (measured in milligal, where $1mGal = 10^{-5} m/s^2$) as well as the second-order derivatives of the gravitational potential with respect to three spatial directions, also known as gravitational gradients (measured in Eötvös, where $1E = 10^{-9} s^{-2}$).

In reality, the coefficients up to degree and order L_{max} of the spherical harmonic series are the fundamental gravity unknowns. Their determination is based on the satellite measurements of the gravitational potential along the orbit. The SH coefficients can be derived by a *spherical harmonic analysis*:

$$\left.\begin{matrix}\bar{C}_{\ell m}\\ \bar{S}_{\ell m}\end{matrix}\right\} = \frac{1}{4\pi}\int_{\theta=0}^{\pi}\int_{\lambda=0}^{2\pi} V(\theta,\lambda,r)\bar{P}_{\ell m}(\cos\theta)\left\{\begin{matrix}\cos m\lambda\\ \sin m\lambda\end{matrix}\right\}\sin\theta d\lambda d\theta \qquad (2.3)$$

For the sake of better visualization, it is common to represent the SH coefficients $\bar{C}_{\ell m}$ and $\bar{S}_{\ell m}$ in the form of a triangle (Figure 2.1) where the vertical axis of the triangle represents the degrees ℓ of the SH coefficients (or the corresponding spatial resolution *D*). The horizontal axis refers to the order $m \le \ell$ with the cosine $\bar{C}_{\ell m}$ coefficients on the right and the sine $\bar{S}_{\ell m}$ coefficients on the left side. Coefficients of order zero are called zonal harmonics, those of same degree and order $\ell = m$ sectorial harmonics and all the other coefficients tesseral harmonics. The colour code of the triangles refers normally to the logarithm of the absolute coefficients.

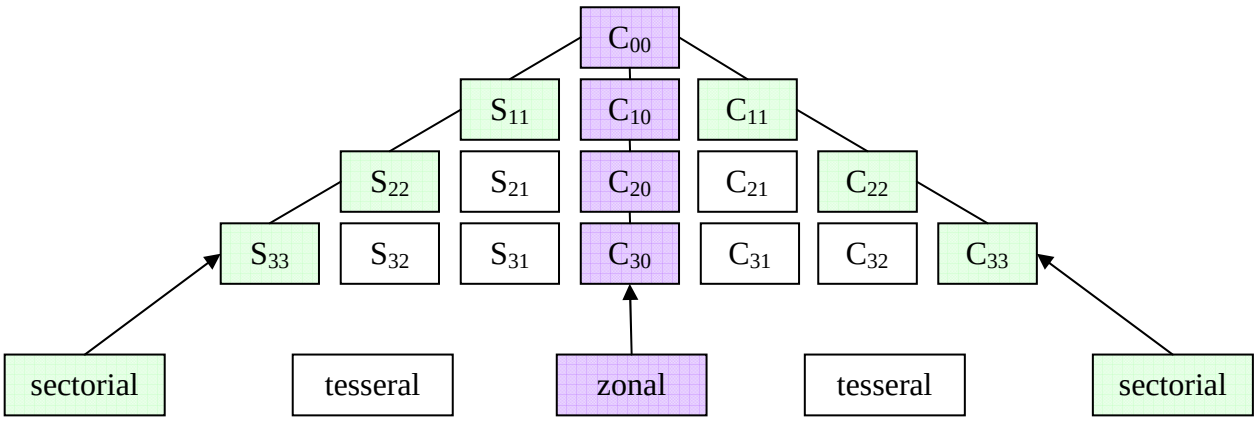

Figure 2.1: Triangular representation of SH coefficients

One of the limits in the resolution of these models is the field attenuation with increasing altitudes *h* of the satellite, expressed by the attenuation factor $\left(R/R+h\right)^{\ell+1}$ in Eq. (2.2).

This effect can be counteracted on the one hand by using an orbit as low as possible and on the other hand by the principle of gradiometry which does not measure the gravitational potential itself or its gradient but rather its second-order derivatives $\partial^2 V/\partial x_i \partial x_j$ in along-track, cross-track and radial direction. The resulting outcomes are nine gravitational gradients which can be arranged in a second-rank 3x3 signal tensor:

$$\Gamma_{ij} = \begin{bmatrix} V_{xx} & V_{xy} & V_{xz} \\ V_{yx} & V_{yy} & V_{yz} \\ V_{zx} & V_{zy} & V_{zz} \end{bmatrix} \qquad \text{for } i = \{x,y,z\} \wedge j = \{x,y,z\} \qquad (2.4)$$

This matrix is symmetrical and due to the Laplace equation, the trace must sum to zero, i.e., $V_{xx} + V_{yy} + V_{zz} = 0$.

A 'differentiation factor' caused by the differentiation counteracts the attenuation factor caused by the satellite altitude. This relation is visualized in the following mathematical scheme (Figure 2.2), the so-called Meissl scheme (Rummel and van Gelderen, 1995), which shows the three fundamental gravity quantities. These are the geoid, the gravity anomaly and the gravity gradient measurements. They are presented as potential V_ℓ, its first $\partial_r V_\ell$ and second-order $\partial^2_{rr} V_\ell$ derivatives dependent on the degree ℓ of the spherical harmonic coefficients. At satellite altitude, all three quantities are dampened by the attenuation factor $(R/r)^\ell$ which can be counteracted by a factor $(\ell+1)(\ell+2)$ by measuring gravity gradients.

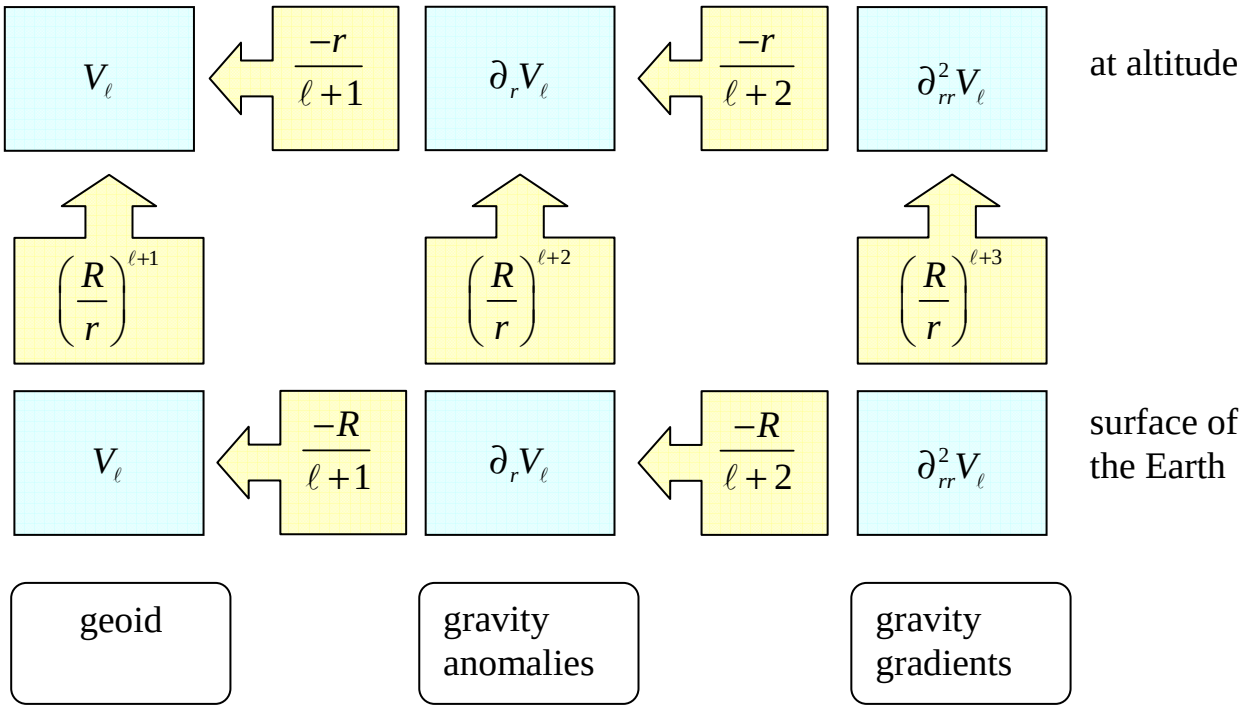

Figure 2.2: Relationship between satellite altitude and derivatives of gravitational potential *V (ESA, 1999)*

More details on the principles of satellite gradiometry are given in ESA (1999) and Hofmann-Wellenhof and Moritz (2005).

2.2 GOCE – Gravity Field and Steady-State Ocean Circulation Explorer

Satellite gradiometry is the primary measurement principles of the Gravity Field and Steady-State Ocean Circulation Explorer (GOCE) which is planned to be launched in May 2008. As this report deals with the GOCE signal, i.e., the second order derivatives of the gravitational potential, the most important aspects of this mission will be explained in section 2.2.2 after providing a short overview of the new satellite gravity missions and their mission concepts (section 2.2.1).

2.2.1 OVERVIEW OF NEW SATELLITE GRAVITY MISSIONS

In the context of the accurate determination of the Earth's gravity field, the two other gravity field satellite missions preceding GOCE should not fall into oblivion. They are currently operational in space and have already provided significantly improved gravity models. It should be noticed that each of the three missions is based on different innovative measurement concepts (Hofmann-Wellenhof and Moritz, 2005).

- **CHAMP (Challenging Minisatellite Payload):**
  This German satellite, operating since 2000, utilizes the measurement concept of satellite-to-satellite tracking in high-low mode (SST-hl). The low Earth orbiting (LEO) satellite CHAMP at an altitude of approximately *400km* is continuously tracked by the high GPS satellites. Additionally, the included accelerometer in the LEO satellite measures three-dimensional perturbing but non-gravitational accelerations along the orbit. This principle can be considered as 'in-situ' determination of 3-D positions, velocities and accelerations of a LEO and allows to accurately determine the long-wavelength features of the static Earth gravity field. Significant improvements were made for example in the polar regions which were difficult to access prior to CHAMP. For more information, the reader is referred to *http://op.gfz-potsdam.de/champ*.

- **GRACE (Gravity Recovery and Climate Experiment):**
  This US-German mission, launched in 2002, is based on the satellite-to-satellite tracking concept in low-low mode (SST-ll). Placing GRACE twin satellites in the same LEO orbit (ca. *400km* altitude) and ca. *220km* apart from each other, the concept of line-of-sight measurement of range, range rate and range acceleration between two low-orbiting satellites is realized. The satellite positions are determined by the GPS. Ranges and range rates are influenced by gravity field variations and can be measured very accurately. In combination, this leads to differences of the accelerations over a long baseline. Additionally, micro accelerometers are situated in the centre of mass of each satellite, they measure only non-gravitational accelerations on the satellites caused by e.g. air drag or solar radiation pressure. GRACE provides temporal gravity variations, such as monthly changes in the gravity field, as well as a global high-resolution gravity field of the Earth with high accuracy features for a scale of about *600–1000km*. More information is provided at *http://op.gfz-potsdam.de/grace*.

- **GOCE (Gravity Field and Steady-State Ocean Circulation Explorer):**
  The satellite of this planned ESA mission is expected to measure highly accurate, high spatial resolution gravity gradients in three dimensions. It is based on the principle of satellite gravity gradiometry (SGG) which is an analysis of the differences in gravitational acceleration between pairs of proof masses of an ensemble of six accelerometers inside the GOCE satellite. This concept is in fact very similar to the low-low-mode of satellite-to-satellite tracking. While the measurements of GRACE take place between two LEO satellites divided by a long baseline of about *220km*, the GOCE gradiometer instrument measures gravitational and rotational acceleration differences in 3D between accelerometer units within one single satellite only *±50cm* centimetres apart. The measured signal is caused by the attracting masses of the Earth which are spatially varying due to the relative distribution of oceans, land and ice, ocean mass exchange by circulation, mountains and valleys, or via ocean ridges, subduction zones, mantle inhomogeneities as well as core-mantle boundary. Since non-gravitational accelerations affect all accelerometers of one satellite in the same way, they can ideally be neglected by taking

differences between two accelerometers along one baseline. Combined with high-low satellite-to-satellite tracking (SST-hl), GOCE gradiometry will lead to high-resolution global and regional models of the Earth's static gravity field improving spatial scales down to the order of *200km*. The concept is depicted in Figure 2.3.

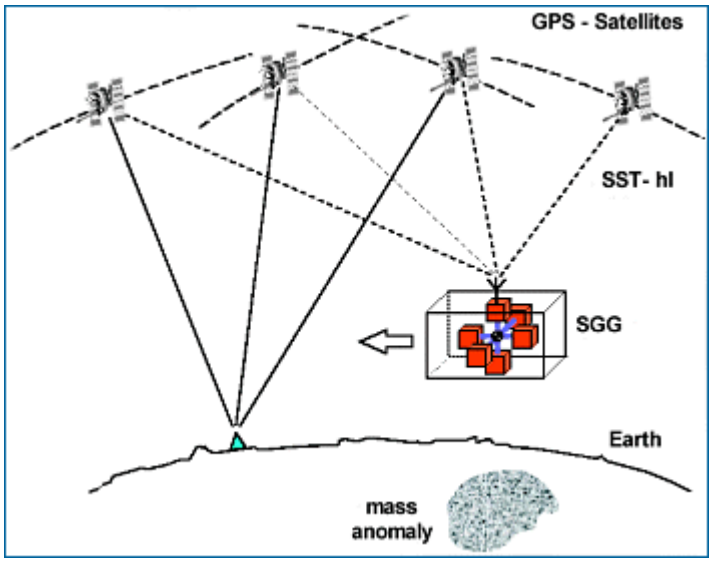

Figure 2.3: Satellite gravity gradiometry (SGG) with a three-axis gradiometer (*http://www.ife.uni-hannover.de*)

In conclusion, the development of the satellite gravity mission concepts reaches from the first derivative of the gravitational potential (CHAMP) over the difference of first derivatives over a long baseline (GRACE) to the second-order derivatives (GOCE). This development implies an improvement of the accuracy for GOCE at medium and smaller scales of the Earth's gravity field. The essential factor hereby is the decreasing distance between the test masses within the accelerometers which is "almost" zero for GOCE. Other advantages of GOCE compared to CHAMP and GRACE are the stronger signal due to the very low-earth orbit (*~250km*) and the reduced attenuation effect by applying the concept of satellite gradiometry.

2.2.2 GOCE MISSION

The Gravity Field and Steady-State Ocean Circulation Explorer (GOCE) was selected in 1999 as the first Core Earth Explorer Mission of the ESA Living Planet Programme and is planned to be launched in spring 2008. After the explanation of the mission concept of GOCE which is satellite gradiometry, this section will provide some further details of the GOCE mission. This information has been extracted from several sources such as ESA (1999), Johannessen et al. (2003), ESA (2006), Drinkwater et al. (2007) and for the cutting-edge information from the mission website *http://www.esa.int/livingplanet/goce*. Table 2.1 summarizes the key aspects of the GOCE mission.

Table 2.1: Overview of the GOCE mission (*http://www.esa.int/livingplanet/goce*)

GOCE	Mission overview
Mission Duration	2 years
Launch	2008
Orbit	Sun-synchronous, dawn-dusk
- altitude (mean)	~ 250km
- inclination	96.5°
Ground Segment	Kiruna: commands and acquisition
	ESOC: flight control
Payload	Gradiometer: 3 pairs of 3-axis, servo controlled, capacitive accelerometers.
	GPS receiver with geodetic quality
Launcher	Rockot (1000 kg payload in SSO)
Budgets	Mass: ~1000kg
	Electric power demand: 760W
Lifetime	20 months nominal; 30 months extended
Operation	Continuous data take in eclipse-free cycles; hibernation in long-eclipse season

Science Objectives

As already mentioned in the introduction, the improvement of the knowledge about the Earth's gravity field and the corresponding geoid (reference equipotential surface) in accuracy and spatial resolution will give a better insight into the physics of the Earth's interior and the interaction between continental plates. The reason is that gravity is directly linked to the mass distribution within the Earth. Furthermore, it will also lead to a better understanding of sea-level change and of the ocean circulation which plays an important role in energy exchanges around the globe. Another objective is the global unification of height systems which enables the direct comparison of mountain ranges on one continent against those on others and the usage of GPS levelling. This will be realized by using 'pseudo levelled' or orthometric heights referenced to a common GOCE-derived geoid. Thus, the mission goal is mainly the significant improvement in solid-earth physics, oceanography and geodetic applications of the data.

Mission Objectives

In order to enable the compliance of the science objectives, gravity anomalies and geoid heights will be derived from the measurements. They have to fulfill the following mission requirements:

- Earth's gravity field anomalies with an accuracy of better than *1 mGal*
- Geoid (i.e., equipotential surface of a hypothetical ocean at rest) with a radial accuracy better than *1-2 cm*
- Gravity anomalies and geoid heights with a spatial resolution of *100 km* or less (i.e., maximal degree and order of the spherical harmonic coefficients of at least 200 and higher)

Mission Elements

The advanced gravity mission GOCE is designed as a 'gravity measuring device'. This means that the satellite platform and the instrument payload (system of sensors and control elements) work as a unity which guarantees a stable thermal environment for the gradiometer. The mission consists of the GOCE satellite and three main payload instruments:

- Spacecraft (S/C):
  single rigid octagonal spacecraft which is ca. *5m* long and *1m* in diameter with fixed solar wings and no moving parts, cross-section minimised in direction of flight to reduce drag, tail fins for passive stability, solar-illuminated side of spacecraft covered with solar cells

- Electrostatic Gravity Gradiometer (EGG):
  3 pairs of 3-axis, servo-controlled, capacitive accelerometers on an ultra-stable carbon-carbon structure, each pair forms 'gradiometer arm' separated by a baseline of approximately *0.5m* and mounted orthogonal to one another, nominal alignment of gradiometer arms in along-track, cross-track and radial direction (pointing towards Earth's centre), forming a right-handed triad

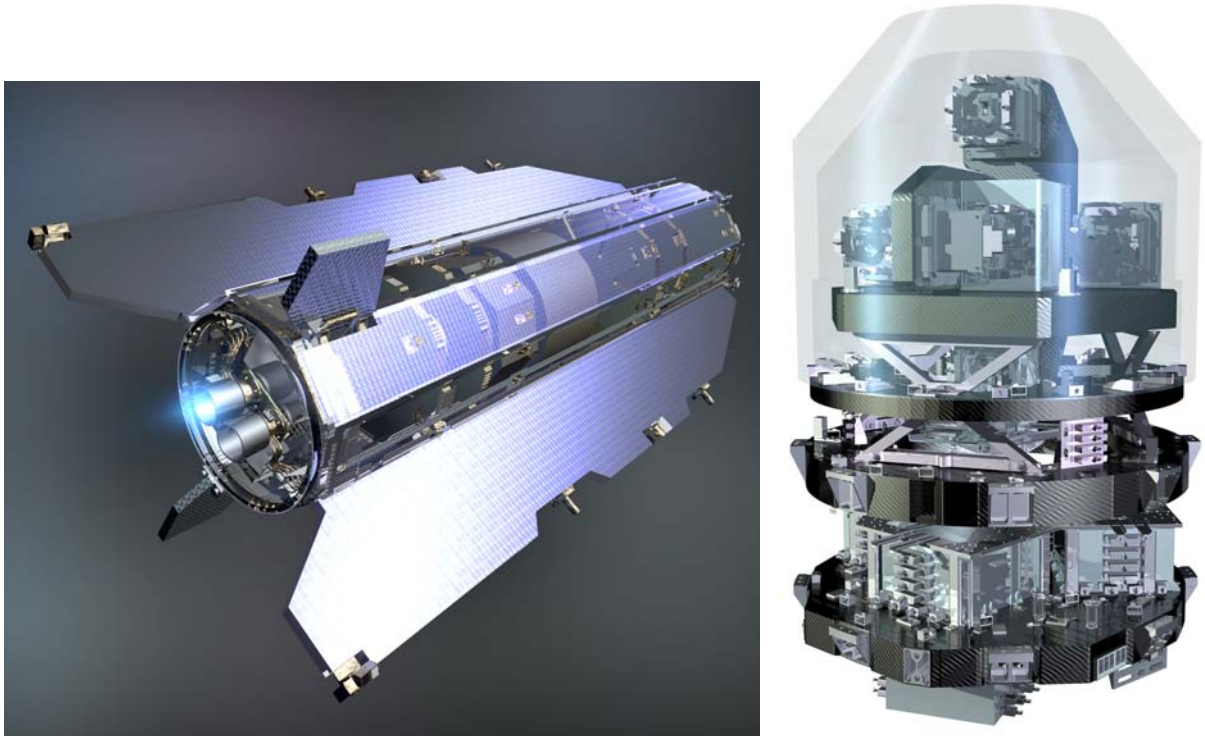

Figure 2.4: Artist's impression of the GOCE satellite (left) and Electrostatic Gravity Gradiometer instrument without harness (right) (*http://www.esa.int/livingplanet/goce*)

- Satellite-to-Satellite Tracking Instrument (SSTI):
  12-channel dual-frequency GPS receiver with dual zenith-pointing quadrifilar helix antennas, providing geodetic quality *(~1cm*) orbit determination, used for real-time on-board navigation and attitude-reference-frame determination

- Laser Retro-reflector (LRR):
  Corner-cube array acquiring satellite laser ranging (SLR) observations by existing ground-based laser network in order to support precise orbit determination by post-processing

Mission Profile

The launch of GOCE is planned on a Rockot vehicle from the Eurockot Cosmodrome in Plesetsk, northern Russia, in spring 2008. The nominal mission duration is stated as 20 months. First, the spacecraft will be injected into an orbit of about *265 km* altitude. As the fixed solar panels must face the sun, the launch orbit configuration depends on the seasonal window. Up to now, a winter launch configuration is expected which corresponds to a dawn-dusk orbit with a 6:00 hrs equatorial ascending node crossing. During the early orbit phase, global coverage outside the polar caps can be reached after about 30-40 days in this orbit. Moreover, the reference orbit configuration assures a ground track repeat period exceeding 60 days. Before reaching the operating orbit with a measurement altitude of around *250km* and an inclination of close to *96.5°*, the spacecraft is slowly decreasing its altitude. This controlled decay of about three months is used for an initial estimated commissioning of the spacecraft as well as the set-up and calibration of the gradiometer. The actual data acquisition with the assumed nominal instrument performance takes place during eclipse-free science measurement operation cycles. These phases may be separated by a long-eclipse hibernation period of around five months duration as the satellite is in Earth shadow for over 25 minutes of each orbit.

Data Products

In order to exchange commands with the satellite and acquire data via downlink, the GOCE mission makes use of a single ground station in Kiruna, Sweden. Flight control and continuous monitoring of health status and performance of the platform and the instruments, however, is undertaken by the Flight Operation Segment (FOS) via ESA-ESOC in Darmstadt, Germany. The ground station will provide the GOCE data to the Payload Data Segment (PDS) which will generate scientific Level 1b products of the GOCE mission. Furthermore, the European GOCE Gravity Consortium (EGG-C), i.e., a group of 10 European Institutes, developed a distributed processing chain called High-Level Processing Facility (HPF) which will finally provide the following Level 2 data products to approved and registered users. These Level 2 data include:

- Externally calibrated and corrected gravity gradients
- Precise science orbit solutions
- Global Earth gravity potential modelled as spherical harmonic series of minimal degree and order 200 (i.e., *100 km* spatial resolution) including coefficients and error estimates
- Geoid heights, gravity anomalies and geoid slopes (global ground-referenced and gridded)
- Variance-covariance matrix of final Earth gravity field model provided by GOCE.

2.3 Lowpass filter functions

In order to derive different data products, GOCE data will be processed with different algorithms which usually implies that the data will be also filtered in some way. The problem, however, is that

specific filters have to be applied according to the type of the data and that varying kinds of filters will also have different influences on the resulting data products. On the one hand, directly filtering the signals received from the satellite observations along the orbit requires the so-called along-track filtering. Spherical filters, on the other hand, are implemented in order to filter the resulting models if represented as spherical harmonic series. The relationship between these one-dimensional along track filters and the two-dimensional spherical ones as well as the match of their outcomes is far from obvious. Thus, the objective of this study report is to investigate how both filter types will affect the simulated GOCE signal and the resulting models. Furthermore, it will be tried to empirically examine their relation. As this work applies along-track and spherical lowpass filters with different designs, the next sections will give a short introduction into filter theory where the main information is extracted from Lynn (1982), Press et al. (1992), Oppenheim and Schafer (1999), Ingle and Proakis (2000) and Zenner (2006).

2.3.1 1D SIGNAL SLONG-TRACK FILTERING

The nine second-order derivatives of the gravitational potential form the simulated GOCE signal which can be arranged in a 3x3 gravitational gradient tensor (Eq. 2.4). Since each of the nine gradients presents a discrete one-dimensional time series of the signal along the orbit, along-track filtering can be applied. This report concentrates on filtering the three main diagonal components of the gradient tensor in along-track V_{xx}, cross-track V_{yy} and radial direction V_{zz}.

Let us assume that we have a discrete-time signal x with an integer number of N samples which is mathematical represented as a sequence of numbers in the time domain:

$$x = \{x[n]\}, \qquad -N/2 \le n \le N/2 \tag{2.5}$$

As the sequence was created by equidistant sampling of the continuous analogue and non-periodic GOCE signal, the numeric value of the *n-th* number in the sequence x is equal to the value of the analogue signal, $x_a(t)$, at time $n\Delta t$:

$$x[n] = x_a(n\Delta t), \quad -N/2 \le n \le N/2 \tag{2.6}$$

where Δt is the sampling period, i.e., the time interval between consecutive samples. Its reciprocal is called sampling frequency or rate and is given in samples recorded per second corresponding to Hertz (*Hz*):

$$f_s = \frac{1}{\Delta t} \tag{2.7}$$

The total length T in seconds of a finite time series can be computed by multiplication of the sampling period Δt times the total number of samples N. Its reciprocal is called fundamental frequency in *Hz* and is the lowest frequency which can be reached by a signal:

$$f_0 = \frac{1}{T} = \frac{1}{N\Delta t} \tag{2.8}$$

Another special type of frequency which can be computed with respect to any sampling interval Δt is the so-called Nyquist frequency:

$$f_{Ny} = \frac{1}{2\Delta t} = \frac{f_s}{2} \tag{2.9}$$

according to the Nyquist sampling theorem of Shannon. This theorem states that the maximum frequency f_{max} in the observation signal which can be accurately represented must be smaller than the Nyquist frequency, i.e., less than one-half of the sampling frequency:

$$f_{max} < f_{Ny} = \frac{1}{2\Delta t} \tag{2.10}$$

or the sampling interval must be:

$$\Delta t < \frac{1}{2 f_{max}} \tag{2.11}$$

If this theorem is fulfilled, the data are correctly sampled without aliasing error which is a folding of the signal from beyond the Nyquist frequency. This error could map into any other frequency inherent in the signal. Therefore, the prevention of aliasing is especially important if the sampling of the signal is chosen.

Instead of representing a signal as a time series in the time domain, it can be also represented as a spectrum in the spectral or frequency domain. A spectrum shows the discrete Fourier transforms (DFT) of the signal at discrete frequencies with an equal spacing of $1/(N\Delta t)$ reaching from the fundamental frequency f_0 to the Nyquist frequency f_{Ny}. The DFT is a Fourier representation of the finite-duration sequence x. As this time series is sampled with a fixed number of N values, maximal $K=N$ values of DFTs can be computed for the spectrum. Thus, the discrete sequence of the sampled signal can be transformed from the time into the spectral domain by applying the discrete Fourier transformation, given by:

$$X[k] = \sum_{n=0}^{N-1} x[n] \exp^{(-i2\pi kn)/N} \qquad -N/2 \le n, k \le N/2 \tag{2.12}$$

and vice versa by applying the inverse DFT denoted as follows:

$$x[n] = \frac{1}{N} \sum_{k=0}^{N-1} X[k] \exp^{(i2\pi kn)/N} \qquad -N/2 \le n, k \le N/2 \tag{2.13}$$

where *x[n]* is the *n-th* value sampled from the signal in the time domain and *X[k]* is the *k-th* spectral value of the sequence in the frequency domain.
As the GOCE signal is considered to be a real function, its spectrum is symmetric to zero with *X[k]=X[-k]*. Therefore, it only has to be determined for $0 \le k \le N/2$. In order to compute the DFT as fast and efficient as possible, the Fast Fourier Transformation (FFT) was applied which is also implemented in MATLAB. The speed-up compared to the direct transformation is due to avoiding the multiple computations of terms which are nullifying each other.

In the sequel, the simulated GOCE signals will be interpreted with respect to the square root of the power spectral density (PSD) estimates. The PSD measures the distribution of signal power (variance) of a time series over frequency domain. Mathematically, it is defined as the Fourier Transform of the autocorrelation sequence of the time series. Usually, the PSD is normalized by a proper constant term, denoted as *c* in the following. There are, however, several different conventions of normalizations. In general, the measure of the *k-th* amplitude of the PSD estimates and the squared amplitude of the DFTs $|X[k]|$ are proportional to each other:

$$PSD_k = \frac{|X[k]|^2}{c} \qquad -N/2 \le k \le N/2 \tag{2.14}$$

The method of PSD which will be used in this study is the simple version of an estimator called periodogram. In this case, the PSD is normalized by the sampling frequency with $c=f_s$. An implementation of this PSD estimator can be found in the function `periodogram.m` which is part of the MATLAB Signal Processing Toolbox. The PSD of the GOCE signal is given in power of Eötvös per Hertz (E^2/Hz). In general, it is much more convenient to interpret a spectrum given in the unit of $E/\sqrt{Hz}$. Thus, the square root of the PSDs will be plotted instead for further investigation purposes.

The implementation of many mathematical operations, such as filtering or convolution for example, can be realized much easier and with less computational effort in the spectral domain. Convolution is one of the elementary mathematical operators in signal processing which takes the corresponding values of two sequences *x[n]* and *h[n]* and produces a third sequence *y[n]* that, in a sense, represents the amount of overlap between *x[n]* and a reversed and translated version of *h[n]*:

$$y[n] = x[n] * h[n] = \sum_{k=-\infty}^{\infty} x[k]h[n-k] \tag{2.15}$$

In this context, the convolution theorem has to be mentioned. This theorem states that the convolution in the time domain corresponds to the multiplication in the frequency domain and vice versa:

$$x[n] * h[n] \Leftrightarrow X[k] \cdot H[k] \tag{2.16}$$

The simple transform pair shows that the Fourier transform of the convolution *x[n]*h[n]* is just the product of the individual Fourier transforms *X[k]* and *H[k]*.

If *x[n]* is considered as one sample of a signal sequence with its corresponding DFT value *X[k]* and if *H[k]* is representing one sample of a random filter designed in the spectral domain with the corresponding IDFT sample *h[n]*, the convolution theorem in Eq.(2.16) allows two rather distinct ways of filtering sampled one-dimensional signals:

- filtering time series in time domain by convolution of signal sequence samples *x[n]* with IDFT sequence samples *h[n]* of the spectral filter:

$$y[n] = x[n] * h[n] \tag{2.17}$$

- filtering the DFT of the signal in spectral domain by direct multiplication of signal DFT samples *X[k]* with spectral filter samples *H[k]*:

$$Y[k] = X[k] \cdot H[k] \tag{2.18}$$

Both filter implementations will affect the original signal and its spectrum in exactly the same way and will lead to the filtered signal samples *y[n]* in the time domain and its corresponding DFT samples *Y[k]* in the spectral domain. Thus, digital filtering in the spectral domain can be facilitated to a simple multiplication of signal DFTs and the filter due to the convolution theorem. Along-track filtering of the simulated GOCE signal will be always performed in the spectral domain in the sequel of this work. In this case, filtering can be seen as a form of weighting the signal spectrum with a factor $|H[k]|$. If modern computers are used, filtering in the spectral domain is very efficient for a long series of data and also much faster than filtering in the time domain. Furthermore, as the purpose of filtering is to modify the spectrum of the original signal, it is much more convenient and flexible to design the desired filter spectrum in the spectral domain.

According to the filter gain $|H[k]|$ which specifies the amplitude of the filter for each specific frequency sample, there are basically four different kinds of filters:

- lowpass filter: low frequency part of the signal passes the filter and high frequency part(noise) is attenuated
- highpass filter: high frequency part of the signal passes the filter and low frequency part is attenuated
- bandpass filter: specified frequency range of the signal passes the filter
- bandstop filter: specified frequency range of the signal is rejected

The amplitude spectra of these filters are visualized as amplitudes versus frequencies in Figure 2.5 where f_c, $f_{c1}$and f_{c2} specify the different cut-off frequencies.

In the sequel, all tests are performed by applying lowpass filters as this is the most common form of filtering in signal processing in order to reduce high-frequency noise but might be also inherent in the data processing itself, e.g., the interpolation in the torus approach. There are several different designs of spectral filters such as the boxcar, the Butterworth, the Gaussian, the Chebyshev, the Elliptic filters, just to name a few of them.

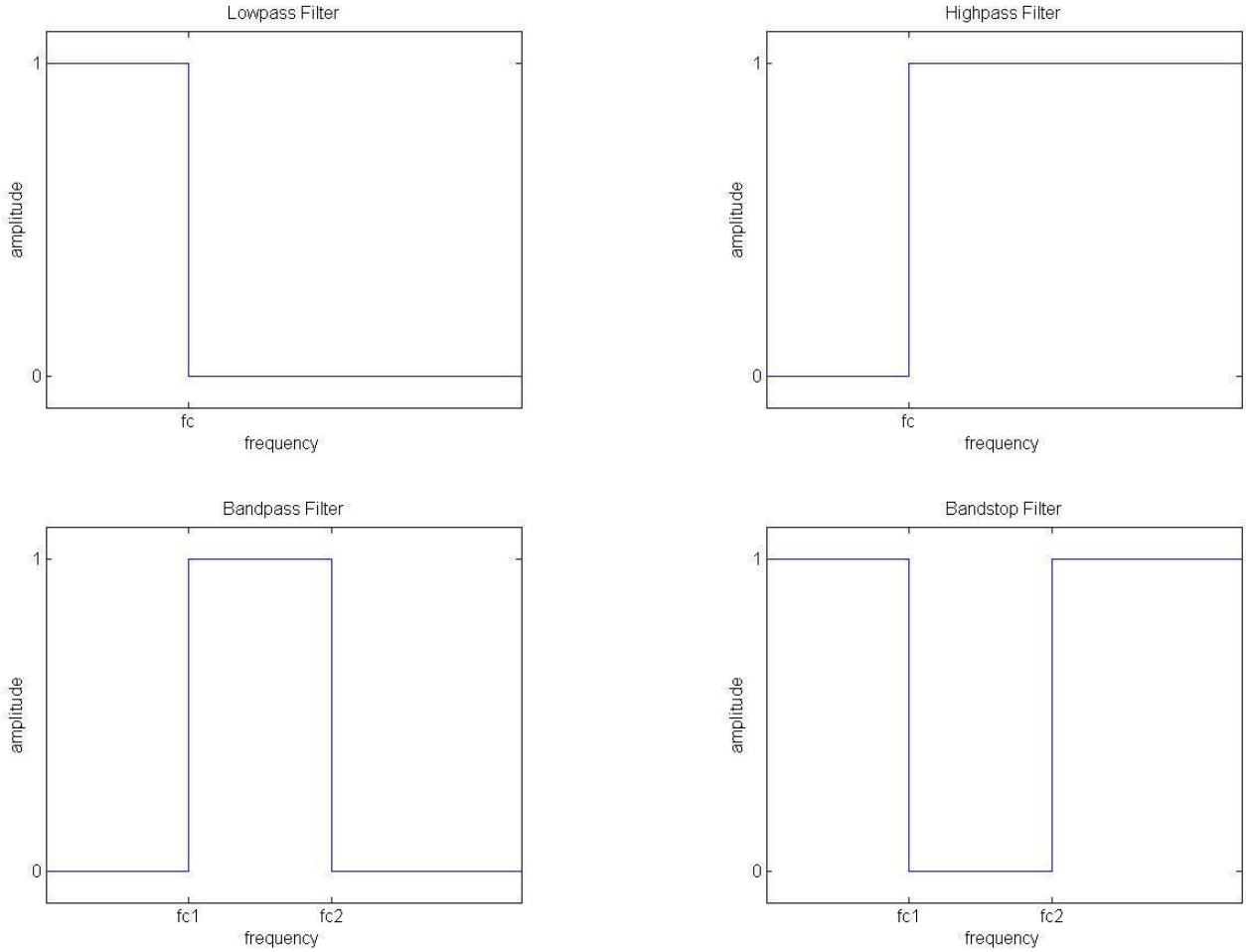

Figure 2.5: Different types of filters

The lowpass filter, shown in Figure 2.5, where the frequency response is unity over a certain range of frequencies and is zero at the remaining frequencies is a so-called boxcar filter or ideal frequency-selective filter designed in the spectral domain. Mathematically, this rectangular spectral window function is defined as:

$$\left|H[k]\right| = \begin{cases} 1 & \text{for} \quad \left|k\right| \le k_c \\ 0 & \text{for} \quad k_c < \left|k\right| \le K/2 \end{cases} \tag{2.19}$$

where k_c is the sample which corresponds to the cut-off frequency $f_c = k_c f_0$. Since the *k-th* sample of the filter spectrum directly corresponds to a specific frequency value via the linear relation $f = k f_0$, the definition of Eq. (2.19) can be adapted to the following frequency response:

$$\left|H(f)\right| = \begin{cases} 1 & \text{for} \quad \left|f\right| \le f_c \\ 0 & \text{for} \quad f_c < \left|f\right| \le f_{Ny} \end{cases} \tag{2.20}$$

with the amplitude of the filter $|H(f)|$ being dependent on frequencies instead of on samples. As this boxcar filter spectrum will be multiplied with the discrete Fourier transforms of the signal, this definition states that the signal spectrum for frequencies f smaller than or equal to the cut-off frequency f_c stays unmodified as it is multiplied by one. On the other hand, the signal spectrum for all the other frequencies up to the Nyquist frequency, i.e., higher than the cut-off frequency, is completely eliminated due to the multiplication with zero. If the inverse discrete Fourier transformation (IDFT) is applied to the samples *Y[f]* of the resulting spectrum, the filtered signal sequence *y* will only contain frequencies smaller than f_c. That means that within the GOCE signal processing just these lower frequency parts will be used for computing the SH coefficients. As there are no higher frequencies inherent in the filtered signal any more, it will look much smoother compared to the original signal. The smoothness obviously is dependent on the choice of the cut-off frequency: the lower the cut-off frequency, the more high frequencies are eliminated and consequently, the smoother the filtered signal will be.

The main problem of implementing this ideal boxcar lowpass filter in the spectral domain is the radical jump at the cut-off frequency from one to zero. This becomes obvious if the impulse response *h* of the filter is computed by inverse discrete Fourier transformation (IDFT). The resulting sequence in the time domain will be a sampled sinc-function with one main lobe and infinitely long side lobes. This function is truncated due to the limited number of samples at $n = \pm N/2$. With increasing cut-off frequency in the filter spectrum, the width of the main and each side lobes in the time domain is becoming smaller and the amplitudes of the side lobes are diminished. This inverse relation between filter width in the spectral domain and the width of the sinc-function lobes in the time domain is visualized in Figure 2.6. The side lobes as a consequence of the abrupt jump in the filter spectrum are rather unwanted. In the case of filtering the simulated GOCE data, a convolution of the original signal and the boxcar filter in the time domain (which is equivalent to a multiplication of their spectra in the spectral domain) will cause disturbing structures of ringing and ripples in the resulting filtered signal and in all derived quantities such as the gravitational potential and its derivatives. This effect is known as Gibbs' phenomenon. As a result, geoid heights of points in the direct neighbourhood are alternately weighted positive or negative by applying an along-track boxcar filter.

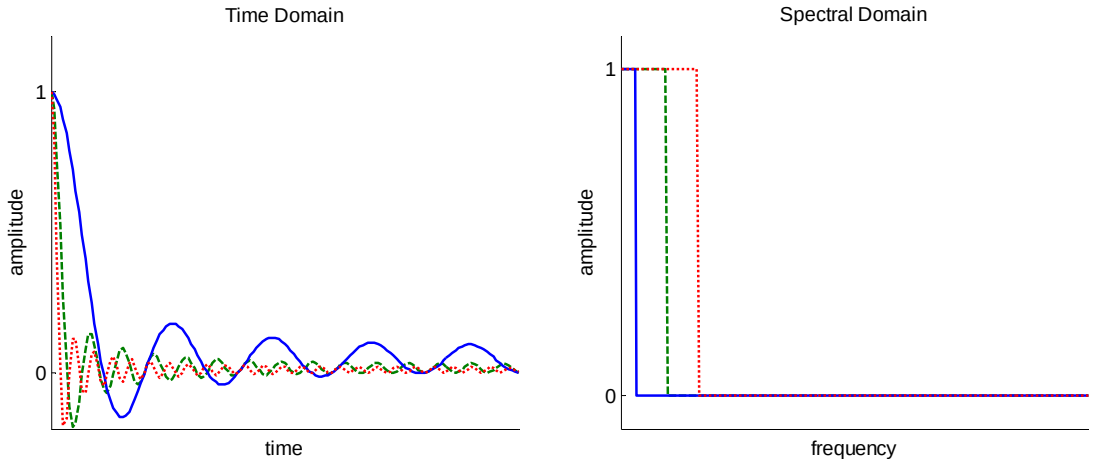

Figure 2.6: Boxcar lowpass filters with various cut-off frequencies in the time (left) and spectral domain (right)

This Gibbs' phenomenon can be moderated by using filters with a smoother transition between maximal and minimal amplitudes in the spectral filter design. Thus, the abrupt attenuation of frequencies larger than the cut-off frequency can be reduced.

One of these filters with a smoother transition is the Butterworth filter which is the second form of filter implemented in this study. The amplitude spectrum $|H(f)|$ of this filter is a monotonically decreasing function of the frequencies *f*, denoted by:

$$|H(f)| = \frac{1}{\sqrt{1+(f/f_c)^{2\cdot order}}} \tag{2.21}$$

where *f* is one of the entries in the frequency vector of the spectrum reaching from the fundamental frequency f_0 to the Nyquist frequency f_{Ny} and where f_c is the cut-off frequency. As opposed to the boxcar filter which is a fix rectangular function, the design of the Butterworth filter can be modified by varying the order of the filter. This further parameter determines the slope of the transition. If the order is increasing up to infinity, the transition between maximal and minimal amplitude becomes steeper and approaches the filter design of the boxcar filter (Figure 2.7).
Further, it is evident that $|H(f)|$, the amplitude of the filter in the spectral domain, is just converging to zero but is never actually reaching it. While the spectrum of the boxcar filter becomes zero at the cut-off frequency, it is always $1/\sqrt{2}$ at $f = f_c$ for a Butterworth filter regardless of the filter order. However, even if the Butterworth filter does not have the abrupt jump in its spectrum, it should be noted that it already modifies frequencies smaller than the cut-off frequency in contrast to the boxcar filter.

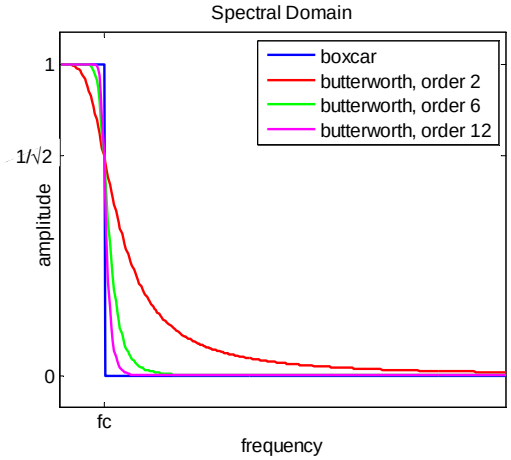

Figure 2.7: Comparison between boxcar and Butterworth lowpass filters with various orders in spectral domain

Just because of these different filter characteristics, it becomes evident that the application of both filters to the original signal will lead to varying filter results. However, by increasing the order of the Butterworth filter, the resulting filtered signal will approach the outcome of applying a boxcar filter to an original signal.

2.3.2 2D SPHERICAL MODEL FILTERING

While the previous section explained the along-track filtering of one-dimensional signals, this section will give a short overview of how two-dimensional models derived from the signal can be filtered. A second possibility of applying filters within the scope of processing simulated GOCE data, is filtering the models of the gravitational potential. As these two-dimensional models can be represented as spherical harmonic (SH) series (Eq. 2.2), spherical filtering suggests itself. In other words, filtering these models can be realized by multiplying the corresponding SH coefficients $\bar{C}_{\ell m}$ and $\bar{S}_{\ell m}$ by a certain weighting factor. This factor corresponds to the selected filter. As the SH coefficients are dependent on the degree ℓ and the order *m* of the SH series, they can be either filtered by an order or a degree filter. Since the spatial resolution of a model depends on the maximum resolvable degree $\ell = L_{max}$, using a degree filter was deemed to be the better alternative. That means that all coefficients with the same order *m* will be multiplied with the same filter factor while the factor varies with increasing degree ℓ.

In the same way as for the along-track filtering, a spherical boxcar as well as a Butterworth filter will be applied in the sequel. The corresponding factors of the two different spherical degree filters with a cut-off degree ℓ_c are computed for each degree reaching from zero to the maximum resolvable degree $\ell = L_{max}$ and are defined as follows:

- spherical boxcar filter factor:

$$b_\ell = \begin{cases} 1 & \text{for} \quad \ell \le \ell_c \\ 0 & \text{for} \quad \ell_c < \ell \le L_{\max} \end{cases} \tag{2.22}$$

- spherical Butterworth filter factor:

$$b_\ell = \frac{1}{\sqrt{1+(\ell/\ell_c)^{2\cdot order}}} \tag{2.23}$$

where *order* denotes the order of the filter and not the order of the SH series.

This becomes clearer if we take a look at the triangular representation of the degree factors for a spherical boxcar and a spherical Butterworth filter in Figure 2.8.

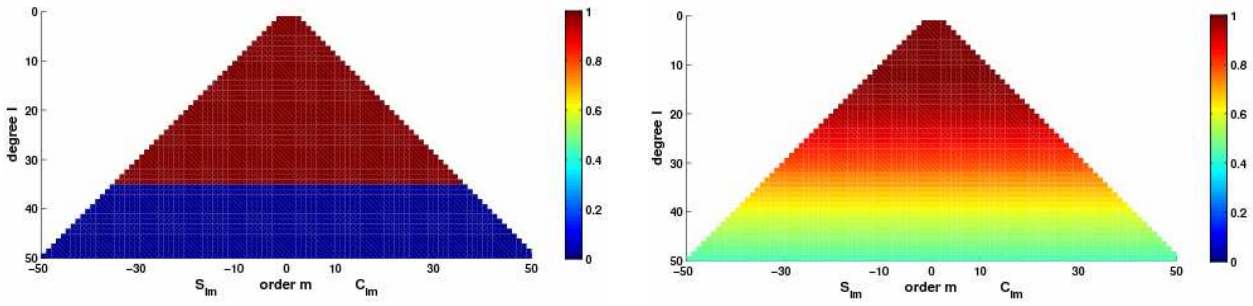

Figure 2.8: Triangular representation of a spherical boxcar and a spherical Butterworth filter

In order to apply a spherical filter to a global model and to obtain filtered SH coefficients $\overline{C}_{\ell m}^{filtered}$ and $\overline{S}_{\ell m}^{filtered}$, these filter factors b_ℓ have to be multiplied with the corresponding SH model coefficients $\overline{C}_{\ell m}$ and $\overline{S}_{\ell m}$:

$$\begin{aligned} \overline{C}_{\ell m}^{filtered} &= b_\ell \overline{C}_{\ell m} \\ \overline{S}_{\ell m}^{filtered} &= b_\ell \overline{S}_{\ell m} \end{aligned} \tag{2.24}$$

Thus, the implementation of along-track filters on the one hand and spherical filters on the other hand looks very similar on first sight. The main difference is that in the first case frequencies of a time series are filtered and that in the second case SH coefficients representing a geopotential model are filtered with respect to degrees. Both kinds of filters are applied by a multiplication of the filter weighting factors with the original data in the spectral domain.
Although there seem to be quite a few similarities in the implementations, a match between these along-track filters and the spherical ones is far from obvious as they are dealing with completely different datasets. They cannot be directly compared to each other. However, the different influences of these filters on the reference data will be examined and compared to each other in several testing procedures and their relation will be investigated empirically by the comparison of their transfer functions in the signal and model domain.

3 TESTING PROCEDURES

The main objective of this study is to compare empirically the influences of along-track and spherical filters. The along-track filters will be applied to simulated GOCE data on the one hand and the spherical filters to a global gravity field model on the other. The following sections will give an overview of the software used, the necessary input data and the various testing procedures in form of flowcharts.

3.1 Software packages

In order to generate synthetic data from a global model, known as synthesis step, as well as to estimate a new model from these simulated data which is referred to as analysis step, a FORTRAN software package created by Gernot Plank has been used. This program consists of two main but completely independent parts:

- 'create' (`create_new_obs_file.exe`): synthesis for signal generation
- 'adjust' (`adjust.exe`): analysis based on least squares adjustment (time-wise approach) for model estimation

All further computations were implemented in MATLAB R2007a augmented by the additional Signal Processing Toolbox. Based on global geopotential models, there are mainly four quantities which will be taken into account for the testing procedures of this work (Figure 3.1).

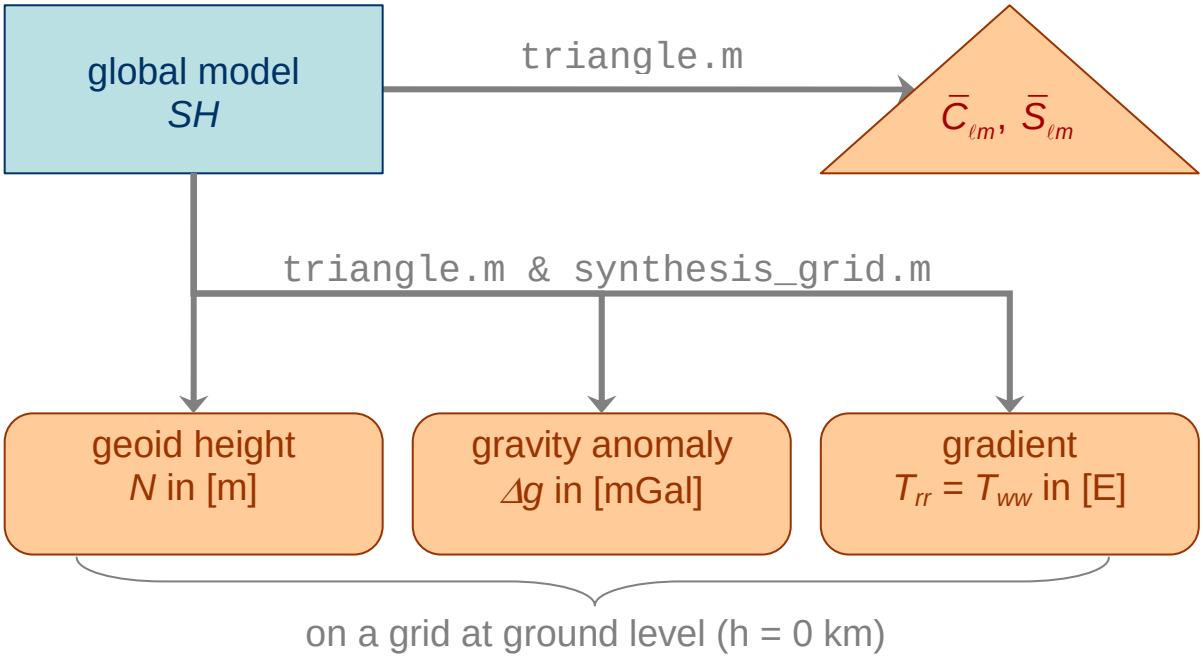

Figure 3.1: Different representations of a global model

For the sake of better visualization of the global models, it is common to represent the spherical harmonic coefficients in the form of a triangle which has been already explained in the background section 2.1. This specific triangular representation of SH coefficients is implemented in the MATLAB code `triangle.m`.

Another MATLAB code called `synthesis_grid.m` plots the gravitational potential and its derivatives on a grid on the surface of the Earth with *h = 0km*. This time, a discrete global spherical harmonic synthesis is realized by the implementation of the MATLAB function `gshsag.m` which was created by Matthias Weigelt. It is an adaption of the original function `gshs.m` which belongs to the spherical harmonic MATLAB toolbox (SHBUNDLE) from Nico Sneeuw. The MATLAB toolbox can compute all relevant quantities from a spherical harmonic model such as geoid heights *N* in meters *[m]*, gravity anomalies Δg in milligal *[mGal]* and the second order radial derivatives, the so-called radial gravity gradients, in Eötvös *[E]*.

On the other hand, the output from these tests will not only be the SH coefficients of global geopotential models but also time series of the simulated signal, either in the original or filtered form. Thus, the interpretation of the results also takes the square root of their power spectral densities (PSD) into account. This square root of the PSD given in $E/\sqrt{Hz}$ is derived from a signal measured along the orbit at satellite height (Figure 3.2). The PSD of a signal can be computed with the MATLAB function `periodogram.m` which belongs to the signal processing toolbox.

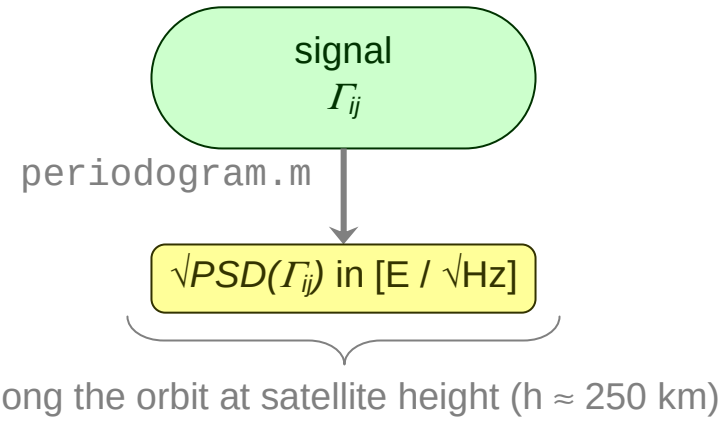

Figure 3.2: Square root of the PSD computed from satellite signal

With respect to the implementation of filters, following MATLAB programs were used:

- `boxfilter.m`: boxcar filtering of simulated signal (along-track filtering)
- `Butterworth.m`: Butterworth filtering of simulated signal (along-track filtering)
- `SH_boxfilter.m`: boxcar filtering of global model (spherical harmonic filtering)
- `SH_Butterworth.m`: Butterworth filtering of global model (spherical harmonic filtering)

3.2 Input data

For these tests, the EGM96 (Earth Gravity Model 1996) was chosen as full global model. The major reference for this model is NASA/TP-1998-206861. EGM96 is a spherical harmonic model of the Earth's gravitational potential truncated at a maximum degree and order of $L_{\max} = 360$. It is provided in the form of spherical harmonic coefficients in the file `egm96_to360.ascii`. Due to the high computational effort with a full global model, not all coefficients were used for the computations in this study. Instead, one set with maximal degree and order 50 was chosen. However, it should be kept in mind that the spatial resolution of a global model gets worse with decreasing truncation order and degree.
In order to enable investigations prior to the launch, simulated datasets are provided. The signal on which this study is based on, was generated along a simulated *29-days* repeat orbit of GOCE with a sampling rate of *5 seconds* or *0.2 Hz*. The simulation is based on a noise-free scenario which means that there is no noise inherent in the dataset. The orbit information is given in `pos_29d_5s_sst80.estec` The characteristics of the orbit are summarized in the following Table 3.1. The corresponding zoomed in ground-track is plotted in Figure 3.3.

Table 3.1: Orbit characteristics

orbit characteristics	
orbit length	29 days
number of data samples	501148
sampling rate	5 seconds
number of revolutions	467
inclination	96.6°
nominal altitude	ca. 250 km

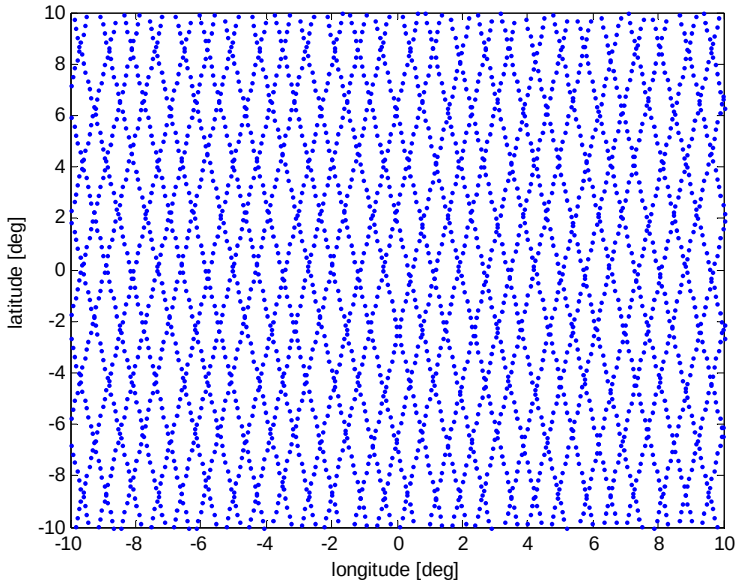

Figure 3.3: Ground track of orbit, zoomed in

3.3 Testing procedures

3.3.1 CLOSED-LOOP TESTS

The first step before applying any filters to the data is to validate the implemented software package by so-called closed-loop tests. In our case, the simulated signal is generated by using the EGM96 model, i.e., the corresponding spherical harmonic (SH) coefficients, as an input for the synthesis program '*create*'. The output of the signal is given as a tensor of nine gravitational gradients defined in Eq. (2.4). Within this study, only the diagonal elements of the tensor will be used which are the components in along-track direction V_{xx}, in cross-track direction V_{yy} and in radial direction V_{zz}.

The back-computation of an estimated model from the generated signal can be realized by using the analysis program '*adjust*'. It gives the possibility to use either all three diagonal tensor elements (V_{all} which is V_{xx}, V_{yy} and V_{zz}) or only one of them (V_{xx}, V_{yy} or V_{zz}). This leads to four estimated models with different spherical harmonic coefficients (SH_{all}, SH_{xx}, SH_{yy} and SH_{zz}).

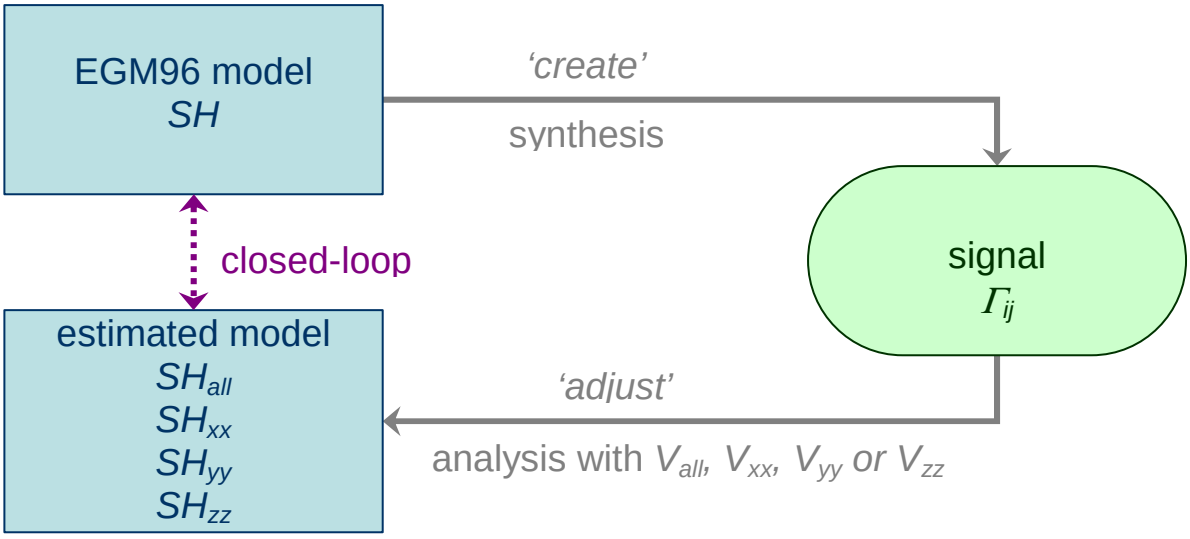

Figure 3.4: Flowchart for closed-loop tests

The synthesis together with the analysis forms a closed-loop which simulates a signal out of an original model and estimates the model back from this signal. If the two completely independent programs '*create*' and '*adjust*' work perfectly fine and if the dataset is not manipulated within this closed loop, the original and the estimated model, should be theoretically the same with small differences lying within the level of the numerical accuracy of the computer. Figure 3.4 shows the closed-loop test in the form of a flowchart. These kinds of flowcharts will be used in all of the following test scenarios. Therefore, the flowchart in this section will be explained in detail only once and should serve as an example for all the following sections.
Blue rectangles represent global models, either the original EGM96 model or the estimated model. The green ellipse stands for any type of generated signal. Gray arrows describe the procedure

which is applied to the data in rectangles or ellipses. This can be a synthesis, an analysis, filtering or shortening of the signal. Double arrows in purple indicate which data will be compared to each other.
This particular closed-loop test in Figure 3.4compares the spherical harmonic coefficients of the original EGM96 model with those of the estimated model. The comparison is either based on the triangles of the spherical harmonic coefficients or by means of the geoid heights, gravity anomalies and the second order radial derivatives which can be determined by applying the SHBUNDLE software to the models. The results will be discussed in section 4.2.

3.3.2 ALONG-TRACK FILTERING

If the closed-loop tests prove that the software provides reliable results, the next step is to test the influences of different kinds of filters. This section deals with the explanation of the procedure to test along-track filters applied to the one-dimensional simulated signal. The corresponding flowchart is shown in Figure 3.5.

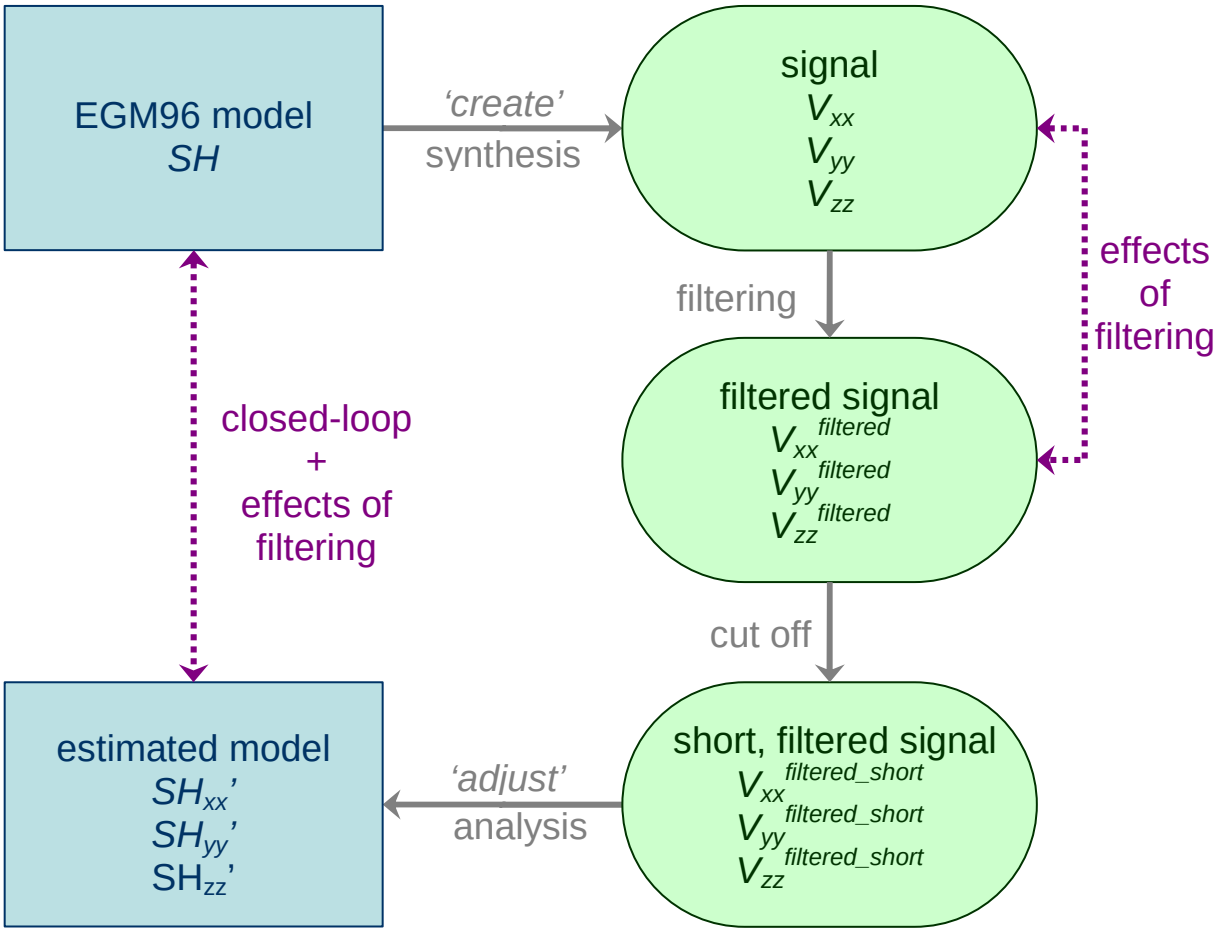

Figure 3.5: Flowchart for along-track filtering

At first, the signal components V_{xx}, V_{yy} or V_{zz} can be determined by a synthesis step. Each of these three data series is filtered with a boxcar or a Butterworth filter with various cut-off frequencies and various orders in the case of the Butterworth filter. In order to compensate for the transient oscillation and warm-up effects which can be seen in the of the filtered signal components $V_{xx}^{filtered}$, $V_{yy}^{filtered}$ or $V_{zz}^{filtered}$, 10,000 samples are cut off in the beginning and in the end of the filtered signal. The subsequent analysis estimates a new model from the shortened and filtered signal $V_{xx}^{filtered\_short}$, $V_{yy}^{filtered\_short}$ and $V_{zz}^{filtered\_short}$. The output are three different sets of spherical harmonic coefficients SH_{xx}', SH_{yy}' and SH_{zz}'. These coefficients are compared to the corresponding coefficients of the original EGM96 model in the form of SH triangles as well as on a grid for geoid heights, gravity anomalies and the radial gravity gradients. Since the data sets have been manipulated by a filter this time, the comparison between original and estimated model will not only include the closed-loop differences but also the filter effects. The influences of filtering signals along-track are shown in section 4.3.

3.3.3 FILTERING SPHERICAL HARMONIC COEFFICIENTS

Another testing approach deals with the filtering of spherical harmonic (SH) coefficients (Figure 3.6).

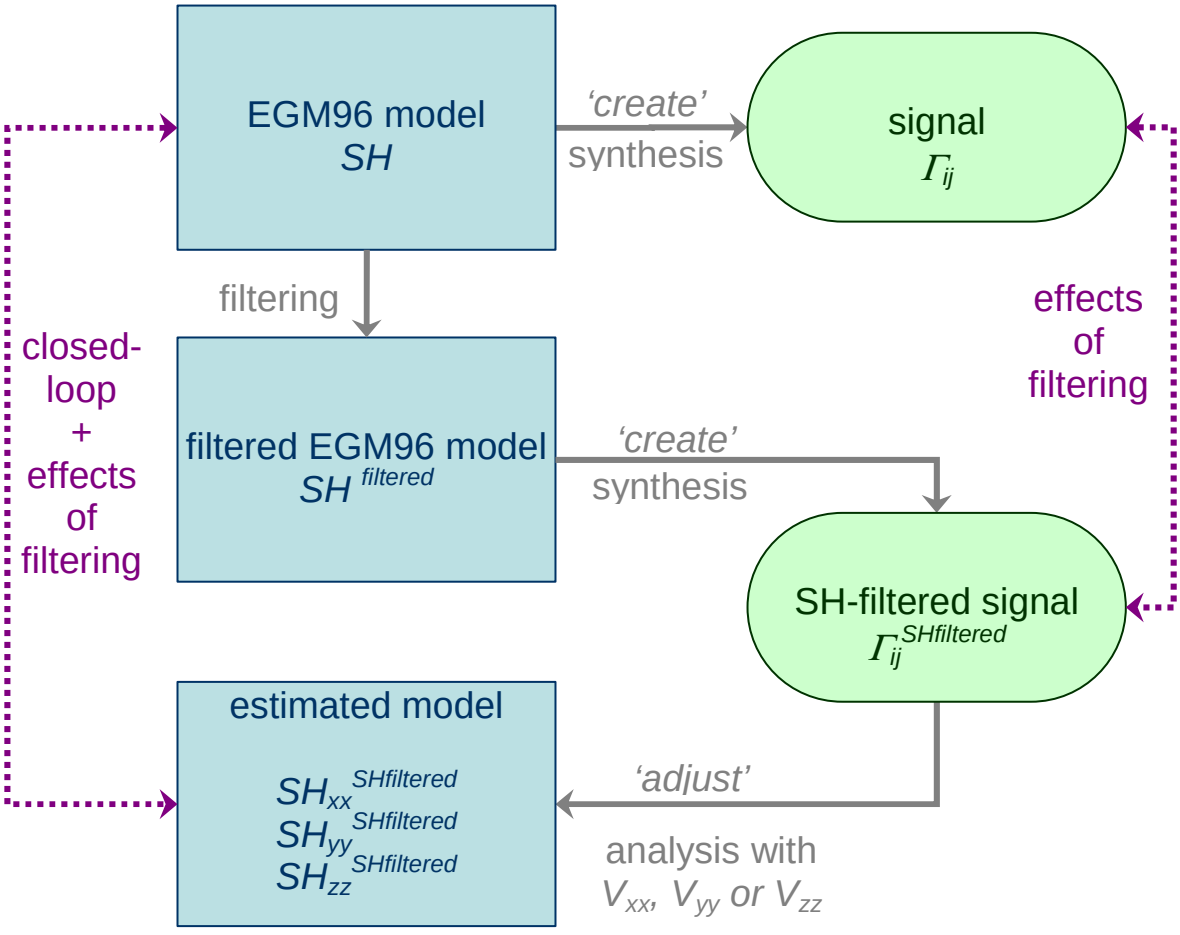

Figure 3.6: Flowchart for SH filtering

In this case, all SH coefficients of the global EGM96 model are filtered two-dimensional with a boxcar as well as a Butterworth filter. Based on this filtered EGM96 model ($SH^{filtered}$), one can generate the corresponding signal tensor $\Gamma_{ij}^{SHfiltered}$ by a synthesis step. Analogously, a reference signal Γ_{ij} can be determined based on the original global EGM96 model. By comparing this original with the SH-filtered signal, the effects of SH filters on the one-dimensional signal can be investigated. In order to determine the filter effects on the SH coefficients, an analysis of the SH-filtered signal components makes it possible to put the original model side by side to the estimated model ($SH_{xx}^{SHfiltered}$, $SH_{yy}^{SHfiltered}$, $SH_{zz}^{SHfiltered}$). The outcome will be shown in section 4.4.

3.3.4 EMPIRICAL DERIVATION OF TRANSFER FUNCTIONS

The previous two sections explained the implementation of applying along-track filters to the simulated signals as well as the test procedure of applying spherical filters to the models. It is, however, also interesting to see how a spherical filter need to be designed in the model domain in order to achieve the same results as an along-track filter applied in the signal domain. Accordingly it will be investigated how an along-track filter should look like in the signal domain if it should have the same influences as a spherical filter in the model domain. This is analogue to converting an along-track filter into a spherical filter and vice versa. Therefore, transfer functions will be derived empirically. A transfer function basically transfers the reference input data into filtered output data.

For the along-track filter in the signal domain, the corresponding transfer function in the model domain can be empirically derived as follows (see also Figure 3.7):

1. Use of a global model estimated from closed-loop yielding reference models SH_{xx}, SH_{yy} and SH_{zz}, where each model consists of the SH coefficients $\bar{C}_{\ell m}$ and $\bar{S}_{\ell m}$ (including closed-loop errors which are negligibly small)
2. Application of 1D along-track filter to synthetic satellite data Γ_{ij} and retrieval of filtered global models SH_{xx}', SH_{yy}' and SH_{zz}' (SH coefficients $\bar{C}_{\ell m}^{filtered}$ and $\bar{S}_{\ell m}^{filtered}$)
3. Empirical derivation of transfer function in model domain (which corresponds to along-track filter in signal domain) by computing the proportion between filtered and reference global models:

$$b_{\ell m} = \frac{\bar{C}_{\ell m}^{filtered}}{\bar{C}_{\ell m}}$$
$$b_{\ell m} = \frac{\bar{S}_{\ell m}^{filtered}}{\bar{S}_{\ell m}} \qquad (3.1)$$

In other words, a new filter triangle with SH coefficients $b_{\ell m}$ will be derived by calculating the ratio between filtered SH coefficients ($\bar{C}_{\ell m}^{filtered}$ and $\bar{S}_{\ell m}^{filtered}$) and reference SH coefficients ($\bar{C}_{\ell m}$ and $\bar{S}_{\ell m}$). The ratio comes from modifying the spherical filter equation (Eq. 2.24). This transfer function in the form of a new filter triangle symbolizes the spherical filter which would have to be applied to the reference model in order to achieve the same effects as the corresponding along-

track filter applied to the reference signal. It should be also noted that the closed-loop errors are inherent in the reference model as well as in the estimated filtered model.

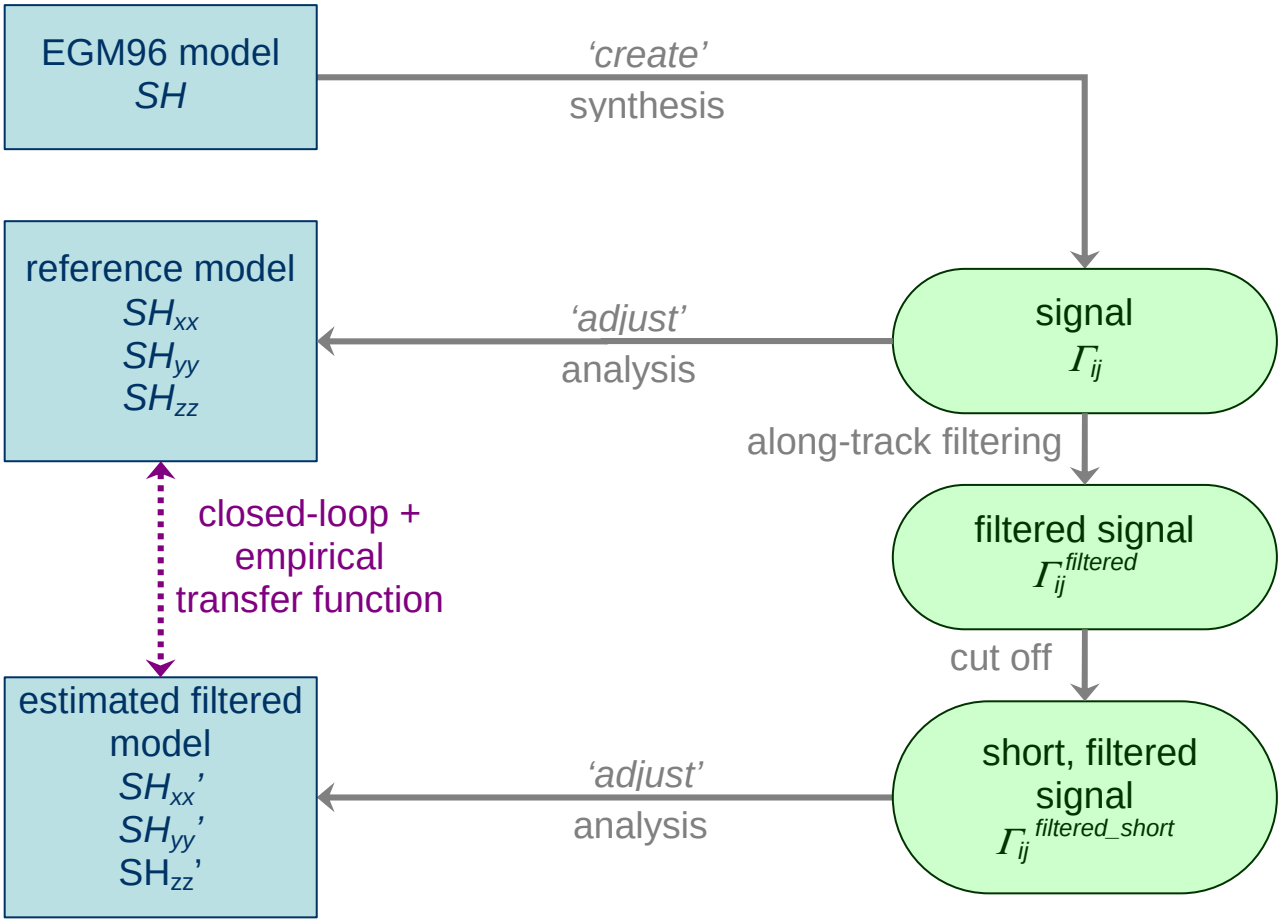

Figure 3.7: Flowchart for empirical derivation of transfer function in model domain in the case of along-track filtering

This procedure can be repeated analogously for spherical filtering in the model domain. The following steps explain the empirical derivation of a corresponding transfer function in the signal domain (see also Figure 3.8):

1. Use of synthetic data generated from global model yielding reference signal Γ_{ij} (represented by its Discrete Fourier Transform samples $X[k]$)
2. Application of 2D spherical filter to same model and generation of filtered synthetic satellite signal $\Gamma_{ij}^{SHfiltered}$ (represented by its Discrete Fourier Transform samples $Y[k]$)
3. Empirical derivation of transfer function in signal domain along the orbit (which corresponds to spherical filter in model domain) by computing the quotient of the DFTs of filtered and reference signals:

$$H[k] = \frac{Y[k]}{X[k]} \tag{3.2}$$

That means that modifying the along-track filter equation (Eq. 2.18) yields samples *H[k]* of a filter sequence in the signal domain which will have the same influence on the reference data as its corresponding spherical filter in the model domain.

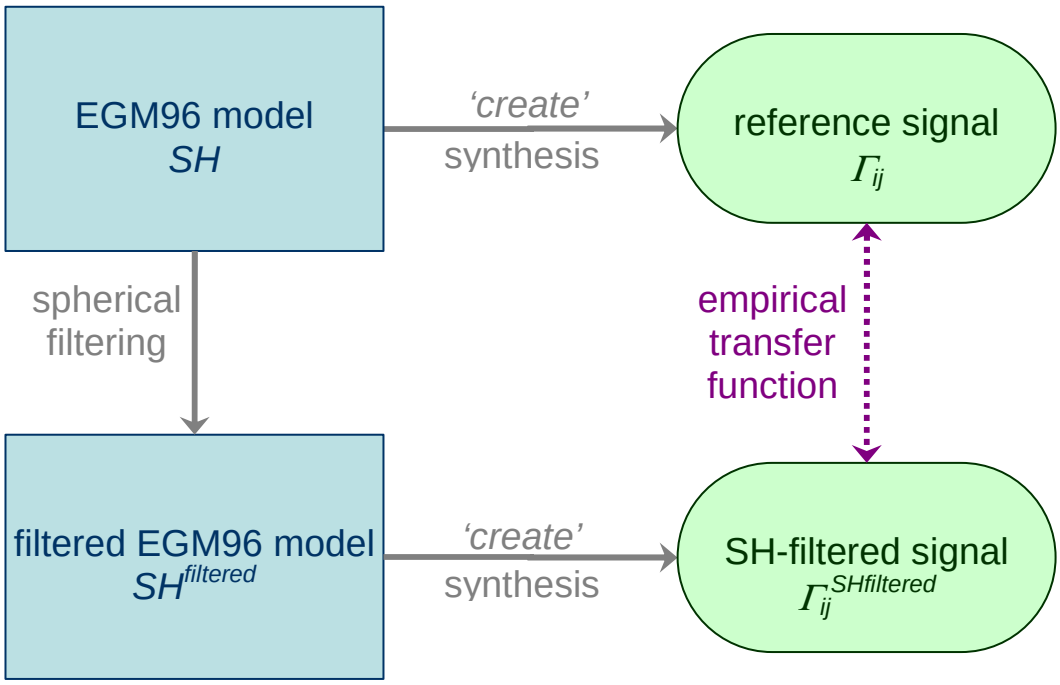

Figure 3.8: Flowchart for empirical derivation of transfer function in signal domain in the case of spherical filtering

It should be noted that this section actually describes the counterpart of the two previous sections. Instead of designing filters and then looking at the outputs, the transfer functions of filters in signal or model domain are computed based on the output from the corresponding filters in the other domain, respectively. This makes it possible to draw an empirical comparison between along-track and spherical filters. Thus, along-track filters can be converted into spherical filters depending on their outputs and vice versa.

In real case scenarios, the exact reference model is not available. Therefore, a priori information has to be used in order to compare filtered and reference signals and models. Consequently, the outcome could be biased towards this a priori information. This needs further investigation in the future.

4 DISCUSSION OF RESULTS

The outcome of the testing procedures described in the previous section 3.3 is interpreted in various ways.
Section 4.1 will introduce the reference dataset. This is on the one hand the reference model EGM96 which can be represented in different ways. It should be kept in mind that all the following results in the model domain will not be shown as absolute but rather as relative results in the form of differences to the reference model. The second kind of reference data is the simulated reference signal in the form of a square rooted PSD spectrum which will be directly compared to the spectrum of the filtered signal.
Sections 4.2 - 4.4 mainly investigate the differences between original and estimated, possibly even filtered datasets, with respect to variations of the along-track, cross-track and radial component in the signal. Another interesting point in this context is the change between geoid heights, gravity anomalies and the radial gravity gradients.
An overview of the results using different filter properties will be given in section 4.5. This can be either one-dimensional along-track boxcar or Butterworth filters of different orders with varying cut-off frequencies or it can be two-dimensional spherical boxcar or Butterworth filters of different orders with varying cut-off degrees.
Finally, section 4.6 will present the results of the empirical investigation of the filter transfer functions in order to examine the relation between along-track and spherical filters.

4.1 Reference data

4.1.1 REFERENCE MODEL

As already mentioned in section 3.2, the EGM96 was chosen as reference global model of the Earth's gravitational potential. For the interpretation of the test cases, it was considered as suitable to only use spherical harmonic (SH) coefficients up to a maximum order and degree of 50 in order to keep the computational effort low. Using references with higher or lower maximal degrees does not change the final results significantly but has a considerable influence on the resolution and the speed of the computations. The following arrangement of plots in Figure 4.1 shows four different quantities based on the EGM96 with $L_{\max} = 50$. An overview in form of a flowchart has already been shown in section 3.1.

a) **Spherical harmonic (SH) coefficients arranged in a triangle**.
The vertical axis of the triangle represents the degrees ℓ of the SH coefficients. The horizontal axis refers to the order $m \le \ell$ with the cosine $\overline{C}_{\ell m}$ coefficients on the right and the sine $\overline{S}_{\ell m}$ coefficients on the left side. The coefficients with increasing degree ℓ refer to decreasing scales of the gravity field. The colour code of the triangles represents the logarithm of the absolute values of the coefficients.
For the EGM96, the absolute and logarithmic values of the SH coefficients reach from -11 to -4. The higher the degree, the more coefficients have smaller values up to -11.

b) **Geoid heights, *N*,** in meters *[m]* measured from the mean Earth ellipsoid.
Due to the fact that geoid heights are primarily long-wavelength features, the plot looks very smooth. The values lie in an interval of around - 105 to + 79 meters. Areas coloured in red as for example in the Andes of Peru have a higher altitude and are indicating a stronger signal than blue areas as e.g. in the Indian ocean. Positive heights are situated above the reference ellipsoid, negative heights below.

c) **Gravity anomalies, Δg,** in milligal ($1mGal = 10^{-5} m/s^2$) representing the differences between measured and normal gravity at any point ($\Delta g = g - \gamma$).
As the gravity g is the magnitude of the gradient of the potential and thus proportional to the first derivative of the geoid heights, it can be recognized that the structures of the gravity anomaly plot are stressing these areas with higher changes, edges respectively, (density inhomogeneities, mountain ridges, etc.) in the geoid heights. The features are becoming sharper which can be clearly seen in the Andes, for example. Thus, differentiating the potential is analogous to applying a high-pass filter to the original dataset. The values of the gravity anomalies range from - 82 to + 103 mGal.

d) **Gravity gradients, T_{rr},** in Eötvös ($1E = 10^{-9} s^{-2}$) which are the second-order radial derivatives of the potential and the first-order radial derivatives of the gravity vector.
The vertical gravity gradient is usually the largest component with values up to 3000 E on Earth. For better visualization, however, the Earth ellipsoidal effect has been subtracted. That is why the gravity gradient values are only ranging from – 5 to + 6 E. Due to the characteristics of differentiation, the corresponding plot evinces even smaller features than the plots for the geoid heights and for the gravity anomalies.

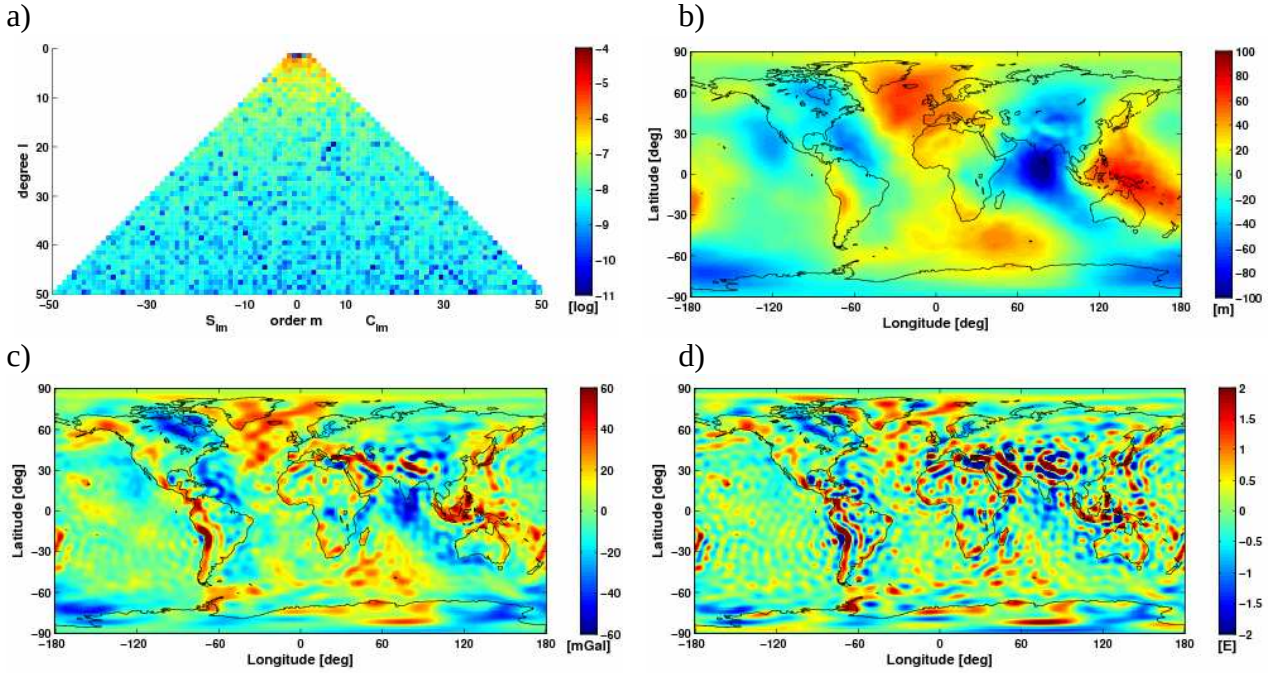

Figure 4.1: Four different representations based on the global model EGM96
a) spherical harmonic coefficients within a triangle, b) geoid heights in [m], c) gravity anomalies in [mGal] and d) radial gravity gradients in [E] with b)-d) plotted on a ground level grid.

The geoid heights, gravity anomalies and radial gravity gradients are plotted on a grid of points at the Earth's surface. These points are equi-angularly spaced with a resolution of one degree.

It should be noted that if the last four plots, let it be the spherical harmonic triangle, geoid heights, gravity anomalies or gravity gradients, are based on any estimated model, they look very similar to the original plots of the complete EGM96 model. Thus, the following sections will only discuss the plots of the differences between these original and estimated models but will not show the full model results.

4.1.2 REFERENCE SIGNAL

The synthetic reference signal was generated from the reference EGM96 global model with maximum degree and order 50. It is a time series of noise-free observations along a simulated *29-days* repeat orbit of GOCE with a sampling rate of *5 seconds* or *0.2Hz* (see section 3.2) at satellite height.

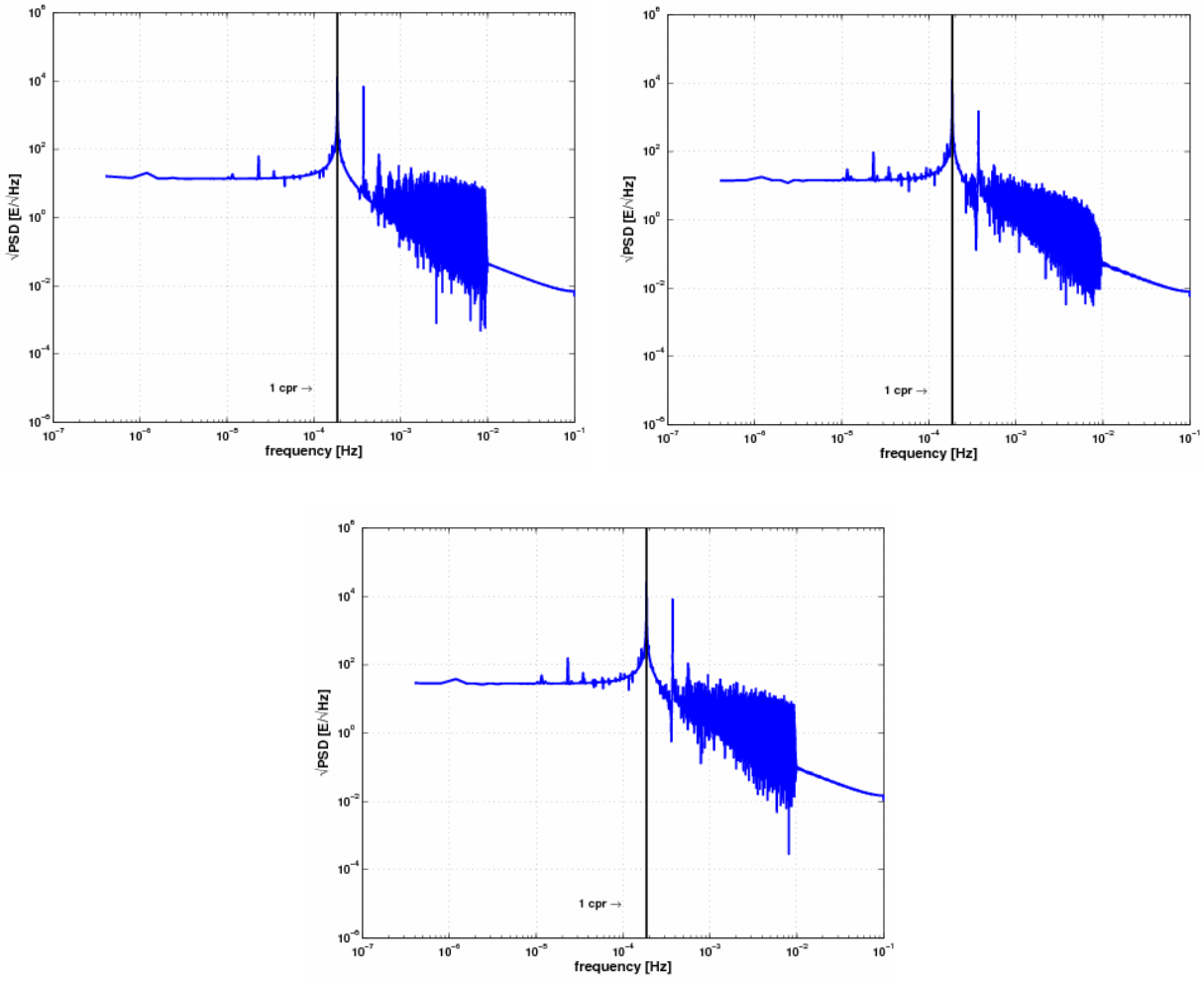

Figure 4.2: √PSD of reference signal for along-track component V_{xx} (top left), cross-track component V_{yy} (top right) and radial component V_{zz} (bottom)

All three components (V_{xx}, V_{yy} and V_{zz}) of the reference signal can be represented as square rooted power spectral density (PSD) estimates in [*E/√Hz*] versus frequencies ranging from the fundamental to the Nyquist frequency (Figure 4.2). The *√PSD* spectrum describes how the square root of the power, i.e., the amplitude, of each signal component is distributed over frequency. Due to better visualization, it will be presented on a logarithmic scale. The revolution frequency of the satellite will be additionally shown as a black line at *0.186mHz* or one cycle per revolution (*1cpr*) in every square rooted PSD plot. The highest amplitudes are concentrated on a frequency band between approximately *0.2mHz* and *0.4mHz* containing two major peaks. The first peak at around *0.2mHz* falls together with the revolution frequency and the second peak at approximately *0.4mHz* is identical to twice the revolution frequency. These peaks have magnitudes of about *12.5ME/√Hz* and *6.8ME/√Hz* for the along-track component V_{xx}, about *12.5ME/√Hz* and *4.8ME/√Hz* for the cross-track component V_{yy} and the highest magnitudes for the radial component V_{zz} with about *25.0ME/√Hz* and *9.6ME/√Hz*. For higher frequencies up to *10mHz*, the spectrum starts to oscillate with a generally decreasing trend. In a frequency band from about *10mHz* up to the Nyquist frequency of *100mHz*, the square rooted PSD of the reference signal is strictly monotonic decreasing without any oscillations. This means that the signal contains only little information in this band since the input model was limited to degree and order 50.
Apart from some smaller differences, the graphs of all three components look very similar. It is, however, evident that the square rooted PSD of the radial component V_{zz} is slightly higher than those of the other components. This was expected as the signal is strongest in the radial direction.
In the following sections, these reference spectra will be directly compared to the spectra of the simulated filtered signals.

4.2 Closed-loop tests

The purpose of implementing closed-loop tests is mainly to check the reliability and consistency of the software and the dataset used. If everything works fine, the differences between original and estimated model are expected to lie within the numerical accuracy of the computer. The implementation of this closed-loop test is explained in detail in chapter 3.3.1.
As it can be seen in Figure 4.3, this section is not interested in the absolute model outcomes but in the differences between the original EGM96 and the estimated model which was computed by applying the two independent software programs *'create'* and *'adjust'*. These differences will be presented in form of triangle plots ($\Delta\overline{C}_{\ell m}, \Delta\overline{S}_{\ell m}$) as well as in the form of three different quantities on a grid at ground level which are geoid heights (*ΔN)*, gravity anomalies (*Δ(Δg))* and gravity gradients (ΔT_{rr}). The difference plots will be arranged in the same way as it was already done for the reference EGM96 model in Figure 4.1. Since the estimated models within the closed-loop tests can be computed by either using all diagonal components of the signal tensor for the analysis step or only one of them (along-track V_{xx}, cross-track V_{yy} or radial V_{zz}), there will be shown four of these difference plot arrangements in the sequel of this section (Figure 4.4-Figure 4.7).
Taking a first quick glance at these figures and the corresponding statistics in Table 4.1, it is evident that the differences within all of these plots lie in fact within the computational accuracy. The triangle plots in the figure parts a) provide difference values from 10^{-15} to 10^{-22}. The application of the cross-track component V_{yy} (Figure 4.6) leads to the maximal RMS values for the differences in the geoid height with *0.13μm,* for the gravity anomalies with *0.13nGal* and for the radial gravity gradients with *3.30nE.*

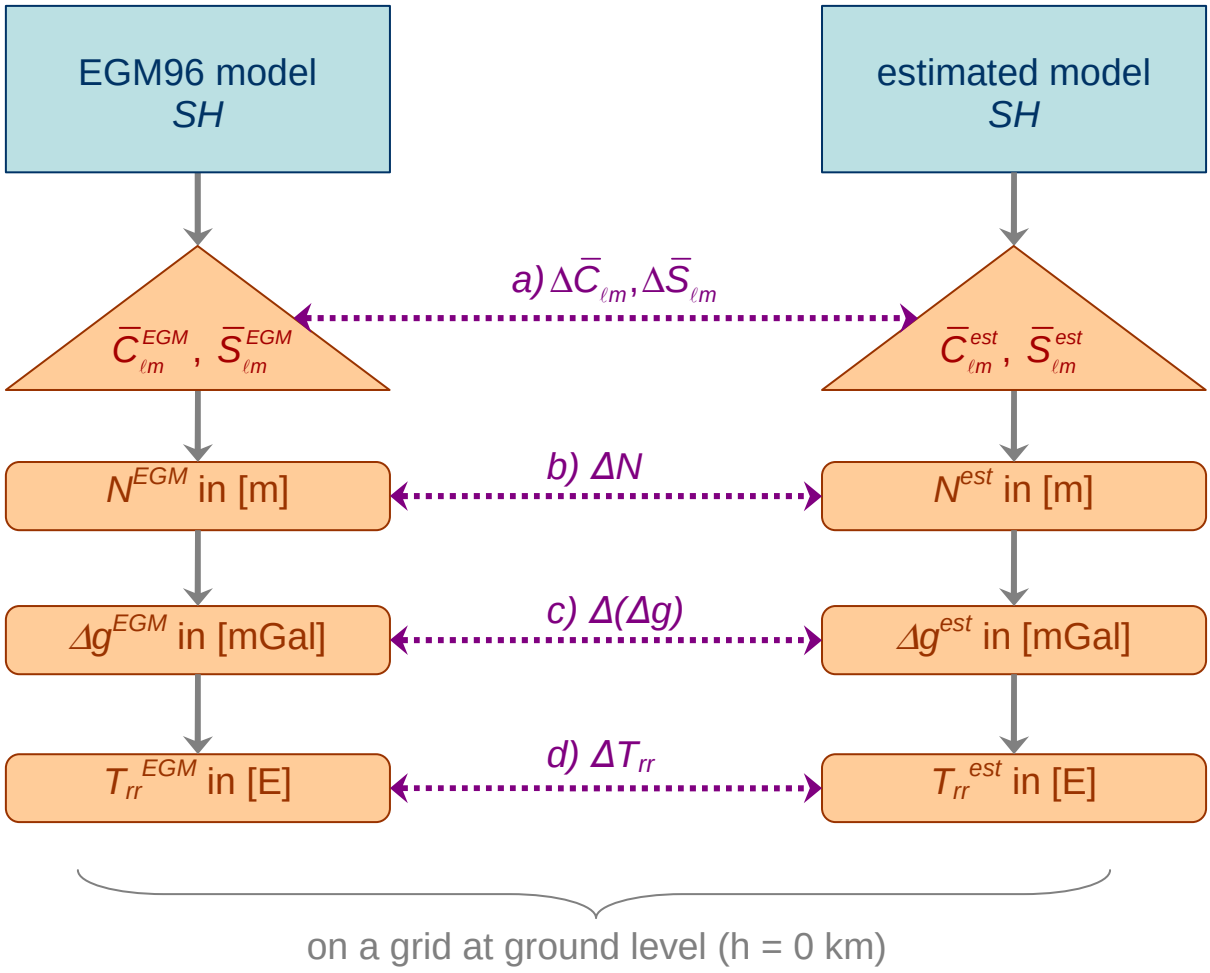

Figure 4.3: Flowchart for comparison of closed-loop test results

Table 4.1: RMS values for closed-loop test

signal components	RMS of ΔN [nm]	RMS of $\Delta(\Delta g)$ [pGal]	RMS of ΔT_{rr} [nE]
all V_{all}	2.237	0.158	0.011
along-track V_{xx}	1.403	0.330	0.011
cross-track V_{yy}	134.899	132.828	3.303
radial V_{zz}	83.087	80.444	2.920

The first case, revealed in Figure 4.4, demonstrates the differences between original and computed model if all signal components are taken into account. In the relatively symmetric triangle plot in a), there is a trend of an increasing number of SH coefficients with smaller differences up to values

of 10^{-22} if the degree is increasing. That trend is similar to the absolute global EGM96 model whereas the relative values are much smaller. Another clearly visible structure is the vertical line along the zonal SH coefficients of zero order with slightly higher differences of up to 10^{-15} compared to the relative values of the surrounding coefficients. As the orbit of GOCE is not polar but has an inclination of 96.6 degrees, there are no measurements above the North and South Pole. These so-called polar gaps have a direct influence on the zonal SH coefficients. Other similar but less distinct features can be seen along the vertical axes of the orders $m = \pm 16, 32, 48$. The reason for these bands of slightly higher values is mainly due to the orbit resonance. In the case of a noise-free scenario, the fundamental rotational frequency which is 16 revolutions per day for GOCE, affects the SH coefficients in the triangle with orders which are a multiple of this revolution number 16.

The plots b)-d) of Figure 4.4 show that the quantities on a grid reveal clear features in west-east direction, i.e., almost perpendicular to the flight (along-track) direction of the satellite. This means that the error in $\overline{C}_{20}$ is dominant. The similarity between the three subplots and the plots in Figure 4.7 when applying the radial component only, is remarkable and is due to the fact that the radial signal component is dominant. Furthermore, the absolute geoid height differences between original and estimated models b) are smaller in regions of latitudes from about ±20 to ±35 degrees and a small zone on the South Pole if compared to other regions, as e.g. the North Pole and the Equator. These features are again ascribed to the polar gaps. The smooth long wavelength structures of the geoid heights get lost in the first and second derivation of the potential. As a consequence, the features in the plots for the gravity anomalies c) and especially for the gravity gradients d) become more detailed.

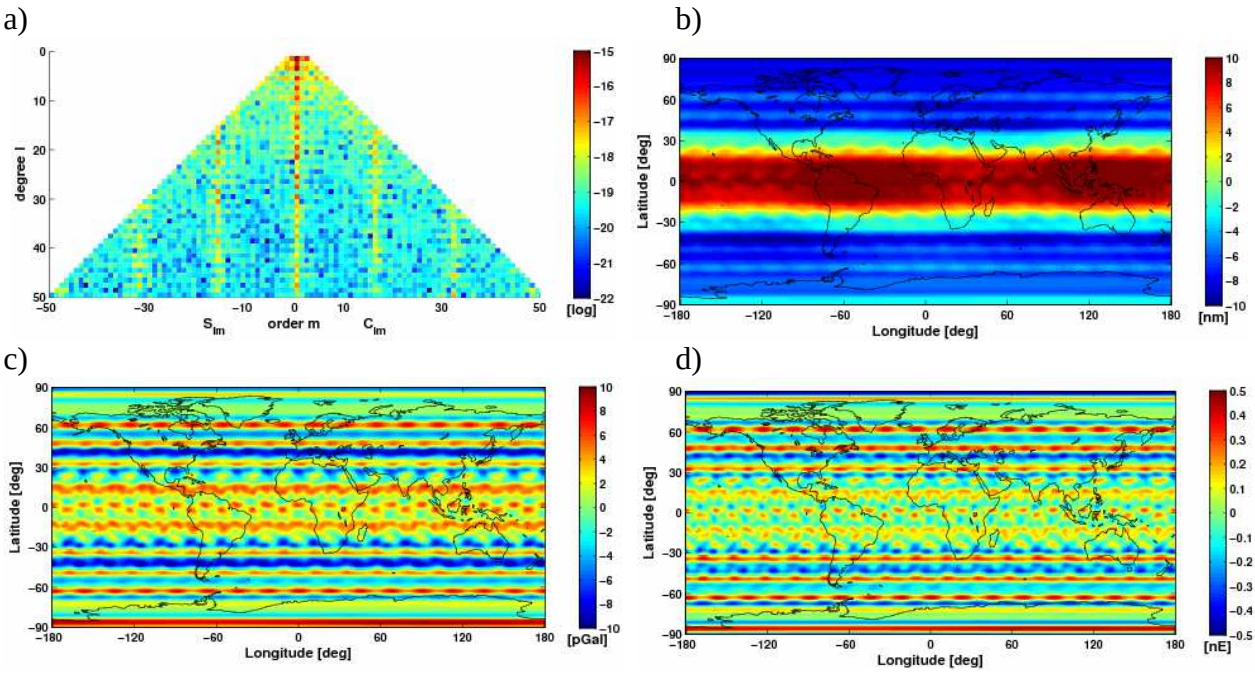

Figure 4.4: Differences between original EGM96 and estimated model (analysis with all signal components) in closed-loop test for a) SH triangle, b) geoid heights, c) gravity anomalies and d) radial gravity gradients.

If only the along-track component V_{xx} is used for the analysis, then the features in the plots in Figure 4.5 look very different although the statistics do not differ significantly from each other (Table 4.1). While the RMS of the geoid height differences for the application of the along-track component is a little bit better with *1.4nm* compared to *2.2nm* for all components, it is vice versa for the gravity anomalies with *0.33pGal* compared to *0.16pGal.* The relative RMS values for the gravity gradients are the same for both cases with ca. *0.01nE.* The corresponding plots b) – d), however, stress features in along-track direction which is almost a north-south feature on the Earth surface. The little offset between north-south and flight direction is due to the inclination of the satellite orbit. Analogue to the case with all components and to the reference field, the features of the geoid gradients are sharper than for the geoid heights and for the gravity anomalies. The relatively high geoid height differences on the Poles are again ascribed to the polar gaps.
Opposite to the closed-loop test with all components, the triangle plot a) with only the along-track component reveals much smaller values with dominant accuracies of ca. 10^{-22}, above all for SH coefficients of lower orders. The trend of increasing accuracy with increasing degrees as well as the lines of lower values for the SH coefficients of order zero and orders $m = \pm 16, 32, 48$ as it is depicted in all the other closed-loop tests, can hardly be seen in this case. Instead, it seems that this time the sectorial SH coefficients reveal slightly higher differences and consequently a sectorial pattern can be seen in the plots b) – d).

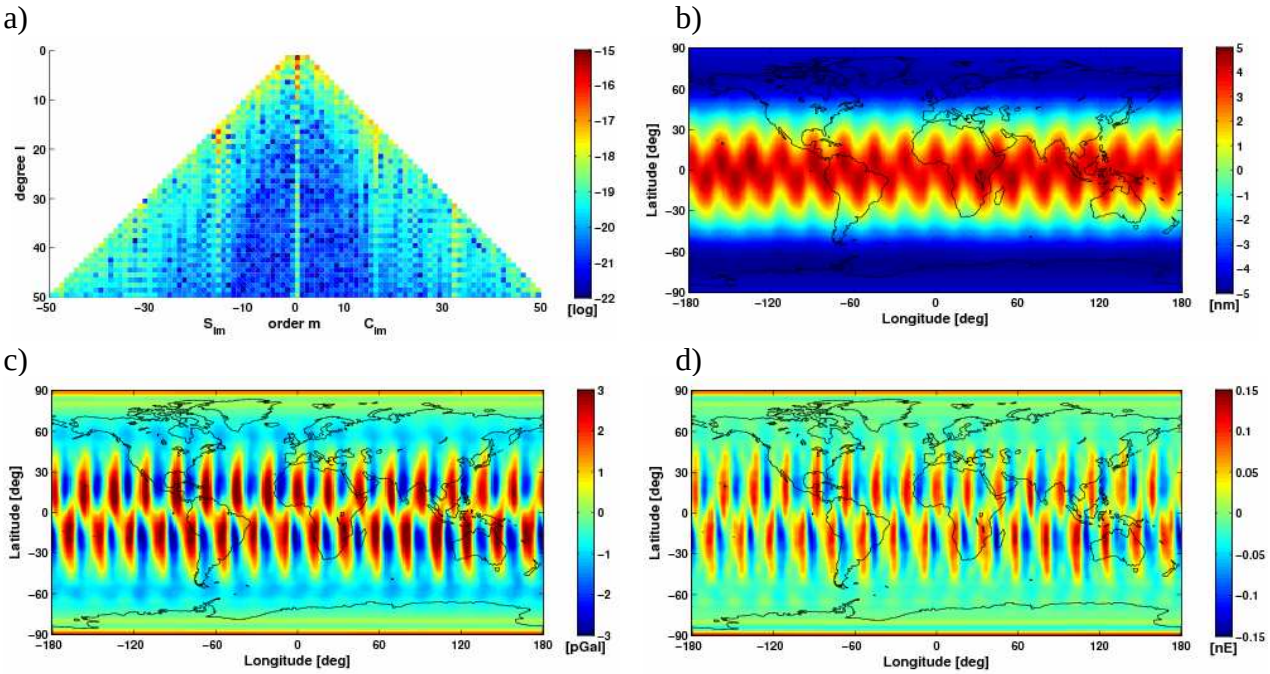

Figure 4.5: Differences between original EGM96 and estimated model (analysis with along-track signal component V_{xx}) in closed-loop test for a) SH triangle, b) geoid heights, c) gravity anomalies and d) radial gravity gradients.

The plot arrangements of the following two figures (Figure 4.6 and Figure 4.7) which belong to the two cases where the cross-track V_{yy} and the radial components V_{zz} were used in the analysis, reveal very similar features as in the case of applying all signal components. The triangle plots show again clear bands of higher differences for the SH coefficients of the orders $m = 0, \pm 16, 32, 48$. For the cross-track case (Figure 4.6, a), the band with differences around 10^{-18} up to 10^{-15} around the coefficients of zero order is comparably broader and includes also coefficients of up to the tenth order of sine and cosine. It becomes one narrow line with larger differences of 10^{-15} if only radial components are used (Figure 4.7, a). All the other plots b) – d) of the following two figures contain significant horizontal structures in west-east direction as they were already visible when all components were taken into account (Figure 4.4).
The corresponding statistics, however, differ a little bit. As already mentioned, applying V_{yy} only, leads to the maximal RMS values for the geoid heights, gravity anomalies and gravity gradients (Table 4.1). These values are only slightly improving if V_{zz} is used instead, with differences in the geoid height of *83.1nm*, in the gravity anomalies of *80.4pGal* and in the radial gravity gradients of *2.9nE*.

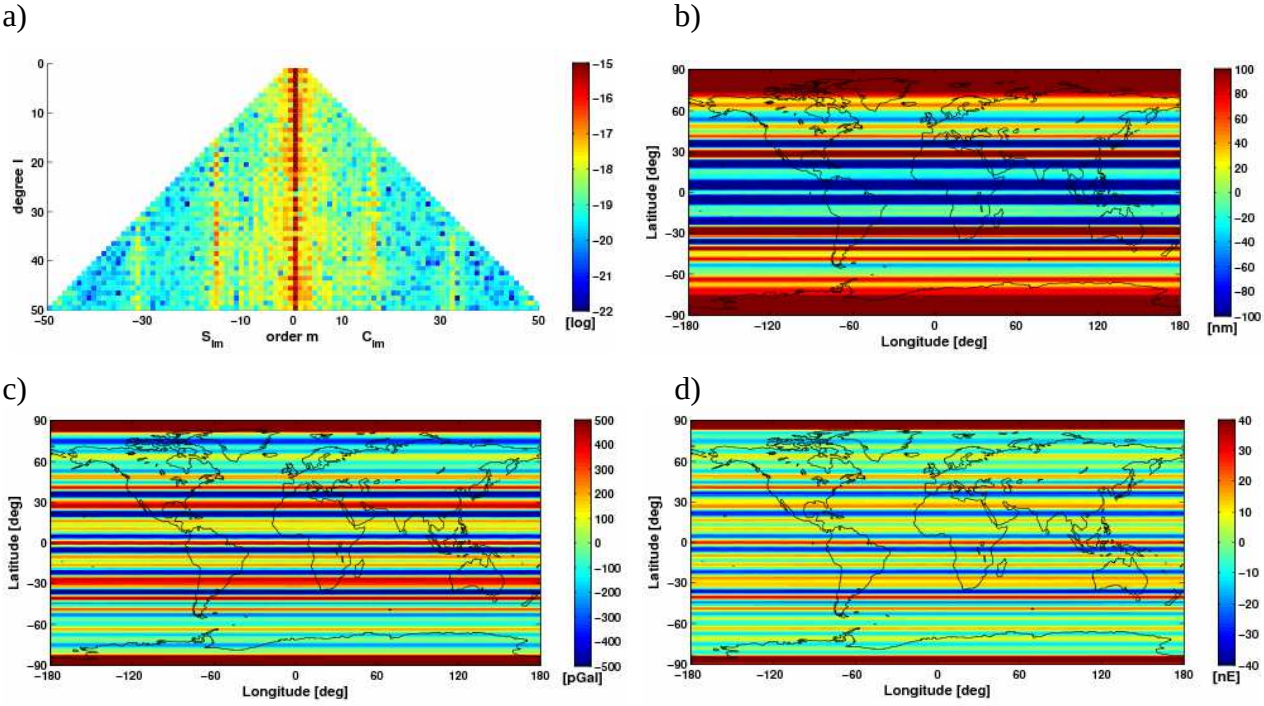

Figure 4.6: Differences between original EGM96 and estimated model (analysis with cross-track signal component V_{yy}) in closed-loop test for a) SH triangle, b) geoid heights, c) gravity anomalies and d) radial gravity gradients.

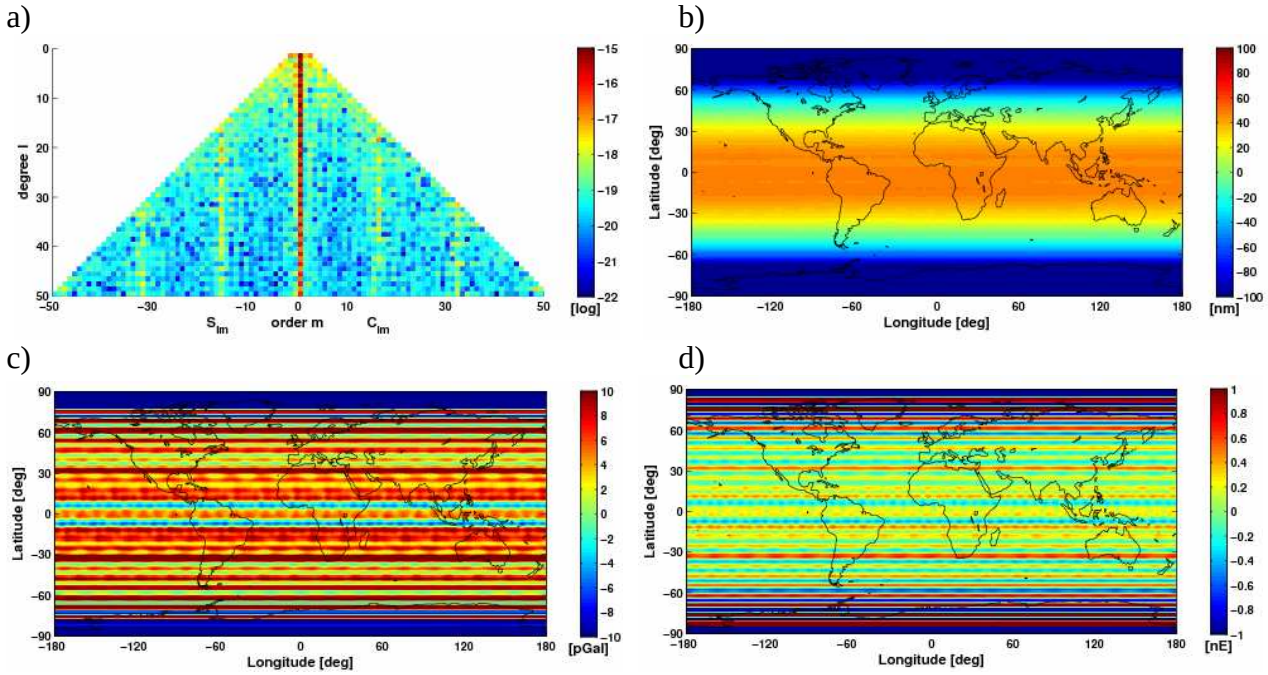

Figure 4.7: Differences between original EGM96 and estimated model (analysis with radial signal component V_{zz}) in closed-loop test for a) SH triangle, b) geoid heights, c) gravity anomalies and d) radial gravity gradients.

Applying all three signal components within the closed-loop tests is expected to lead to smaller differences between EGM96 and the estimated model than applying only one component since more observations are used for the analysis. However, in using the along-track component V_{xx} only, even more accurate models can be achieved within this study which deals with a noise-free scenario. This is mainly due to the polar gaps which have a minor influence on the along-track component but a greater impact on the cross-track and radial components and therefore also on the results of a combined solution. These effects are reflected by the more or less distinct features along the zonal SH coefficients in the triangle plots.
Furthermore, the closed-loop tests also indicate that no matter which signal component is applied within the analysis step, the differences between original and estimated model are within numerical accuracy of the computer.
In conclusion, the software packages *'create'* and *'adjust'* as well as the implied dataset can be deemed to be an appropriate basis for further investigation with respect to applied filters.

4.3 Along-track filtering

The next step of this study was to modify the generated satellite signal by applying one-dimensional along-track filters along the orbit to each of the three main components of the signal output tensor (Eq. 2.4). It should be noted that we are not interested in the actual filtering as filtering a noise-free signal is not reasonable. This study is rather interested in the different effects on the signal itself caused by filters.

Thus, the difference plots for all four quantities on model level will be first shown for the filtering of the along-track signal component V_{xx}, followed by plots for the cross-track component V_{yy} and the radial component V_{zz}. This makes it possible to compare the influences of filters on different signal components.
This section investigates the effects of two different filters, the boxcar and the Butterworth filter. For direct comparison and to keep the overview, only one filter setting with a cut-off frequency of one tenth of the Nyquist frequency ($f_c = 1/10 \cdot f_{Ny} = 10mHz$) and an order of two for the Butterworth filter, is chosen in the sequel. Both filters are shown in the spectral domain (Figure 4.8) as amplitude values dependent on the frequencies which are running from the fundamental to the Nyquist frequency. These filters will be applied to the Fourier transformed signal by multiplication in the spectral domain (detailed description, see section 2.3.1). It is evident that the transition of the Butterworth filter is much smoother than the boxcar filter but also manipulates the signal already for smaller frequencies than the cut-off frequency in contrast to the boxcar filter.
Further investigation on the influence of other filter settings will be presented in section 4.5.

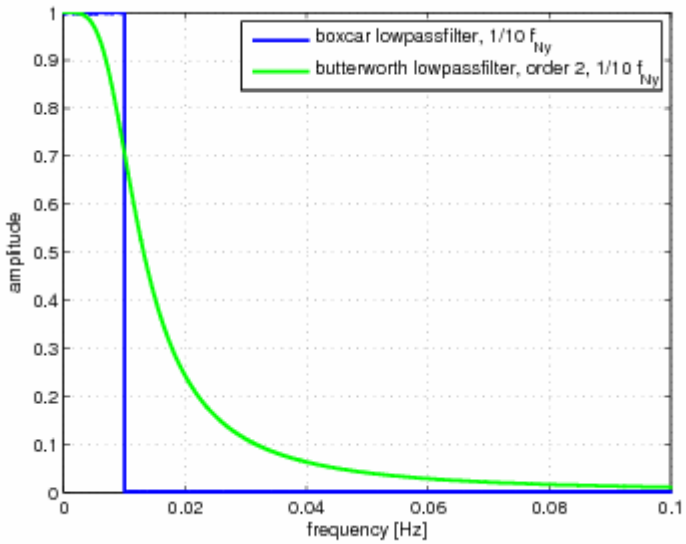

Figure 4.8: Along-track lowpass filter setups in spectral domain with cut-off frequency 1/10 of Nyquist frequency: boxcar filter (blue), Butterworth filter, order 2 (green)

The algorithm of the testing procedure for along-track filtering can be found in the flowchart in Figure 3.5.

BOXCAR FILTER At first, the filtered data will be compared to the reference data on signal level for all three components by putting the spectra of both square rooted power spectral densities (PSDs) side by side (flowchart in Figure 4.9).
Figure 4.10 shows the absolute square rooted PSDs in [$E/\sqrt{Hz}$] of the reference (blue) and filtered signal (red) for all components in the spectral domain versus frequencies ranging from the fundamental to the Nyquist frequency. Due to better visualization, the axes of these plots are presented on a logarithmic scale.

By comparing these spectra of the original and the filtered signal, it can be seen that the amplitudes within a frequency band from *10mHz* (cut-off frequency) to *100mHz* (Nyquist frequency) are cut-off by the boxcar filter. For higher frequencies than the cut-off frequency, the magnitudes of the filtered signal have values less than *1e-20 E*. For all other frequencies, the spectra of the reference and filtered signal are identical.

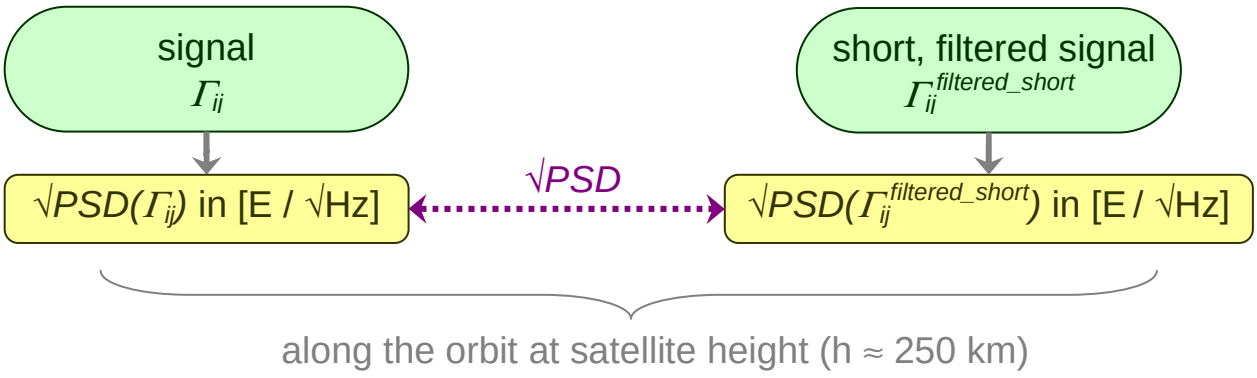

Figure 4.9: Flowchart for comparison of simulated signal from EGM96 model and from along-track filtered signal based on square root of power spectral densities (√PSD)

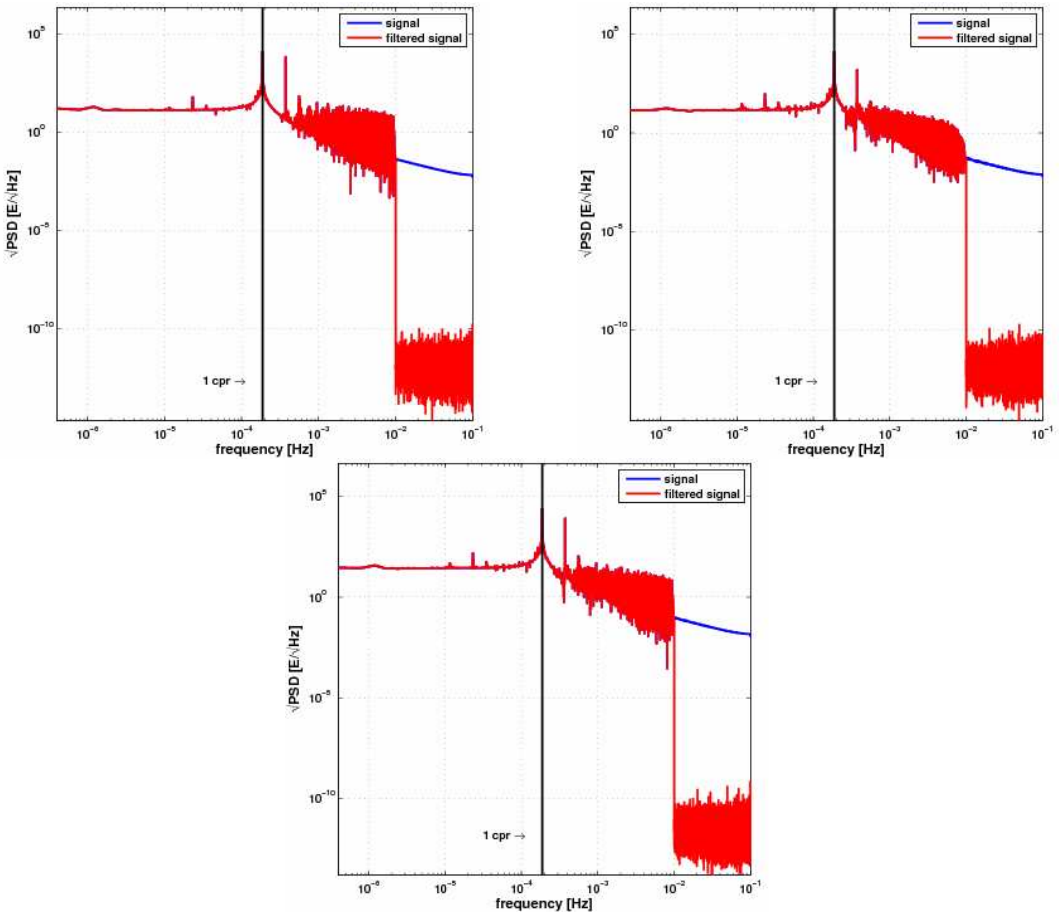

Figure 4.10: √PSD of along-track boxcar filtering of V_{xx} (top left), V_{yy} (top right) and V_{zz} (bottom) with cut-off frequency 1/10 of Nyquist frequency at signal level

In contrast to the comparison of absolute values on signal level, the assessment of the filter influences on geoid model level is based on interpreting the differences between original and estimated filtered models in the form of difference plots (see section 4.1 and Figure 4.11).

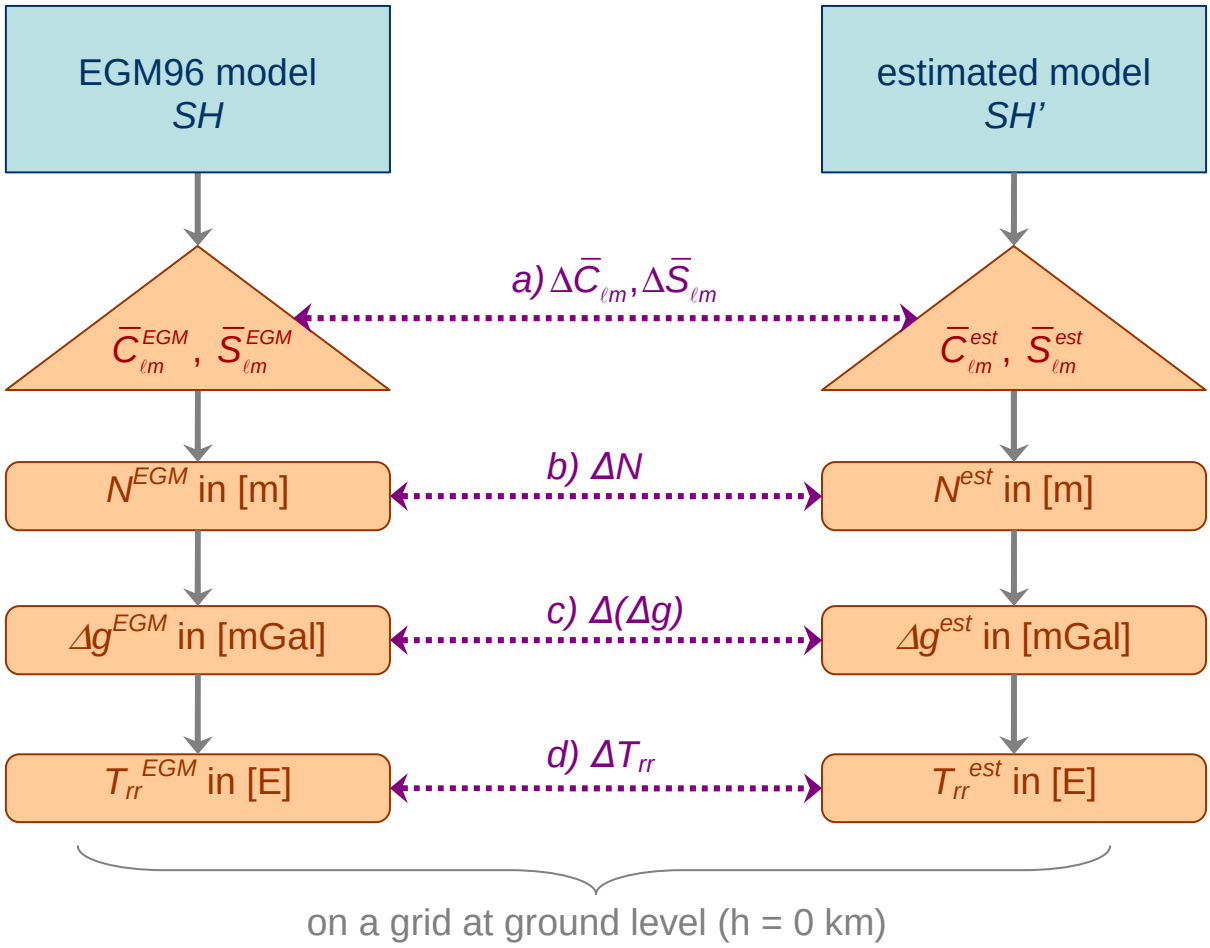

Figure 4.11: Flowchart for comparison of along-track filtering effects based on global models on the ground

The filtered signal had to be shortened on both sides of the time series in order to attenuate the transient phenomenon of the filter. An evidence of this effect can still be seen in the plots b) – d) in Figure 4.12. These plots reveal the differences of geoid heights, gravity anomalies and gravity gradients between the original EGM96 model and the model estimated from the boxcar filtered signal component V_{xx}. In all three cases, these effects appear mainly along the zero meridian with maxima and minima at a latitude of ca. 60 degrees on the North and South hemisphere. Since V_{xx} is the along-track component, the structures in the plots b) – d) as well as the maxima and minima are in alignment with the orbit and are therefore a little bit inclined with respect to the meridian. Due to the polar gaps and this inclination of the orbit, the South and the North pole are also evincing slightly higher differences between EGM96 and estimated model. The magnitudes of the peaks are approximately $\pm 80\mu m$ for the geoid height, $\pm 400nGal$ for the gravity anomaly and $\pm 30\mu E$ for the gravity gradient. The RMS values of differences between original and filtered model (Table 4.2)

are about one order of magnitude smaller with *2.9µm, 16.1nGal* and *1.2µE,* respectively. It seems that the actual filter effects of this specific boxcar filter with a cut-off frequency of one tenth of the Nyquist frequency are smaller than the warm-up effects. If using filters with smaller cut-off frequencies and thus higher influences on the signal, it is expected that the warm-up effects will be hidden by the filter effects.

The SH coefficient triangle in Figure 4.12 a) is mainly divided into two zones. The coefficients of orders between 30 and 50 show differences between the EGM96 and estimated model of 10^{-15} and smaller. On the other hand, there is an area of slightly higher differences up to 10^{-13} for lower order coefficients. As this difference triangle seems to be dependent on the SH order, one could get the impression that applying a one-dimensional boxcar filter to the signal is analogous to applying a two-dimensional spherical order filter to the model. This last assumption, however, has to be revised in the case of filtering the cross-track component V_{yy} of the signal.

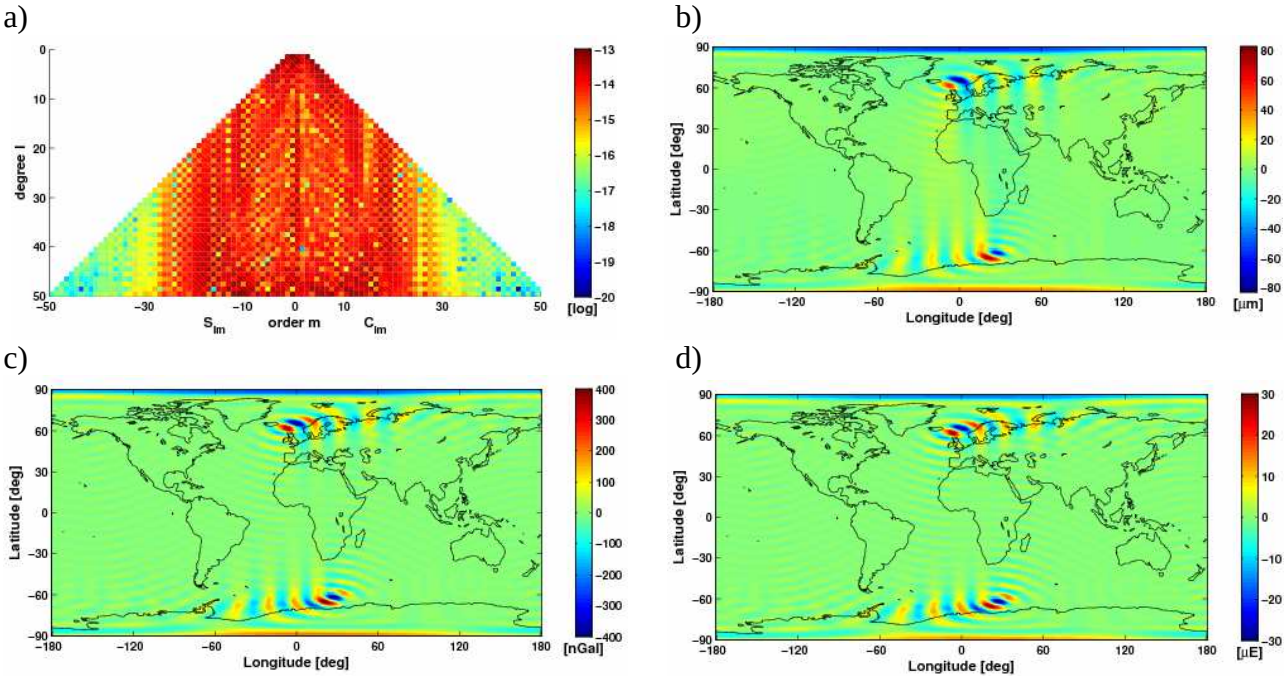

Figure 4.12: Along-track boxcar filtering of V_{xx} with cut-off frequency 1/10 of Nyquist frequency at model level

Table 4.2: RMS values for along-track boxcar filtering with cut-off frequency 1/10 of Nyquist frequency

signal components	RMS of ΔN [µm]	RMS of $\Delta(\Delta g)$ [nGal]	RMS of ΔT_{rr} [µE]
along-track V_{xx}	2.950	16.087	1.181
cross-track V_{yy}	7.221	48.453	3.774
radial V_{zz}	16.356	32.759	1.648

Table 4.2 shows higher differences in the RMS values for the cross-track than for the along-track component. The RMS of the differences in geoid height between EGM96 and estimated model is increasing from $2.95\mu m$ for V_{xx} to $7.22\mu m$ for V_{yy}. In the case of the gravity anomaly, there is an increase from $16.1nGal$ for V_{xx} to $48.5nGal$ for V_{yy} and with respect to the gravity gradients, using the cross-track component leads to a rise from$1.18\mu E$ for V_{xx} up to $3.77\mu E$ for V_{yy}.
As it was already mentioned in the discussion of the closed-loop tests, these higher differences in the RMS values are rather due to the lower power of the cross-track component of the signal compared to the along-track component, but less due to the influences of the boxcar filter. Little differences between the components V_{xx} and V_{yy} can be also recognized in Figure 4.13. Firstly, if the V_{yy} component is filtered, the maxima and minima in the plots b) – d) have significantly higher amplitudes with approximately $\pm 100\mu m$ for the geoid heights, $\pm 600nGal$ for the gravity anomalies and $\pm 45\mu E$ for the gravity gradients. Secondly, the features of the remaining transient filter oscillation are oriented in cross-track direction of the orbit instead of in along-track direction and therefore show a west-east trend. The triangle plot a) also presents a different structure which leads back to the refusal of the assumption that a one-dimensional boxcar filter could be analogously implemented as a two-dimensional order filter. The features in the SH triangle are looking more randomly for the filtered cross-track component with very small differences of up to 10^{-20} for the sectorial coefficients of degree and order higher than 15.

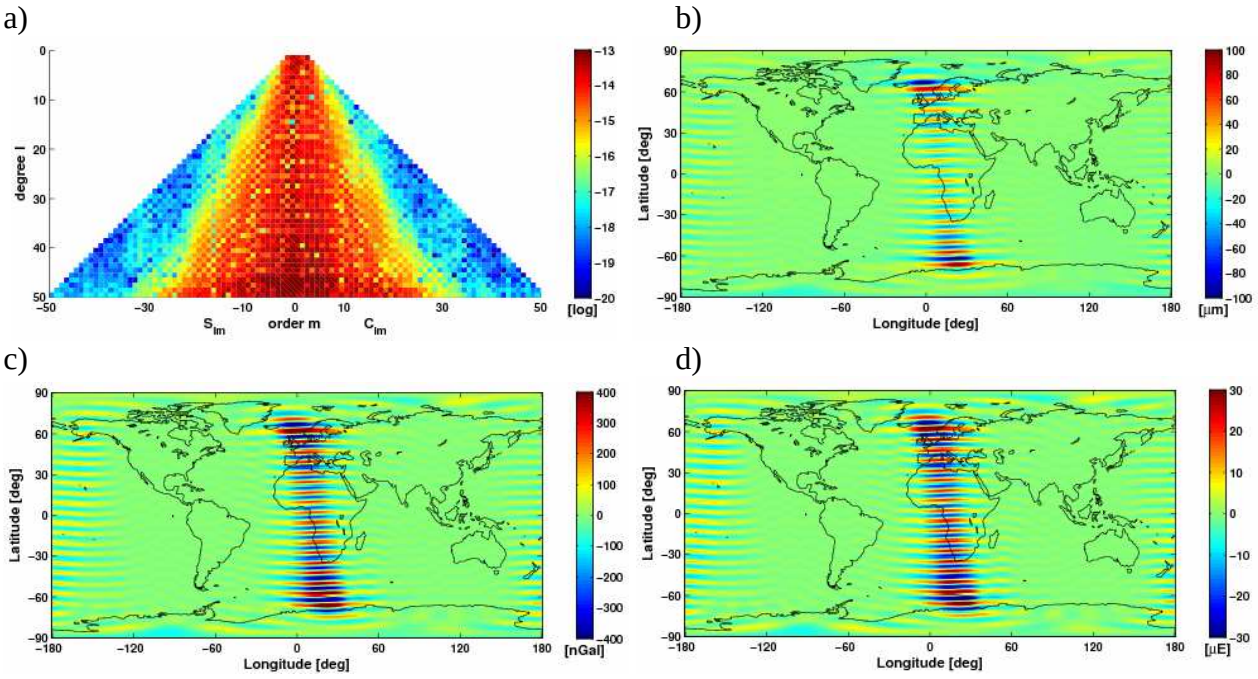

Figure 4.13: Along-track boxcar filtering of V_{yy} with cut-off frequency 1/10 of Nyquist frequency at model level

The third component to discuss is the radial component V_{zz} of the signal. If we take a look at Table 4.2, it can be noted that the boxcar filter seems to have the biggest influence on the radial component with respect to the geoid heights. Compared to the other components, the RMS of the differences in the geoid heights between EGM96 and filtered model becomes maximal with a value of $16.36\mu m$. The reason is that the boxcar filter completely eliminates the signal for all frequencies higher than the cut-off frequency. Thus, as the radial component has the highest

average power, filtering this signal component with a boxcar filter will have the most significant impact on the filtered signal itself and with it on the differences between EGM96 and the estimated model. As the gravity anomalies and gravity gradients are derivatives of the potential and thus, the higher frequencies are amplified, it is consequently expected that more signal is filtered. This would cause even higher differences for gravity anomalies and gravity gradients if the radial component is used. However, the RMS values for both quantities lie between the RMS values for the along-track and cross-track components with respect to the gravity anomalies with *32.76nGal* and with respect to the gravity gradients with $1.65\mu E$.

The corresponding plots in Figure 4.14 b) – d) show similar structures as in the plots of the filtered along-track component V_{xx} with peaks in small regions along the orbit around the meridian at latitudes of ±60 degrees. The graph d) for the radial gravity gradients $V_{rr} = V_{zz}$ is actually the only one which visualizes the estimated model in the same direction in which the signal has been filtered. It should be also noted that the minimum at the South Pole as well as the maximum at the North Pole have increased their magnitudes in all three quantities. The SH triangle of V_{zz} looks very similar to this of V_{yy} with a band of lower differences of ca 10^{-20} along the sectorial coefficients and with higher differences of up to 10^{-13} along the zonal coefficients.

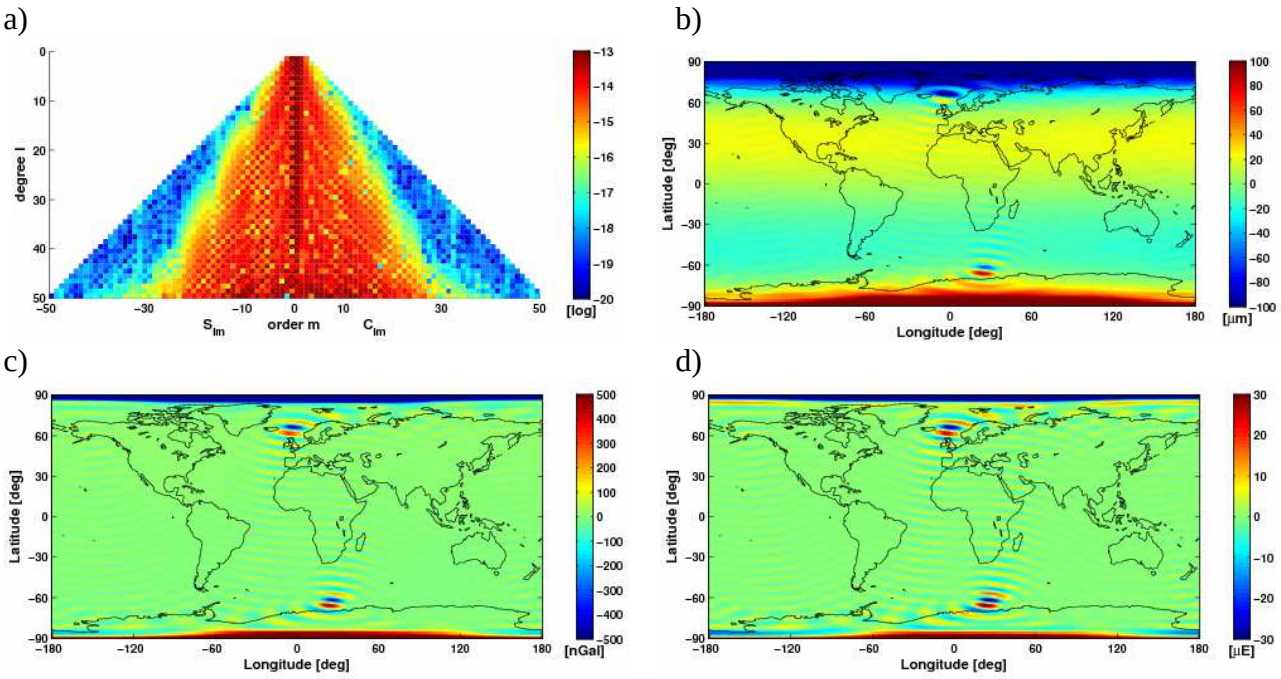

Figure 4.14: Along-track boxcar filtering of V_{zz} with cut-off frequency 1/10 of Nyquist frequency at model level

BUTTERWORTH FILTER The second part of the along-track filtering investigation deals with the application of a Butterworth filter of order two. The different effects will be discussed again on signal and on model level. The same cut-off frequency of one tenth of the Nyquist frequency (*10mHz*) is used.
Table 4.3 shows the RMS values of the differences between the original EGM96 model and the model which is estimated from the Butterworth filtered signal components V_{xx}, V_{yy} and V_{zz} with respect to geoid heights ΔN, to gravity anomalies $\Delta(\Delta g)$ and to the radial gravity gradients ΔT_{rr}.
In comparison to the result of the boxcar filter in Table 4.2, it sticks out that the RMS values are about four orders of magnitudes higher. This time, filtering the radial signal component V_{zz} leads to the maximum differences with *14.4cm* for the geoid height and *0.21mGal* for the gravity anomaly. The maximum difference for the gravity gradient with *0.014E* was achieved by filtering the along-track component V_{xx}. On the other hand, filtering the cross-track component V_{yy} leads to the minimum differences for all three quantities on a grid with *2.62cm, 0.17mGal* and *0.012E*.

Table 4.3: RMS values for along-track Butterworth filtering (order 2) with cut-off frequency 1/10 of Nyquist frequency

signal components	RMS of ΔN [cm]	RMS of $\Delta(\Delta g)$ [mGal]	RMS of ΔT_{rr} [E]
along-track V_{xx}	3.479	0.193	0.014
cross-track V_{yy}	2.618	0.165	0.012
radial V_{zz}	14.411	0.206	0.013

From Table 4.3 it can be firstly concluded that the Butterworth filter is much more aggressive than the boxcar filter. This fact can be also seen in the corresponding plots of the PSDs for all three components of the reference and filtered signal in Figure 4.15. Although the Butterworth filter itself does not hold such a sharp edge as the boxcar filter (Figure 4.8) at the cut-off frequency of *10mHz*, it already starts to modify the signal and reduces the amplitude for frequencies smaller than the cut-off frequency where the √PSD amplitude of the signal is strongly oscillating. The boxcar filter, however, only cuts the relatively low and monotonic √PSD part of the signal for frequencies higher than *10mHz*. That is the reason for achieving significantly higher differences between original and estimated model.
The second point of the conclusion is that filtering the cross-track component will have the smallest influence on the estimated model. The reason is that this signal component V_{yy} has the lowest power compared to the other components and thus, the power loss by filtering will be less. This is especially the case for the Butterworth filter since most of the √PSD is concentrated in the band of frequencies lower than *10mHz*.

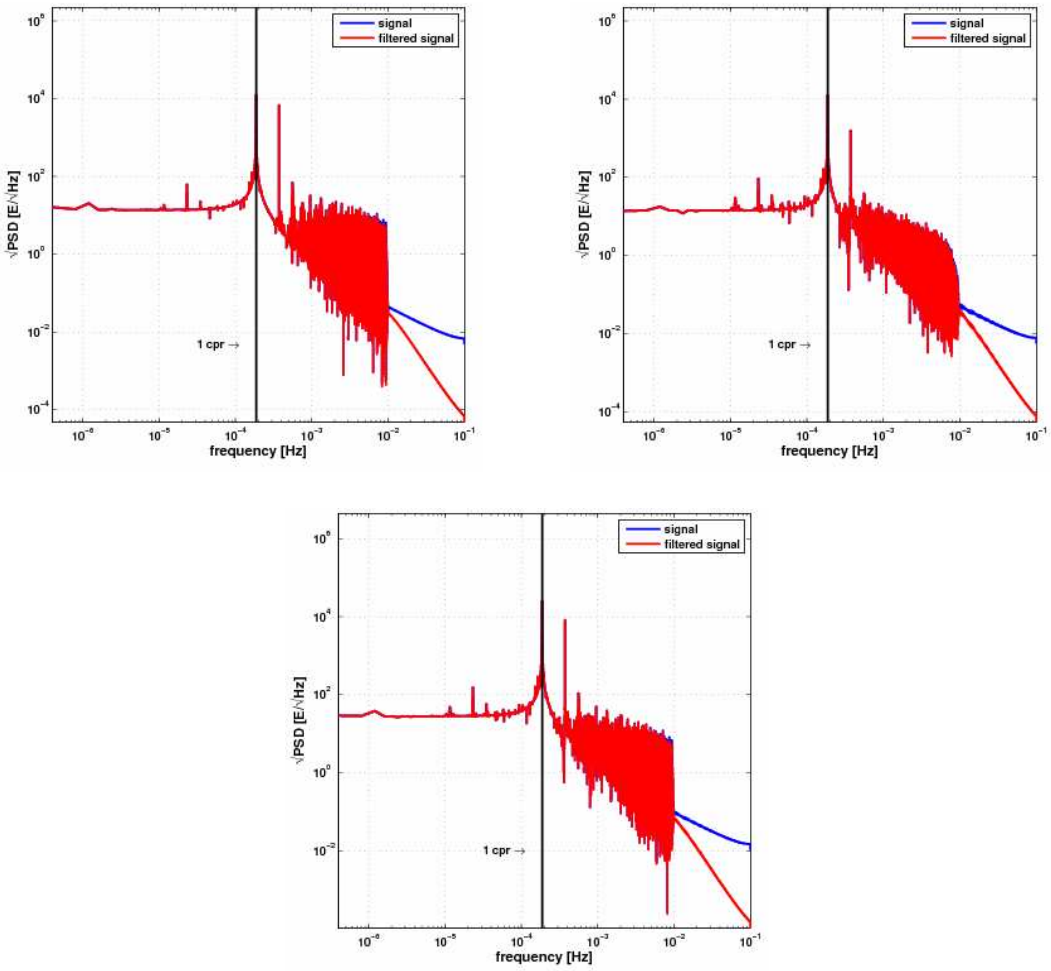

Figure 4.15: √PSD of along-track Butterworth filtering (order 2) of V_{xx} (top left), V_{yy} (top right) and V_{zz} (bottom) with cut-off frequency 1/10 of Nyquist frequency at signal level

Figure 4.16 shows again the differences between the original EGM96 and the estimated model derived from the Butterworth filtered along-track signal component with respect to the four different quantities. The features in all four subplots look more random compared to those of the boxcar filtered results in Figure 4.12 since all frequencies are affected equally. The differences with values up to 10^{-9} presented in the SH triangle with respect to Butterworth filtering are essentially higher for nearly all degrees and orders. Moreover, the sectorial coefficients have slightly smaller values with 10^{-11} to 10^{-10}. Few coefficients reach minimum differences of about 10^{-14} which is about six magnitudes worse than applying the boxcar filter.

In the differences of the geoid heights (subplot b), there are also much finer features inherent distributed over the whole grid of the Earth with maxima and minima of up to $\pm 0.9m$ which can be mainly seen in the Himalaya region, in the Caucasus Mountains and along the Andes. These features are even getting finer with every further derivation of the potential, i.e., for the gravity anomalies (subplot c) and the radial gravity gradients (subplot d).

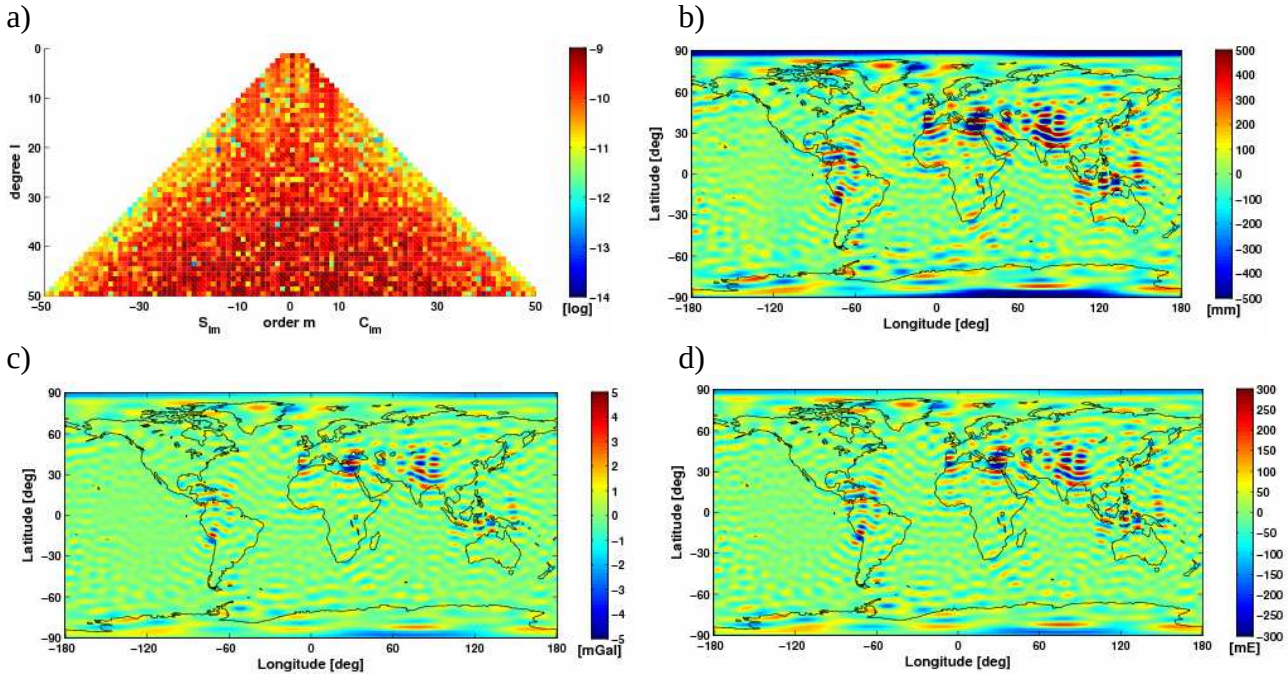

Figure 4.16: Along-track Butterworth filtering (order 2) of V_{xx} with cut-off frequency 1/10 of Nyquist frequency at model level

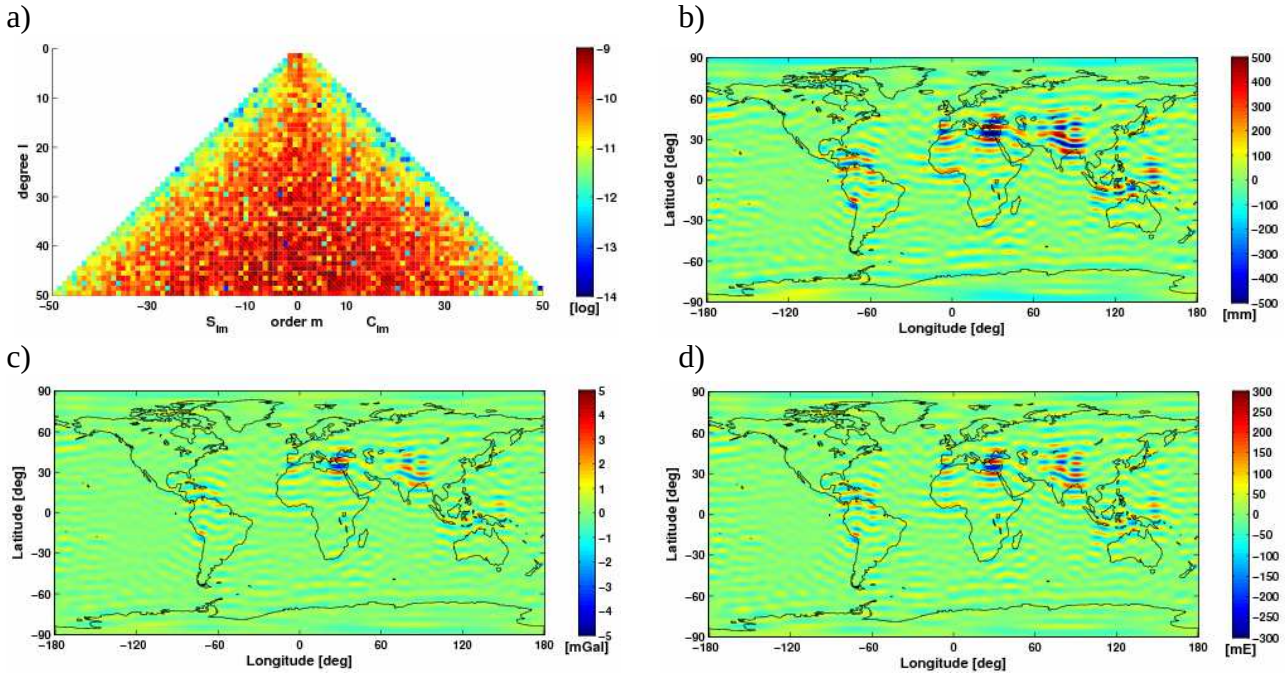

Figure 4.17: Along-track Butterworth filtering (order 2) of V_{yy} with cut-off frequency 1/10 of f_{Ny} at model level

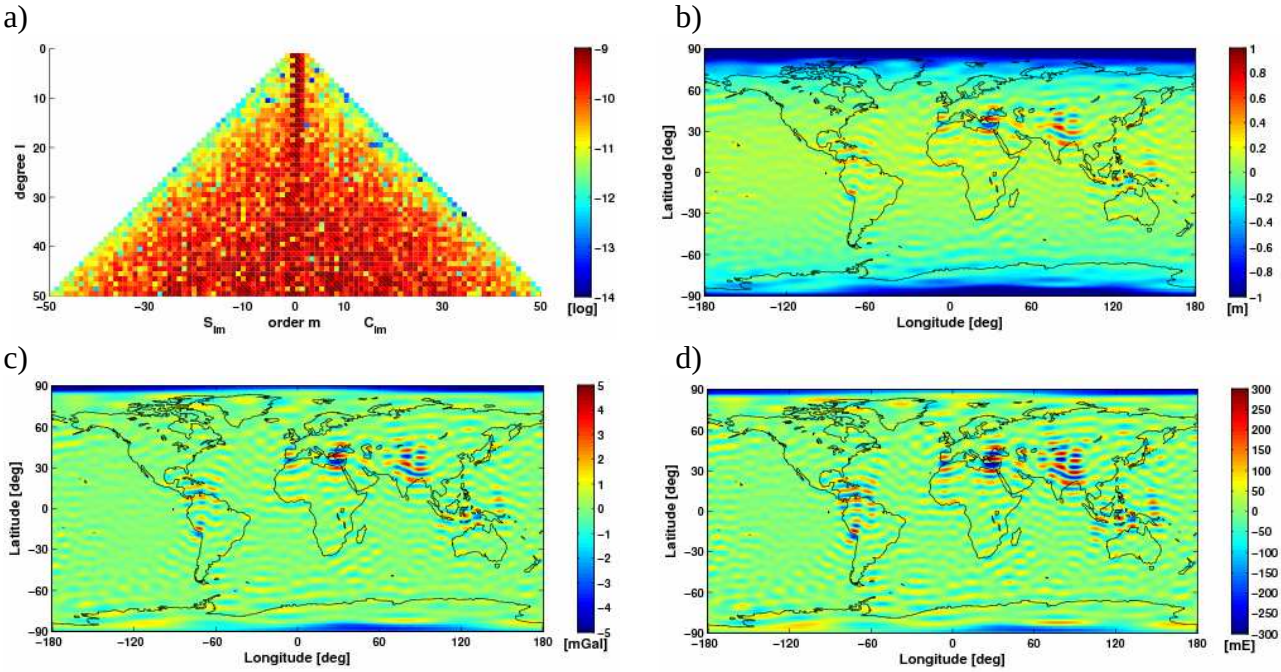

Figure 4.18: Along-track Butterworth filtering (order 2) of V_{zz} with cut-off frequency 1/10 of f_{Ny} at model level

The both previous graphs for the other cases, where the Butterworth filter was applied to the cross-track component V_{yy} (Figure 4.17) as well as to the radial component V_{zz} (Figure 4.18), are evincing similar features compared to the results from filtering the along-track component V_{xx}. As it was shown in Table 4.3, mainly the statistics are different.
In Figure 4.18, it is evident that the differences for the geoid heights are relatively high. The reason is that the effects of the Earth ellipsoidal field start to show up. These effects are even increased if a Butterworth filter of lower cut-off frequency is chosen as it will be revealed for a cut-off frequency of 1/200 of the Nyquist frequency in section 4.5.1. This problem can be solved by filtering the disturbing potential instead of the full gravitational potential.

4.4 Spherical filtering

The third test scenario, apart from the closed-loop tests and test for the one-dimensional along-track filtering of the simulated signal, is the two-dimensional spherical filtering of the EGM96 model. This step was implemented by designing a spherical boxcar filter on the one hand and a spherical Butterworth filter of order 2 on the other hand which are supposed to work as so-called degree filters. That means that the spherical harmonic coefficients of the original EGM96 model will be modified by applying these filter functions to the corresponding SH triangle depending on the degree of the coefficients. The testing procedure itself has been already explained in section 3.3.3.

At first, the effects of the filters will be examined in the spectral domain with respect to square roots of the power spectral densities (√PSD in E/√Hz) of the three different signal components,

along-track V_{xx}, cross-track V_{yy} and radial V_{zz}. The simulated signal tensor based on the original model is compared with the spherical filtered EGM96 model (Figure 4.19).
Furthermore, the difference plots between both models will be also analysed. The relationship of the corresponding quantities is visualized in the flowchart in Figure 4.20 and details can be found in the explanation of the reference data in section 4.1.

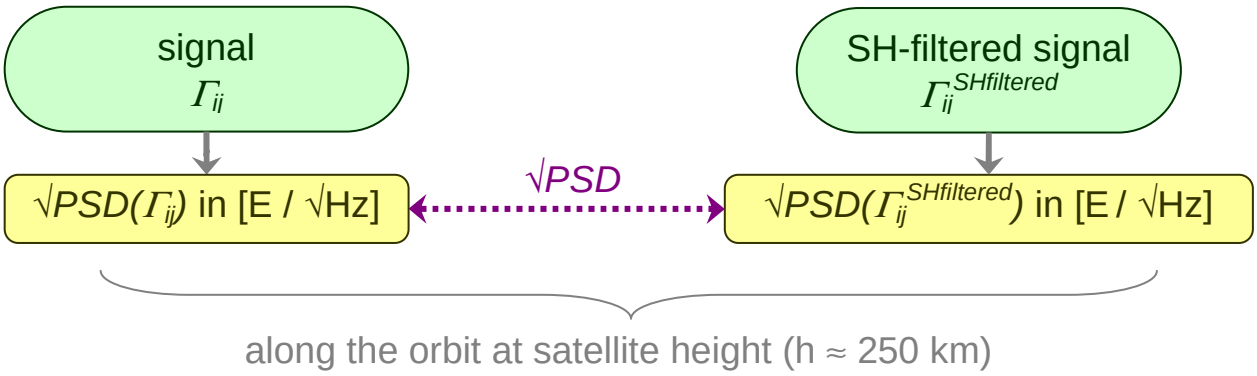

Figure 4.19: Flowchart for comparison of simulated signal from EGM96 model and from spherical filtered model based on square root of power spectral densities (√PSD)

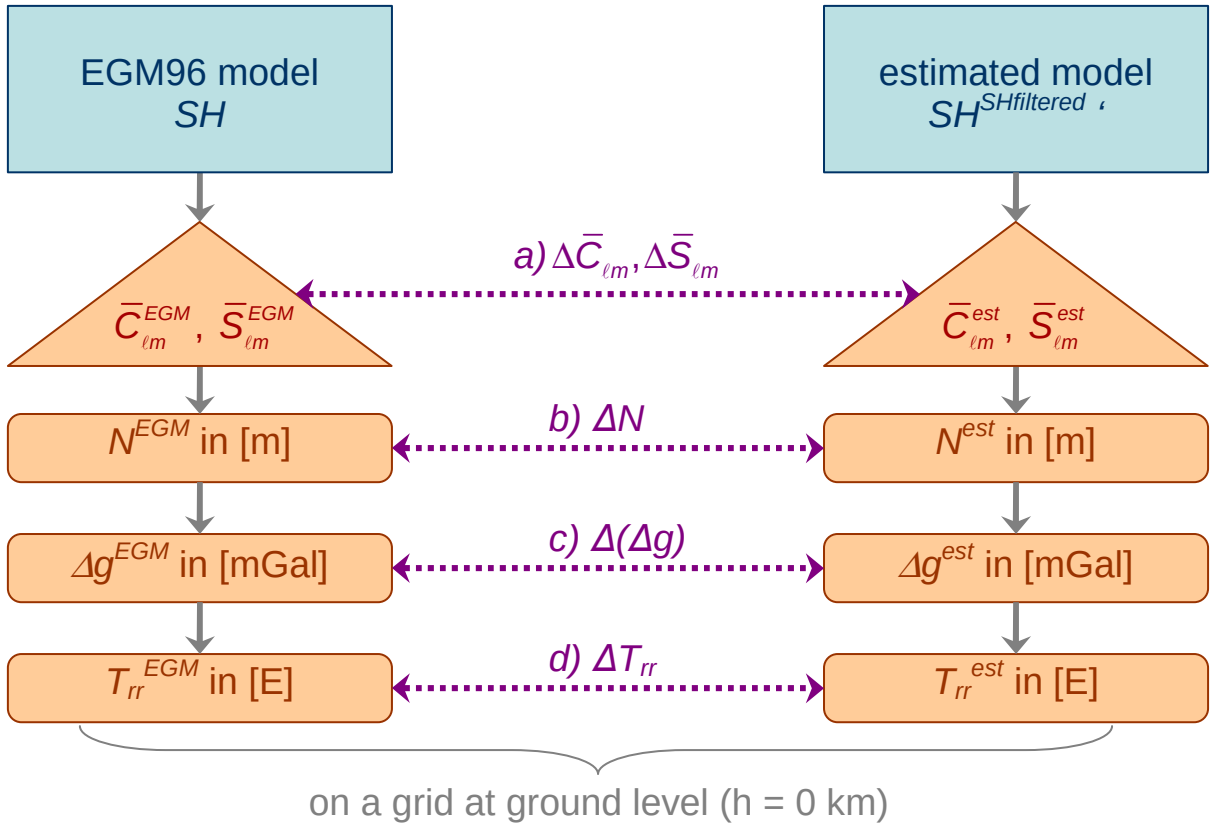

Figure 4.20: Flowchart for comparison of spherical harmonic filtering effects based on global models on the ground

As it was already done for the along-track filters, only one filter setup is chosen within this section in order to investigate the different influences of the two filter types and the effects on the varying signal components. The cut-off for both filters was chosen at 35 degrees in the case of an EGM96 model of maximal degree and order of 50.
The boxcar as well as the Butterworth filter are presented in Figure 4.21 based on the SH coefficients within a triangle plot. In the same way as it was recognized for the along-track filters, it is obvious that the Butterworth filter has a smoother transition than the boxcar filter but also manipulates the coefficients already for lower degrees. While the SH filter coefficients of the latter are either unaltered or zero which will therefore lead to a sharp edge on the cut-off degree of 35, the SH filter coefficients of the Butterworth filter are slowly decreasing from 1.0 to 0.45 with increasing degrees from 1 to 50. Since both filters are not order but degree filters, the coefficients of same order will all have the same filter value. These spherical filters will be applied to the spherical harmonic coefficients of the EGM96 model by multiplication (detailed description, see section 2.3.2).
Further investigation on the influence of other filter settings will be presented in section 4.5.

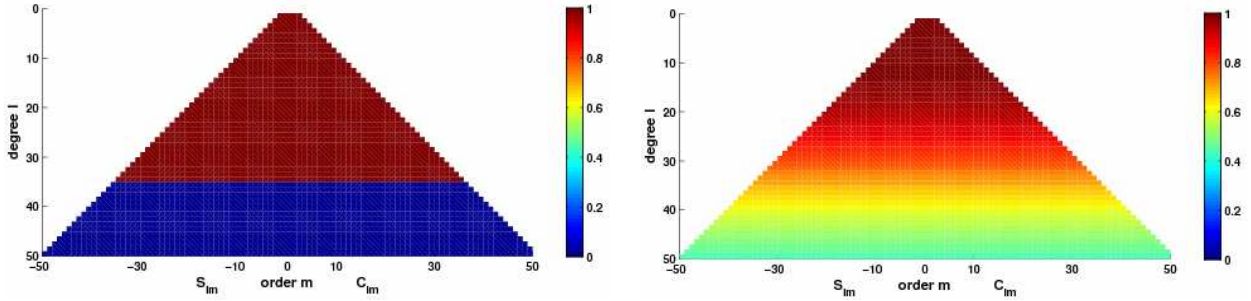

Figure 4.21: Spherical lowpass filter setups as SH coefficient triangles with cut-off degree of $l_c=35$: boxcar filter (left), Butterworth filter, order 2 (right)

BOXCAR FILTER Let us first have a look at the three square rooted PSD plots (Figure 4.22) of the three different signal components. This signal has been simulated based on the spherical boxcar filtered EGM96 model with the cut-off degree $l_c=35$. The first aspect which attracts attention is that for the lower frequencies of up to approximately the second peak at *0.4 mHz*, the √PSD of the estimated signal from the EGM96 model is hardly modified by filtering the SH coefficients. Especially for the along-track component V_{xx}, the √PSD differences between simulated original and filtered signal are minimal in this frequency band. The second point is that the strictly monotonic decreasing non-oscillating tails for frequencies of about *10 mHz* up to *100 mHz* are almost identical for the original and the filtered signal. The cut-off degree of $l_c=35$ mainly reduces the power of the original signal for frequencies from the second peak at around *0.4 mHz* on and depresses the oscillation of the original signal from ca. *7 mHz* on. Thus, a spherical lowpass degree filter in the boxcar form seems to have an influence on the reference signal which is comparable to applying an along-track bandstop filter.
Since not every signal component was filtered separately as it was done for the along-track filtering but are simply derived from the simulated signal tensor based on an overall filtering of all SH coefficients up to degree and order of 50, this type of filtering influences all three signal

components in the same way. This assumption can not only be confirmed by the three very similar √PSD plots, but also by the following statistics in Table 4.4 and the corresponding difference plots.

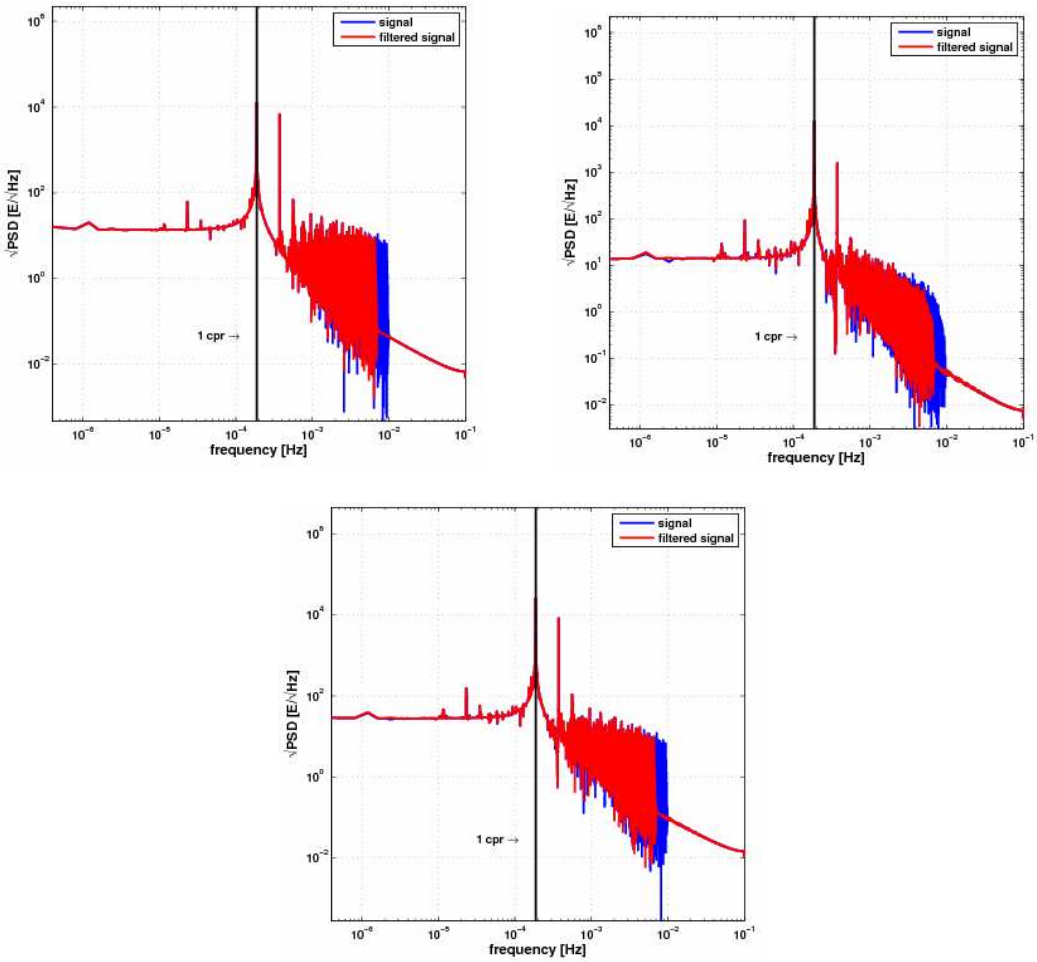

Figure 4.22: √PSD of simulated signal components V_{xx} (top left), V_{yy} (top right) and V_{zz} (bottom) based on spherical boxcar filtering of the EGM96 model with cut-off degree of l_c=35

Table 4.4 presents the RMS values of the differences in geoid heights, gravity anomalies and radial gravity gradients for each component which have been derived from the original EGM96 model and from the estimated model. In fact, the statistics of all three signal components are very close to each other. For example, the change in the RMS value of the geoid height if using the cross-track instead of the along-track component is only around *20nm*. The very small changes between the signal components are probably caused by the closed-loop and lie within the numerical accuracy of the computer. The RMS values for the geoid heights are approximately *26.4cm*, for the gravity anomalies *1.68mGal* and for the gravity gradients *0.12E*. With respect to the absolute values of the corresponding EGM96 quantities, these differences are still smaller than 3%.

Table 4.4: RMS values for spherical boxcar filtering with cut-off degree of $l_c=35$

signal components	RMS of ΔN [cm]	RMS of $\Delta(\Delta g)$ [mGal]	RMS of ΔT_{rr} [E]
along-track V_{xx}	26.366	1.676	0.123
cross-track V_{yy}	26.366	1.676	0.123
radial V_{zz}	26.366	1.676	0.123

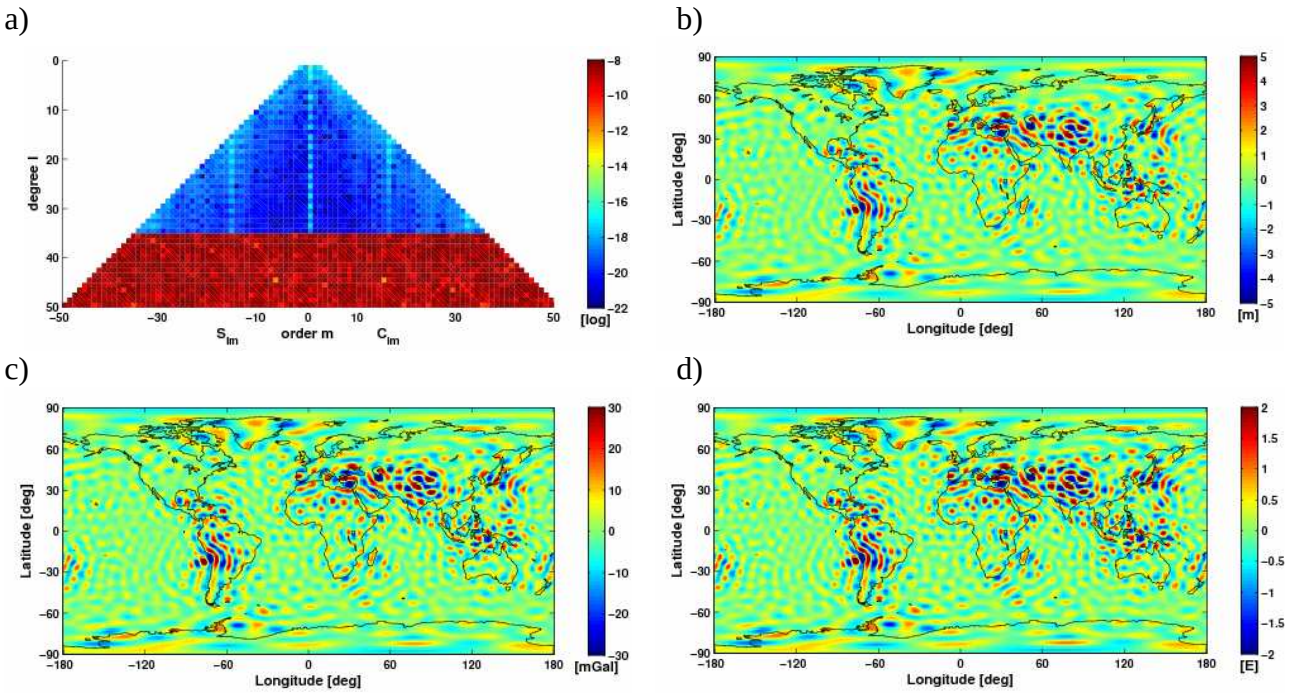

Figure 4.23: Spherical boxcar filtering (V_{xx}) with cut-off degree of $l_c=35$ at model level

With respect to the corresponding difference plots for geoid height b), gravity anomaly c) and gravity gradient d) in Figure 4.23 - Figure 4.25, it is evident that the occurring features are virtually identical for all three signal components. Some small variations between the components can be seen in the triangle plots a), although these plots are more influenced by the high differences of up to 10^{-8} in the SH coefficients from degrees 30 up to 50. For lower orders, the differences are smaller with values from 10^{-22} to 10^{-18} but present maxima of 10^{-16} for coefficients of order zero, ± 16 and ± 32 due to orbit resonances. For the cross-track component (Figure 4.24 a), however, these features are spreading out to the neighbouring SH coefficients.

The difference plots b) – d) on the grid show some striking features of maxima and minima, for example above the Himalaya and the Andes, with magnitudes of about ± 8 *m* for the geoid heights, ± 50 *mGal* for the gravity anomalies and ± 3 *E* for the gravity gradients. These features are very fine with higher frequencies inherent. This characteristic is enhanced by the filter design since the

spherical boxcar filter completely cuts the SH coefficients of the EGM96 from degree 35 to 50 and lets the other ones unchanged. Thus, by plotting the differences between EGM96 and estimated model, the resulting features on the grid directly reflect the EGM96 model for coefficients of order 35 to 50 together with the very small differences resulting from the closed-loop.

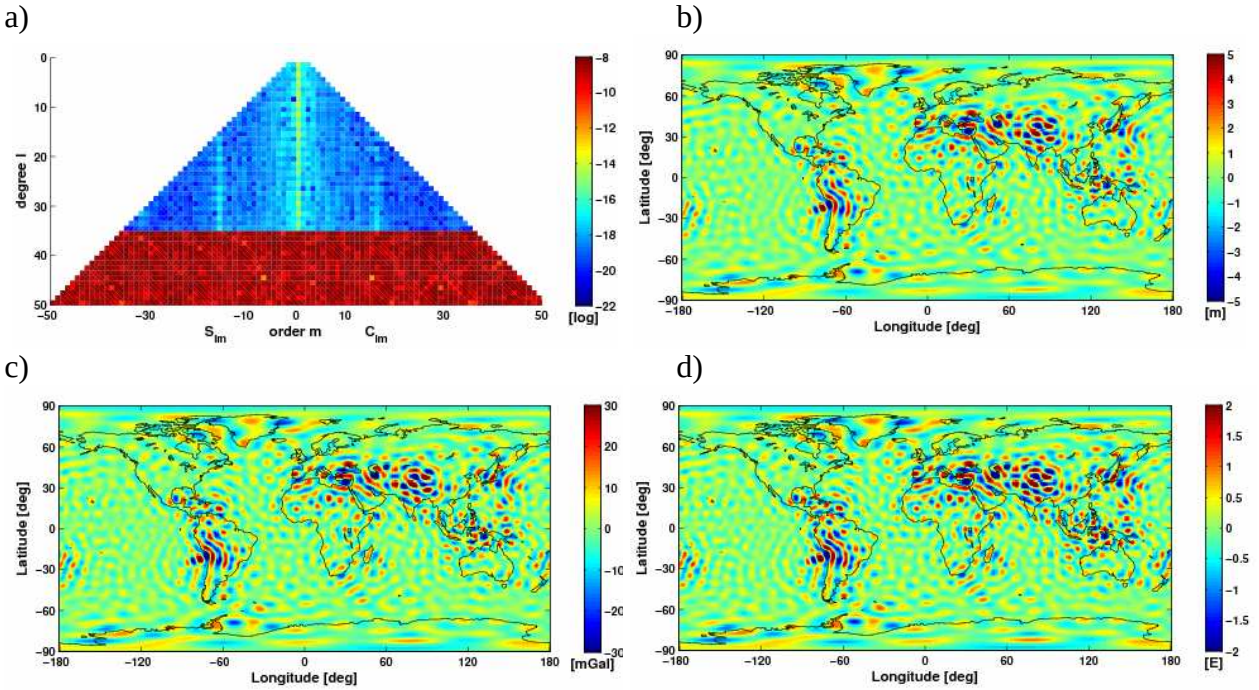

Figure 4.24: Spherical boxcar filtering (V_{yy}) with cut-off degree $l_c=35$ at model level

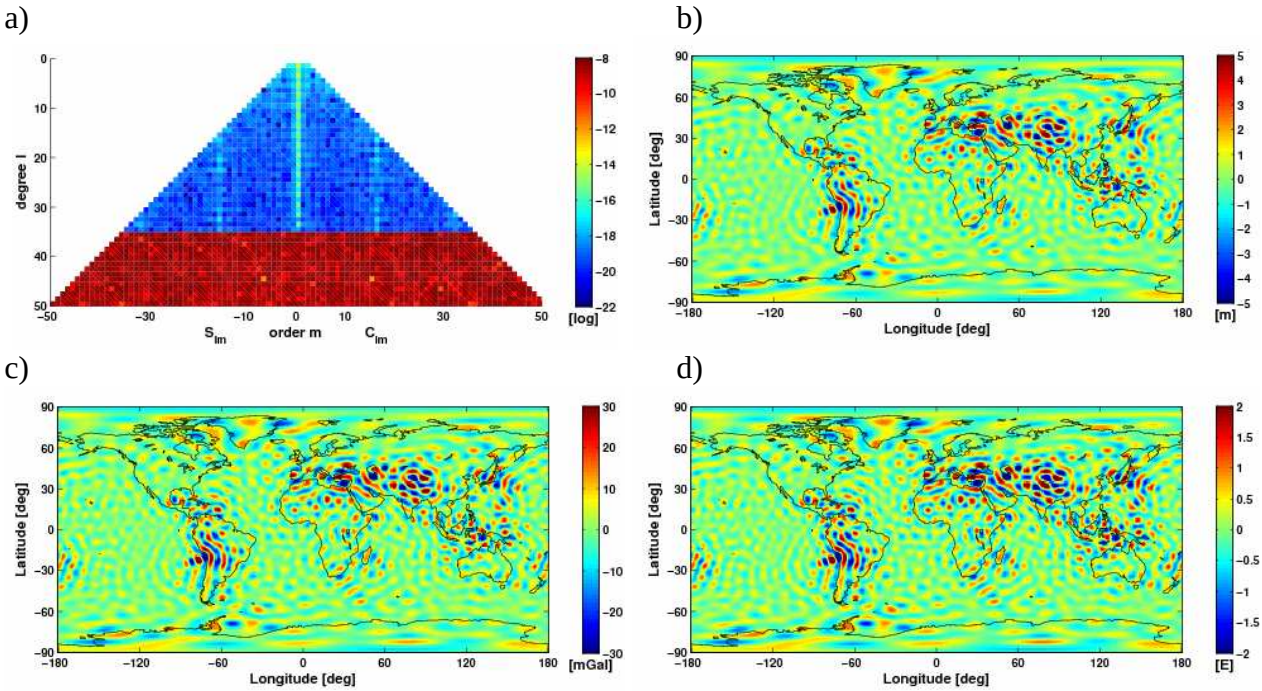

Figure 4.25: Spherical boxcar filtering (V_{zz}) with cut-off degree $l_c=35$ at model level

BUTTERWORTH FILTER Another interesting aspect of the spherical harmonic filtering tests is the comparison of the results from the two different filter types: the Butterworth and the boxcar filter. In comparison with the effects of the boxcar filter, the Butterworth filter of order 2 seems to be less aggressive.

The square rooted PSD plots for all three signal components in the following Figure 4.26 show that the spherical Butterworth filter decreases more and more the range of √PSD oscillations of the simulated original signal for frequencies between *0.4mHz* and *100mHz.* In contrast to the spherical boxcar filter, it does not completely depress the oscillations from ca. *7 mHz* on (Figure 4.22). The reason is that the Butterworth filter design is much smoother and does not lead to an abrupt and complete cut-off as it is caused by a boxcar filter (Figure 4.21).

Therefore, the boxcar filter directly applied to the SH coefficients seems to have a higher influence on the reference data than the Butterworth filter.

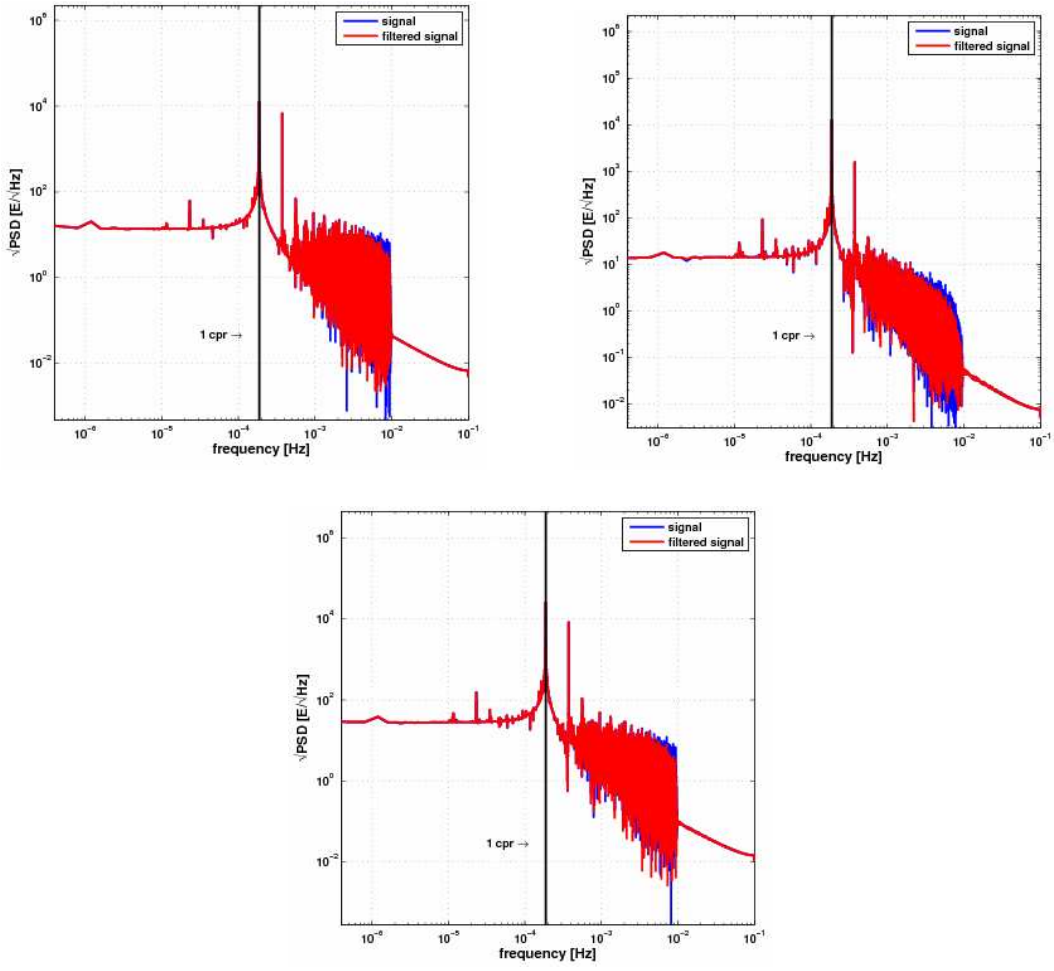

Figure 4.26: √PSD of simulated signal components V_{xx}, V_{yy} and V_{zz} based on spherical Butterworth filtering (order 2) of the EGM96 model with cut-off degree of l_c=35

As it is shown in Table 4.5, the RMS values of the differences between original and estimated model quantities are indeed becoming smaller in the case of applying the spherical Butterworth instead of the boxcar filter with about *15.4 cm* for the geoid heights, *0.88 mGal* for the gravity

anomalies and *0.062* E for the radial gravity gradients. Again, the spherical Butterworth filter affects all signal components in almost the same way.

Table 4.5: RMS values for spherical Butterworth filtering (order 2) with cut-off degree of $l_c=35$

signal components	RMS of ΔN [cm]	RMS of $\Delta(\Delta g)$ [mGal]	RMS of ΔT_{rr} [E]
along-track V_{xx}	15.436	0.885	0.062
cross-track V_{yy}	15.436	0.885	0.062
radial V_{zz}	15.436	0.885	0.062

These RMS values have been computed based on the differences between the original EGM96 and the estimated model. Regarding the corresponding features plotted as geoid heights, gravity anomalies and gravity gradients on a grid at ground level in Figure 4.27 - Figure 4.29, it can be deduced that also the Butterworth filter will influence all signal components in a very similar way. There are no visible differences between these plots as well as in the triangle plots of the SH coefficients. Apart from the significantly smaller magnitudes, the features in the subplots b) – d) look similar to those of applying the spherical boxcar filter even though the latter might be slightly coarser. As already mentioned, the reason is that the Butterworth filter design circumvents a sharp edge and thus reduces higher frequency ripples and ringing (Gibbs' phenomenon) throughout the grid plots. Even the dense regions of alternating minima and maxima, for example in the Himalaya and in the Andes, seem to be more blurry for the Butterworth filter. In these areas, the magnitudes are fluctuating between values of about $\pm 5\ m$ for the geoid heights, $\pm 25\ mGal$ for the gravity anomalies and $\pm 2\ E$ for the gravity gradients. Even though these peaks and the RMS values are lower for the Butterworth than for the boxcar filter, it is the other way round for the triangle plots in the subplots a). They show much higher differences of up to 10^{-8} for almost all SH coefficients in the case of a Butterworth filter. Beside some rare coefficients in between with minimum values of 10^{-15}, only some coefficients with a degree smaller than approximately *10*, present a slight decrease in differences with values of about 10^{-11}.

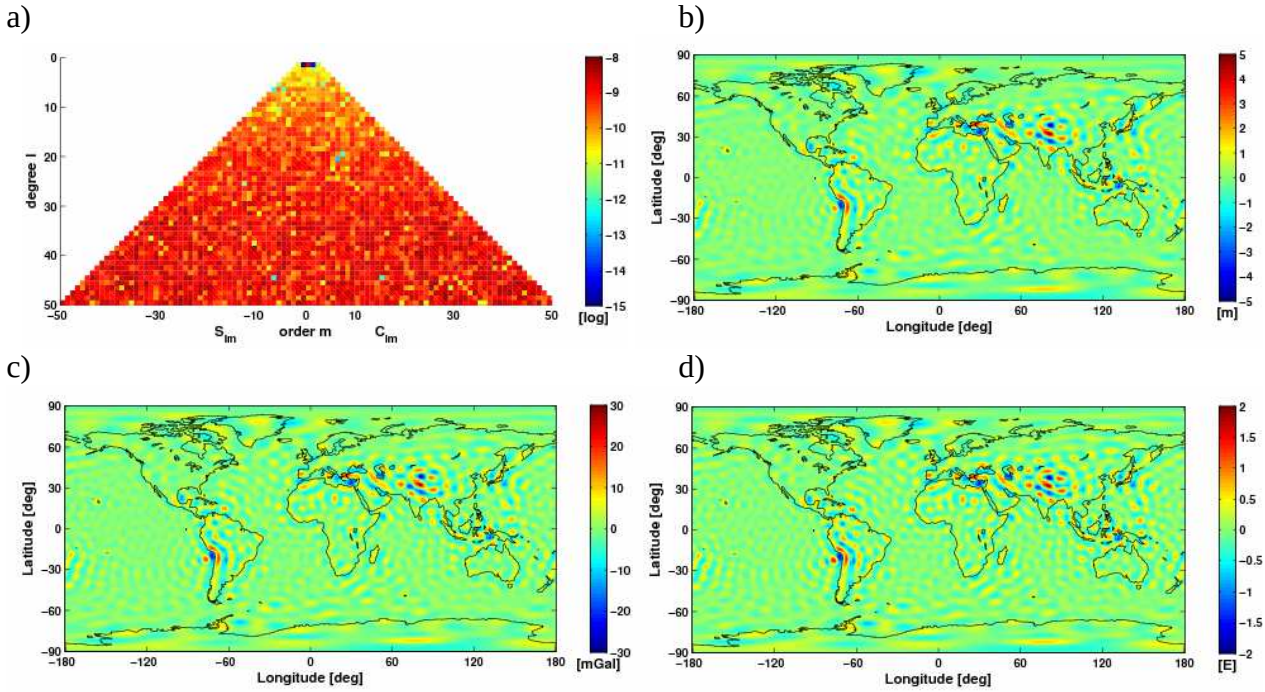

Figure 4.27: Spherical Butterworth filtering (order 2, V_{xx}) with cut-off degree $l_c=35$ at model level

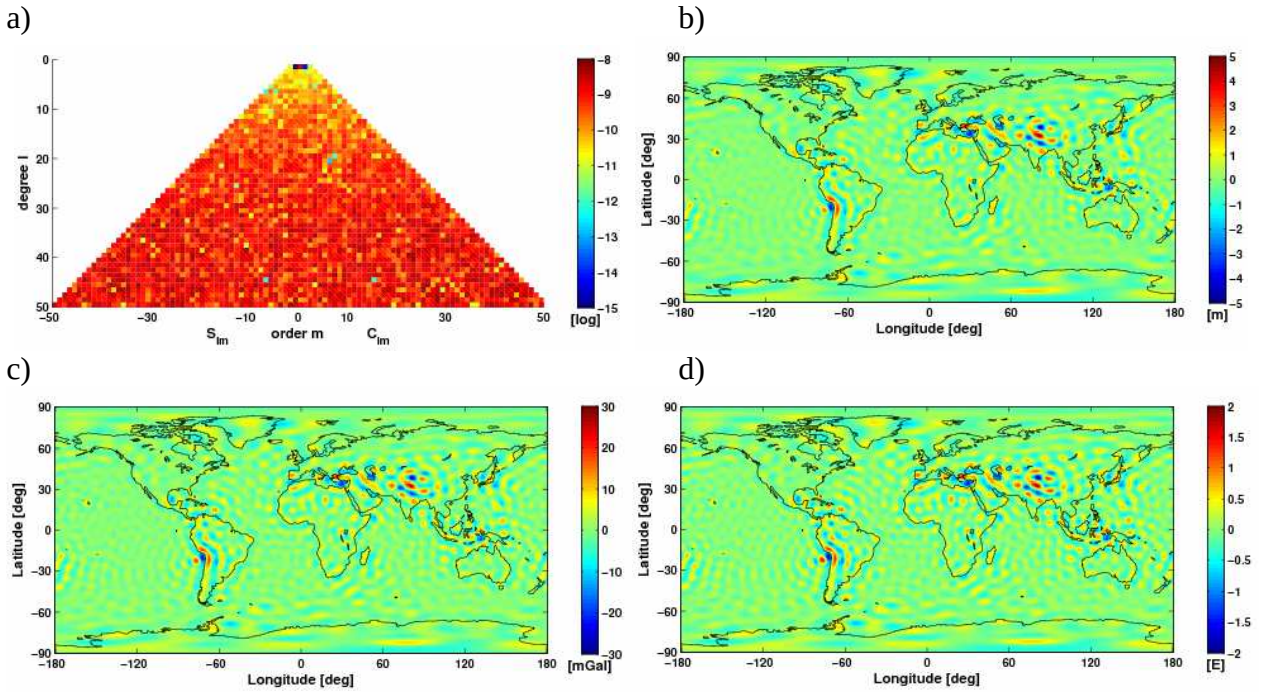

Figure 4.28: Spherical Butterworth filtering (order 2, V_{yy}) with cut-off degree $l_c=35$ at model level

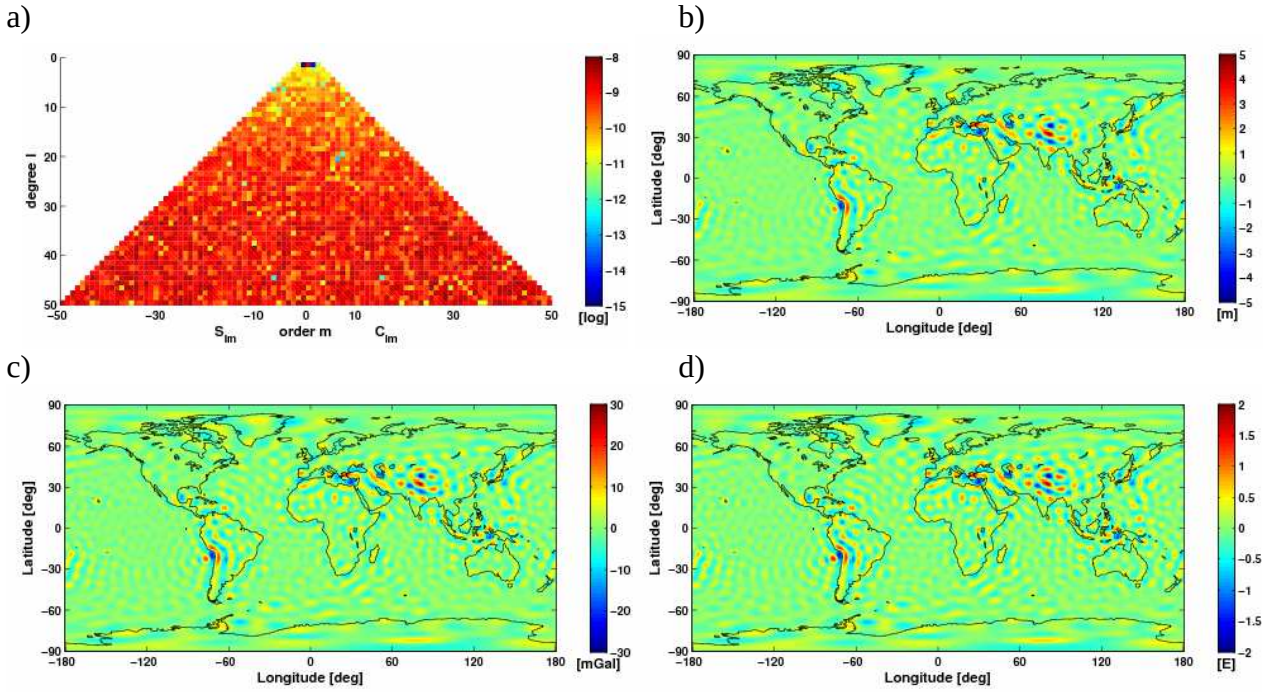

Figure 4.29: Spherical Butterworth filtering (order 2, V_{zz}) with cut-off degree l_c=35 at model level

4.5 Comparison of different filter properties

The discussion of the results from the closed-loop tests, the along-track filtering and the spherical filtering in the previous sections was mainly focused on the investigation of filter influences with respect to different quantities, such as the square root of the PSDs, the SH triangles, geoid heights, gravity anomalies and radial gravity gradients. Furthermore, the different effects caused by applying filters to one of the three signal components were analysed as well as the influences of using a Butterworth instead of a boxcar filter.

This section, however, will investigate how these results are influenced by modifying the filters. These specific modifications include the variation of the cut-off frequencies for along-track filtering (section 4.5.1) and of the cut-off degrees for spherical filtering (section 4.5.2) as well as the variation of the Butterworth filter orders (section 4.5.3).

All three sections will first show the actual filter properties, either in the spectral domain for along-track filters or as SH triangles for spherical filters. Afterwards, the square rooted PSDs of the reference and filtered signals will be shown. Finally, tables will give an overview of the RMS values which are based on the differences between reference and filtered models. Since the results for all three signal components are basically very similar, the following sections will only interpret the results for the radial component V_{zz} because it is the component with the maximum signal power. The interested reader is referred to the appendix which shows the difference plots and statistics for all three signal components and all different filter properties.

4.5.1 VARIATION OF THE CUT-OFF FREQUENCY FOR ALONG-TRACK FILTERING

Figure 4.30 reveals the filter properties in the spectral domain in the form as they will be applied along-track to the simulated signals. The left side shows the boxcar filter design and the right side the Butterworth filter design of order 2.

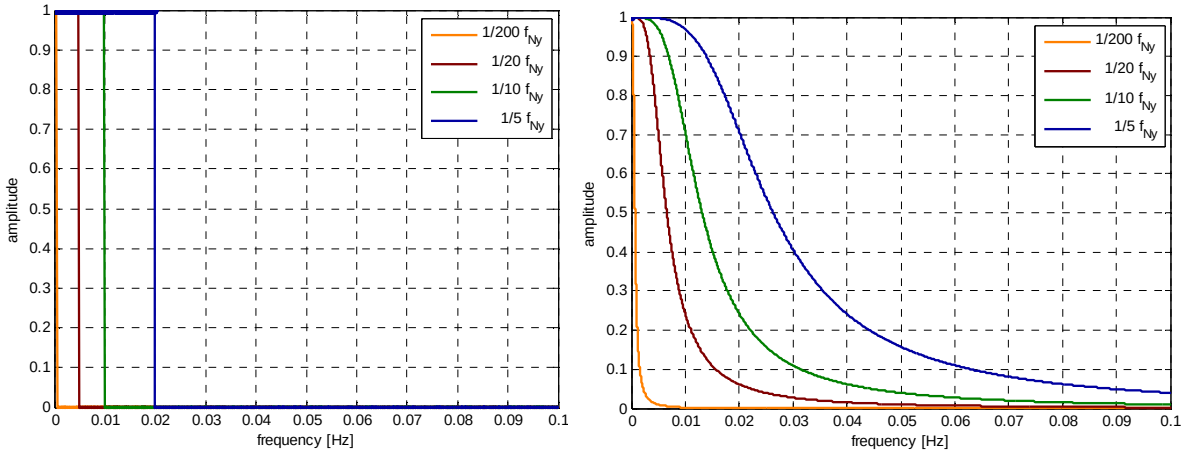

Figure 4.30: Along-track lowpass filter setups in spectral domain with varying cut-off frequencies (left: boxcar, right: Butterworth, order 2)

Four different cut-off frequencies f_c given as fractions of the Nyquist frequency f_{Ny} were chosen for both filters:

- $f_c = 1/200\ f_{Ny} = 0.5$ *mHz*
- $f_c = 1/20\ f_{Ny} = 5.0$ *mHz*
- $f_c = 1/10\ f_{Ny} = 10.0$ *mHz*
- $f_c = 1/5\ f_{Ny} = 20.0$ *mHz*

The smaller the cut-off frequency, the more aggressive is the filter. That means that for high cut-off frequencies such as *20mHz* only high frequencies are dampened by the filter. With decreasing f_c, the filtered signal will contain less and less high frequencies and will become smoother.

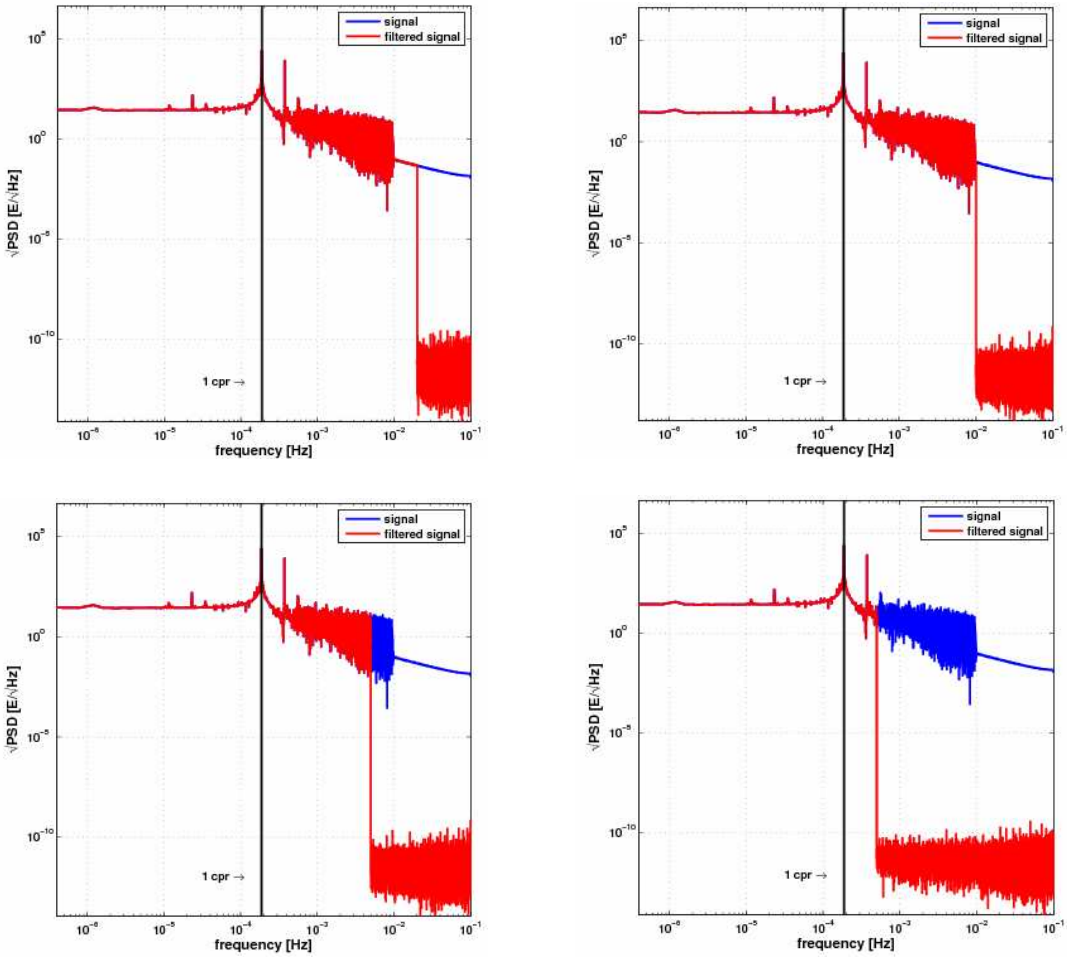

Figure 4.31: √PSD of along-track boxcar filtering of V_{zz} with cut-off frequencies 1/5 (top left), 1/10 (top right), 1/20 (bottom left) and 1/200 (bottom right) of Nyquist frequency at signal level

BOXCAR FILTER Figure 4.31 demonstrates the effects of decreased cut-off frequencies on signal level for along-track boxcar filtering. The square root of the PSDs of reference signal (blue) and filtered signal (red) are compared in each of the four plots on a logarithmic scale. While the √PSD of the reference signal is the same in all four plots, the √PSD of the filtered signal always contains a jump to numerical zero due to the elimination of frequencies higher than the cut-off frequency caused by the boxcar filter.

It should be noted that the boxcar filters at the two cut-off frequencies *10mHz* and *20mHz* are eliminating parts of the signal which contain only little information due to the choice of a EGM96 model with $L_{max} = 50$. Therefore, it is expected that the application of these two filters will not have a major influence on the reference signal.

This fact is proven by the first two rows of the following Table 4.6. The differences between reference and estimated models and their derived quantities respectively are very small. For instance, the difference in geoid heights for a cut-off frequency of *10mHz* is only around $16\mu m$ and even less for *20mHz* with a difference of less than $0.5\mu m$. However, even if these differences are

very small they are still mainly caused by the filters whereas the effects of the closed-loop errors are also inherent in these differences with around $0.08\mu m$ for the radial component.
In contrast, filters with smaller cut-off frequencies such as *0.5mHz* significantly modify the reference signal. This is reflected by an error of almost *4.5m* for the geoid heights, *3.28mGal* for the gravity anomalies and *0.19E* for radial gravity gradients.

Table 4.6: RMS values for along-track boxcar filtering with different cut-off frequencies for V_{zz}

cut-off frequencies	RMS of ΔN [m]	RMS of $\Delta(\Delta g)$ [mGal]	RMS of ΔT_{rr} [E]
1/5 f_{Ny} = 20.0 mHz	$4.931 \cdot 10^{-7}$	$1.492 \cdot 10^{-6}$	$9.420 \cdot 10^{-8}$
1/10 f_{Ny} = 10.0 mHz	$1.636 \cdot 10^{-5}$	$3.276 \cdot 10^{-5}$	$1.648 \cdot 10^{-6}$
1/20 f_{Ny} = 5.0 mHz	0.799	1.963	0.122
1/200 f_{Ny} = 0.5 mHz	4.382	3.283	0.186

BUTTERWORTH FILTER If applying the Butterworth filter (order 2) instead of the boxcar filter, similar conclusions can be drawn. By decreasing the cut-off frequency of a filter, it will have a bigger influence on the reference signal (Table 4.7). That is why the differences between reference and estimated filtered model will also increase for the Butterworth filter. Thus, the Butterworth filter with a cut-off frequency of *20mHz* leads to a minimum difference in geoid height of ca. *1.3cm* as opposed to a filter with a very small cut-off frequency of *0.5mHz* which leads to a significantly higher RMS values in geoid heights of around *1.80m*. The statistics for the gravity anomalies and gravity gradients are also increasing for the application of filters with smaller cut-off frequencies.
Comparing the statistics of Table 4.6 for the boxcar filter and Table 4.7 for the Butterworth filter, it can be recognized that the RMS values for the two higher cut-off frequencies (*10mHz* and *20mHz*) in the first two rows of the tables are higher for the Butterworth than for the boxcar filter and vice versa for the two lower cut-off frequencies (*0.5mHz* and *5mHz*). In general, it is expected that the boxcar filter causes more side effects than the Butterworth filter due to the jump from one to zero at the cut-off frequency which is inherent in the boxcar filter design. This jump is reduced to a smoother transition in the Butterworth filter design (Figure 4.30). However, as it can be also seen in the √PSD plots in Figure 4.32 the Butterworth filter already starts to modify the reference signal for frequencies smaller than the cut-off frequencies. Thus, it is by all means possible that the Butterworth filter has a bigger influence on the signal than the boxcar filter depending on the signal itself and where f_c is chosen. At the same time, a big advantage of the missing jump in the case of the Butterworth filter can be seen in the difference plots in the appendix. The remarkable ringing and ripple structures as well as the features of the transient oscillation effects in the case of applying the boxcar filter (e.g. Figure 6.9) are significantly reduced if the Butterworth filter is used instead (Figure 6.12).

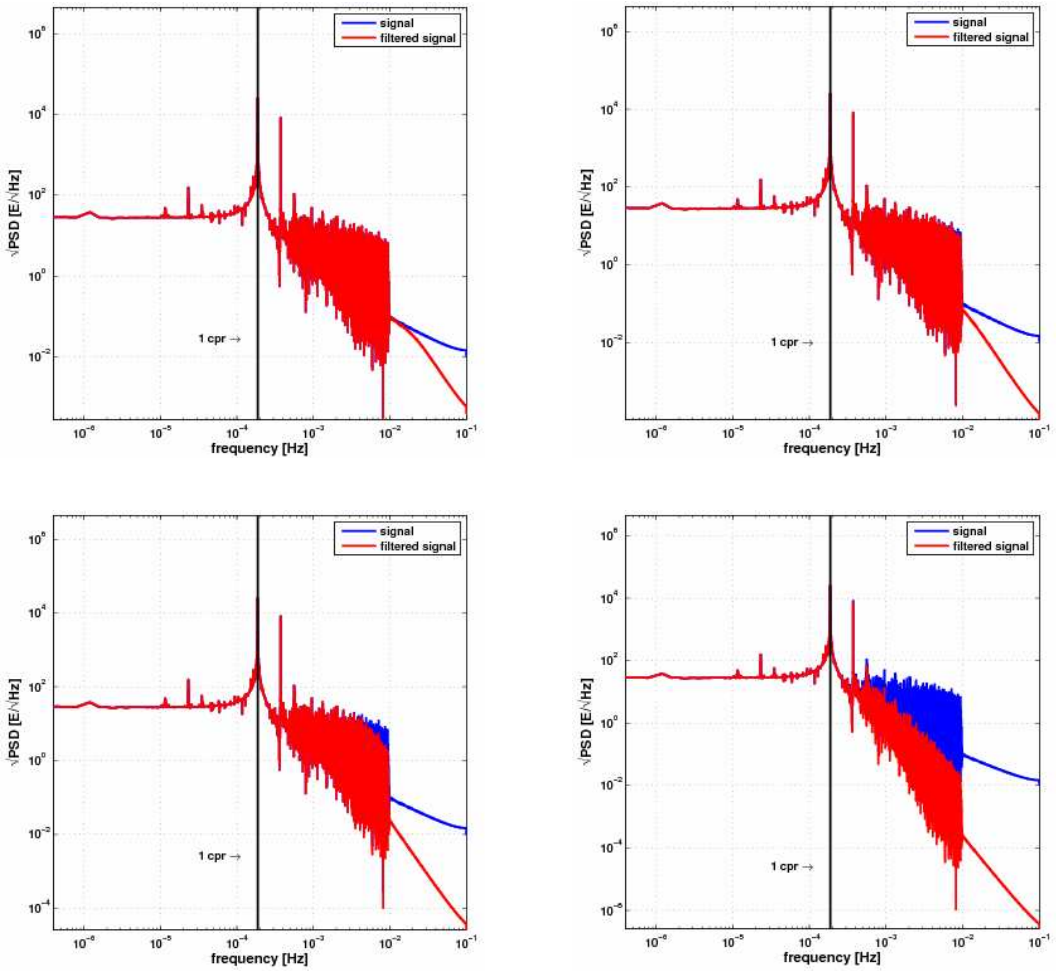

Figure 4.32: √PSD of along-track Butterworth filtering (order 2) of V_{zz} with cut-off frequencies 1/5 (top left), 1/10 (top right), 1/20 (bottom left) and 1/200 (bottom right) of Nyquist frequency at signal level

Table 4.7: RMS values for along-track Butterworth filtering (order 2) with different cut-off frequencies for V_{zz}

cut-off frequencies	RMS of ΔN [m]	RMS of $\Delta(\Delta g)$ [mGal]	RMS of ΔT_{rr} [E]
1/5 f_{Ny} = 20.0 mHz	0.013	0.017	$1.066 \cdot 10^{-3}$
1/10 f_{Ny} = 10.0 mHz	0.144	0.206	0.013
1/20 f_{Ny} = 5.0 mHz	0.438	1.011	0.066
1/200 f_{Ny} = 0.5 mHz	1.790	2.627	0.165

At this point, it has to be emphasized that the computations leading to the results in the last row in Table 4.7 for a Butterworth filter of cut-off frequency *0.5mHz* are based on the disturbing potential instead of the full global potential. In order to understand this step, the next paragraph will give a short expansion of the mathematical background given in section 2.1.
The full global gravity potential *W* is the sum of the gravitational potential *V* and the centrifugal potential *Z* (see Eq. (2.1)). It can be split into an ellipsoidal model part, i.e., the normal potential *U* and the disturbing potential *T*:

$$W = U + T \tag{4.1}$$

The normal potential *U* can be simplified to an SH series which only depends on the first zonal SH coefficients $\bar{c}_{\ell,0}$ with the even degrees $\ell = 0,2,4,6,8$:

$$U(r,\theta) = \frac{GM}{R}\sum_{\ell=0,[2]}^{8}\left(\frac{R}{r}\right)^{\ell+1}\sum_{m=0}^{\ell}\bar{P}_{\ell}(\cos\theta)\bar{c}_{\ell,0} \tag{4.2}$$

where θ is the co-latitude of the satellite and $r = R+h$ with the satellite altitude *h*. *GM* is the gravitational constant (*G*) times mass (*M*) of the Earth with its mean radius *R*. $\bar{P}_{\ell}(\cos\theta)$ is the normalized Legendre polynomial of degree ℓ.
The normalized zonal SH coefficients with the even degrees $\ell = 0,2,4,6,8$ are computed as follows:

$$\bar{c}_{\ell,0} = -\frac{J_{\ell}}{\sqrt{2\ell+1}} \tag{4.3}$$

where J_{ℓ} are the GRS80 physical constants (Rummel, 1992).

As the disturbing potential represents the difference between any gravity related observation and the corresponding quantity derived from the normal gravity field, it can be computed by subtracting the normal potential from the gravity potential which leads to the following SH series:

$$T(r,\theta,\lambda) = \frac{GM}{R}\sum_{\ell=0}^{\infty}\left(\frac{R}{r}\right)^{\ell+1}\sum_{m=0}^{\ell}\bar{P}_{\ell m}(\cos\theta)(\Delta\bar{C}_{\ell m}\cos m\lambda + \Delta\bar{S}_{\ell m}\sin m\lambda) \tag{4.4}$$

where $\Delta\bar{C}_{\ell m} = \bar{C}_{\ell m} - \bar{c}_{\ell m}$ and $\Delta\bar{S}_{\ell m} = \bar{S}_{\ell m}$.

The simulated signal generated by a synthesis using the EGM96 global model is composed of the normal potential and the disturbing potential. Oversimplified, it can be stated that the normal potential is mainly responsible for the two peaks of the square rooted PSD spectrum of the signal. These peaks are at around *0.2mHz* and *0.4mHz*. The full gravity potential and the disturbing potential are shown for the radial signal component V_{zz} as square rooted PSD plots in Figure 4.33. The disturbing potential is distributed with a relatively constant oscillation range over almost the

whole spectrum. It seems to be responsible for the oscillation features in the full gravitational potential which appear for frequencies between around *0.4mHz* and *10mHz*.

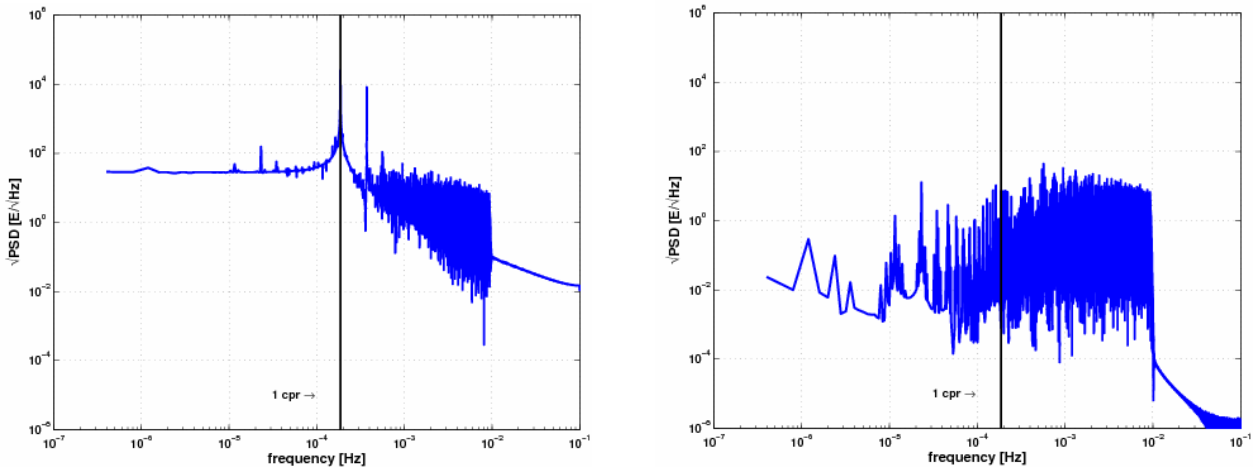

Figure 4.33: √PSD spectra of full gravity potential (left) and of disturbing potential (right) for V_{zz}

All filter operations can be theoretically applied to the disturbing potential instead of to the full gravity potential. If none of the two peaks is significantly diminished by a filter and if we are only interested in the filter effects, it does not make a big difference whether the filter is applied to one or the other. The reason is that when the full potential is used, the normal potential should be fully cancelled out in the end by taking the differences between reference and filtered model in order to show the filter effects and not the effects of the Earth ellipsoidal. Therefore, as soon as one of the peaks is significantly modified by a filter, the disturbing potential should be used instead.
For the application of Butterworth filters, the effects of the Earth ellipsoidal field are always slightly present in the difference plots between reference and filtered dataset and will increase with decreasing cut-off frequencies. The reason is that Butterworth filters are modifying all frequencies in the signal spectrum. As, however, these effects were very small for the cut-off frequencies of *5mHz*, *10mHz* and *20mHz*, all Butterworth and boxcar filters of these higher cut-off frequencies implemented in the study were applied to the full gravity potential.

Filters with the specific cut-off frequency of *0.5mHz* or with even smaller cut-off frequencies have to be handled differently. Since the cut-off frequency of *0.5mHz* is still higher than the frequency of the second peak with *0.4mHz*, this peak is not modified by a boxcar filter. The boxcar filtered models still contain the normal potential which is fully cancelled out in the model difference plots. However, the Butterworth filter with the same cut-off frequency of *0.5mHz* already starts to diminish the spectrum of the signal for frequencies smaller than the cut-off frequency including the second peak at around *0.4mHz*. In other words, parts of the normal potential will be also filtered out. This leads to a filtered model of maximal degree and order 50 with geoid heights reaching from around *-400m* to *+700m*. Thus, the differences between reference and filtered model are even higher than the reference model itself with geoid heights in a range from ca. *-105m* to *+80m*. Therefore, this Butterworth filter has to be applied to the disturbing potential instead of to the full

gravity potential in order to avoid these unacceptable huge features in the difference plots which are caused by filtering the normal potential.

In general, it can be said that decreasing the cut-off frequencies of along-track filters will lead to higher differences between reference and filtered data. The question is if this is also true for the decrease of cut-off degrees if applying spherical filters. This will be discussed in the next section.

4.5.2 VARIATION OF THE CUT-OFF DEGREE FOR SPHERICAL FILTERING

According to the tuning of the cut-off frequencies of along-track filters, the cut-off degrees of spherical filters can be modified as well. The influence on the reference data by applying a filter with cut-off degree $l_c = 35$ has been already discussed in section 4.4. This section 4.5.2 deals with the effects if the cut-off degree is increased to $l_c = 40$. The corresponding spherical filter designs in form of filter factors represented in SH triangles are shown in Figure 4.34 for the boxcar filter and in Figure 4.36 for the Butterworth filter.

Analogue to the case of along-track filtering, it can be stated that the reference data will be more influenced by a spherical filter with lower cut-off degrees. Obviously, more degrees of the original model are cut-off for $l_c = 35$ than for $l_c = 40$ which leads to a loss of information.

BOXCAR FILTER Applying a boxcar filter of cut-off degree l_c to the EGM96 model with maximum degree and order L_{max} = 50 followed by a synthesis to compute the simulated signal is simply the same as generating the synthetic signal from a model of $L_{max} = l_c$ instead of $L_{max} = 50$. That is why in the square rooted PSD plot (Figure 4.35) the end of the oscillations in the reference signal (blue) is just shifted to smaller frequencies for the filtered signal. With decreasing cut-off degrees, the shift will continue in direction to even smaller frequencies. The non-oscillating part of the spherical filtered signal stays coincident with the reference signal in contrast to applying along-track filters which dampen this tail to numerical zero for frequencies higher than the cut-off frequency. Thus, one could assume that applying a spherical boxcar lowpass filter seems to have a similar influence on the reference data as applying an along-track bandstop filter.

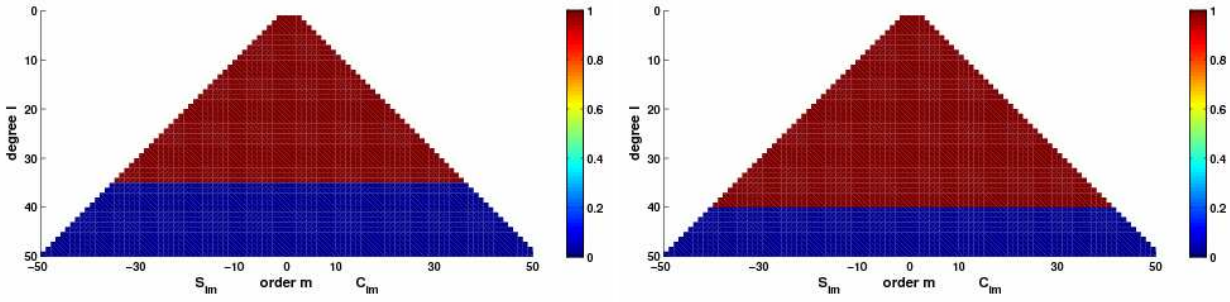

Figure 4.34: Spherical boxcar filter setups with cut-off degrees $l_c=35$ (left) and $l_c=40$ (right)

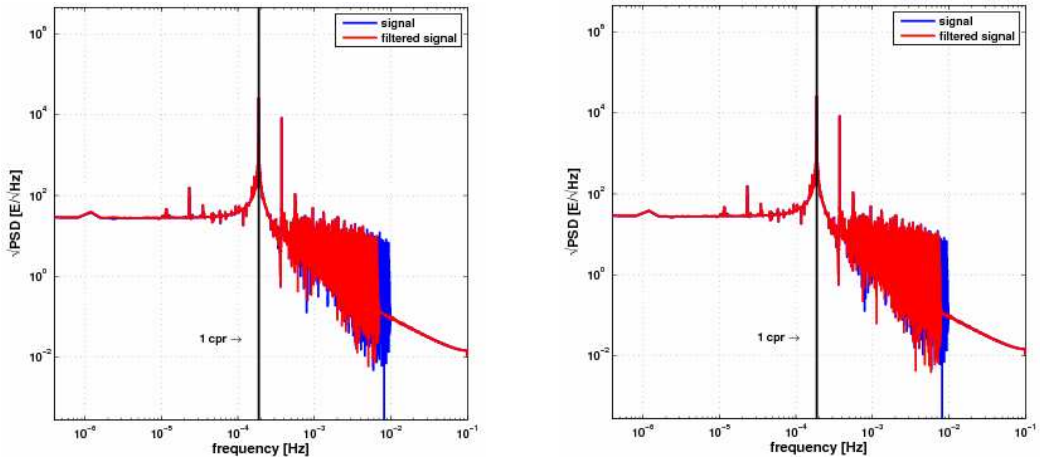

Figure 4.35: √PSD of spherical boxcar filtering of V_{zz} with cut-off degrees $l_c=35$ (left) and $l_c=40$ (right) at signal level

The RMS values in Table 4.8 verify that the differences between reference and filtered models are higher if a boxcar with a lower cut-off degree is chosen. A decrease of the cut-off degree from 40 to 35 yields an increase in the RMS values for the geoid heights from *18.8cm* to *26.4cm*, for the gravity anomalies from *1.27mGal* to *1.68mGal* and for the gravity gradients from *0.10E* to *0.12E*.

Table 4.8: RMS values for spherical boxcar filtering with different cut-off degrees l_c for V_{zz}

cut-off degree	RMS of ΔN [cm]	RMS of $\Delta(\Delta g)$ [mGal]	RMS of ΔT_{rr} [E]
35	26.369	1.676	0.123
40	18.753	1.268	0.098

BUTTERWORTH FILTER The spherical Butterworth filter of order 2 has a considerably smaller influence on the reference dataset than the boxcar filter with the same cut-off degree. This can be validated by the smaller differences revealed in Table 4.9. The RMS values of applying a Butterworth filter with a cut-off degree 35 are *15.4cm* for ΔN, *0.89mGal* for $\Delta(\Delta g)$ and *0.06E* for ΔT_{rr}. They are even smaller than those resulting from the application of a boxcar filter with a higher cut-off degree of 40. By comparing the square rooted PSDs of the reference signal (blue) and the signal (red) filtered by a spherical Butterworth filter of order 2 (see Figure 4.37), it becomes evident that this filter type has a smaller influence. The end of the oscillation is not completely shifted as for the boxcar filter but only slightly dampened in magnitude. The reason is that the transition in the Butterworth filter design (Figure 4.36) is much smoother without jump and that coefficients with a degree higher than the cut-off degree are not completely dampened to zero as it is done for the boxcar filter.

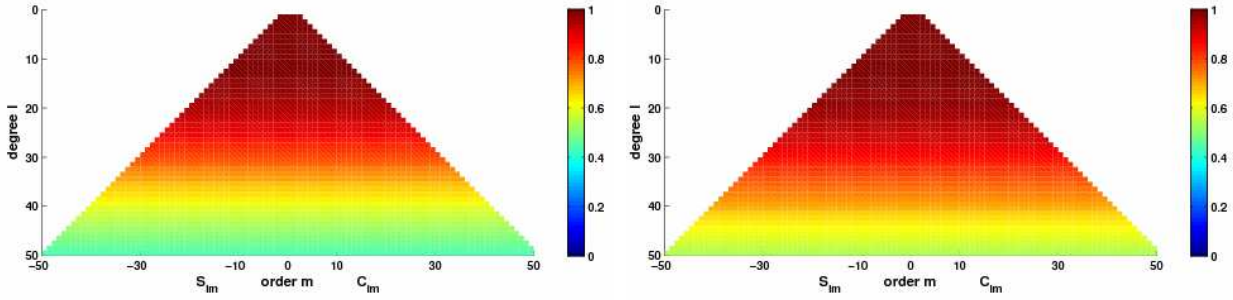

Figure 4.36: Spherical Butterworth (order 2) filter setups with cut-off degrees $l_c=35$ (left) and $l_c=40$ (right)

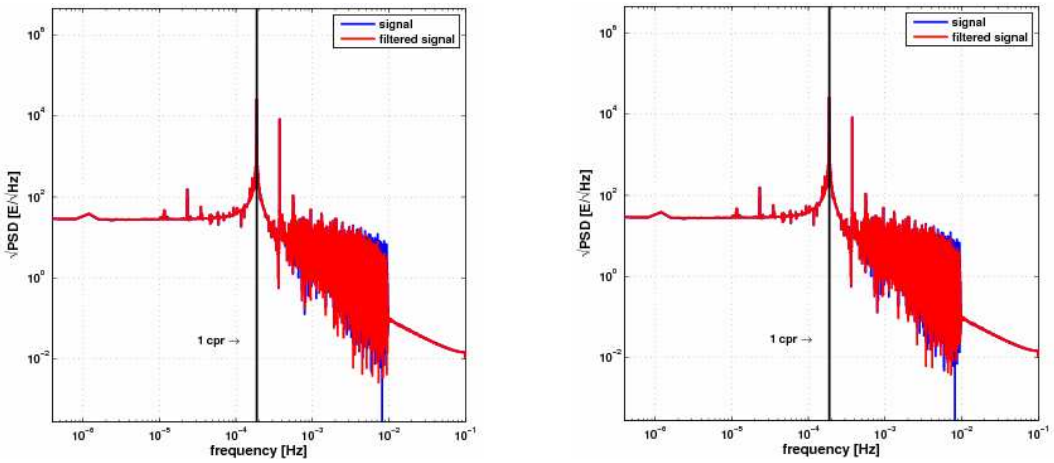

Figure 4.37: √PSD of spherical Butterworth (order 2) filtering of V_{zz} with cut-off degrees $l_c=35$ (left) and $l_c=40$ (right) at signal level

Table 4.9: RMS values for spherical Butterworth filtering (order 2) with different cut-off degrees l_c for V_{zz}

cut-off degree	RMS of ΔN [cm]	RMS of $\Delta(\Delta g)$ [mGal]	RMS of ΔT_{rr} [E]
35	15.436	0.885	0.062
40	11.288	0.663	0.047

4.5.3 VARIATION OF ORDER OF BUTTERWORTH FILTER

Another parameter which can be modified for the along-track as well as spherical filtering is the filter order in the case of a Butterworth filter. The order determines the slope of the transition from maximum to minimum amplitude in the filter design. As visible in Figure 4.38, the slope is becoming steeper with increasing order and is therefore approaching a boxcar filter design.

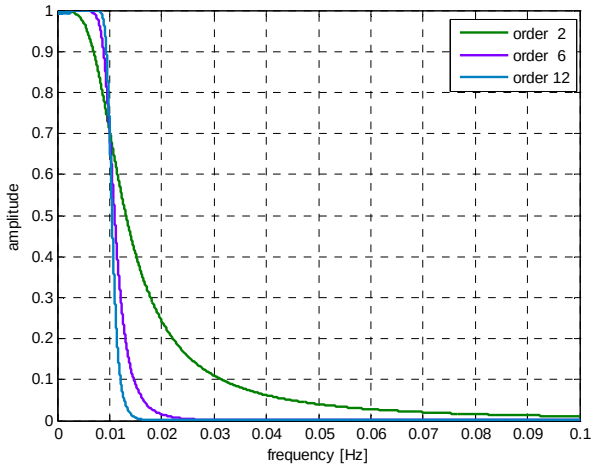

Figure 4.38: Along-track Butterworth filter setups in spectral domain with a cut-off frequency of 1/10 of Nyquist frequency and varying Butterworth filter orders (2, 6, 12)

ALONG-TRACK BUTTERWORTH FILTERING In the square rooted PSD plots in Figure 4.39, it can be seen that Butterworth filters independent of the order but with a cut-off frequency of *10mHz* are mainly attenuating the non-oscillating tail of the reference signal spectrum. Note that the vertical axes of the plots are scaled differently. The spectrum of the signal filtered by a Butterworth filter of order 12 is attenuated to approximately $10^{-12}E/\sqrt{Hz}$ at the Nyquist frequency while the spectrum of the signal filtered by a Butterworth filter of order 6 is only attenuated to ca. $10^{-8}E/\sqrt{Hz}$. Increasing the order of a Butterworth filter, leads to a slightly steeper attenuation. In other words, these filters of higher orders are diminishing the amplitude of the √PSD of the reference signal within a shorter frequency interval which almost appears like a jump similar as in the boxcar filtered spectrum. As a consequence, the RMS values of Butterworth filters with increasing orders are expected to approach the values resulting from applying a boxcar filter with the same cut-off frequency. Since the boxcar filter with a cut-off frequency of *10mHz* yields smaller RMS values than the corresponding Butterworth filter of order 2, it is anticipated that the RMS values for Butterworth filters of increasing orders are decreasing. This assumption can be actually confirmed by the statistics of Table 4.10. The differences are diminished in all three quantities by choosing higher filter orders. The RMS of the geoid heights, for example, is reduced from *14.41 cm* for a filter order of 2 to *5.11cm* for a filter order of 12. The RMS of the corresponding boxcar filtered results is, however, still much smaller with ca. $16\mu m$.

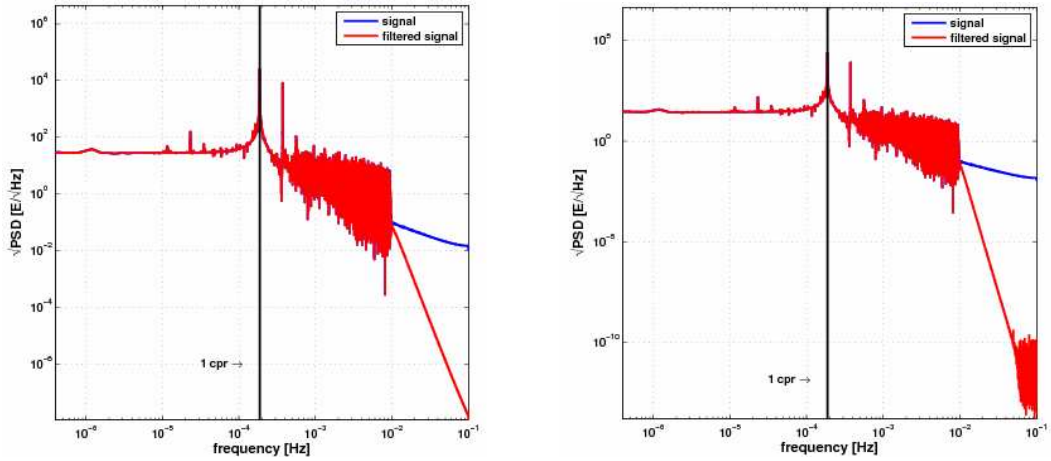

Figure 4.39: √PSD of along-track Butterworth filtering (right: order 6; left: order 12) of V_{zz} with cut-off frequencies 1/10 of Nyquist frequency at signal level

Table 4.10: RMS values for along-track Butterworth filtering with varying orders and with cut-off frequency 1/10 of Nyquist frequency for V_{zz}

Butterworth filter order	RMS of ΔN [cm]	RMS of $\Delta(\Delta g)$ [mGal]	RMS of ΔT_{rr} [mE]
2	14.411	0.206	13.373
6	8.511	0.109	5.035
12	5.114	0.060	2.514

SPHERICAL BUTTERWORTH FILTERING Accordingly, the order of the spherical Butterworth filter can be varied. As a consequence, the filter design of order 12 and cut-off degree 35 looks already very similar to the boxcar filter design. The transition is becoming narrower for a filter order 6 and is limited to a small band around the cut-off degree for filter order 12 as depicted in Figure 4.40.

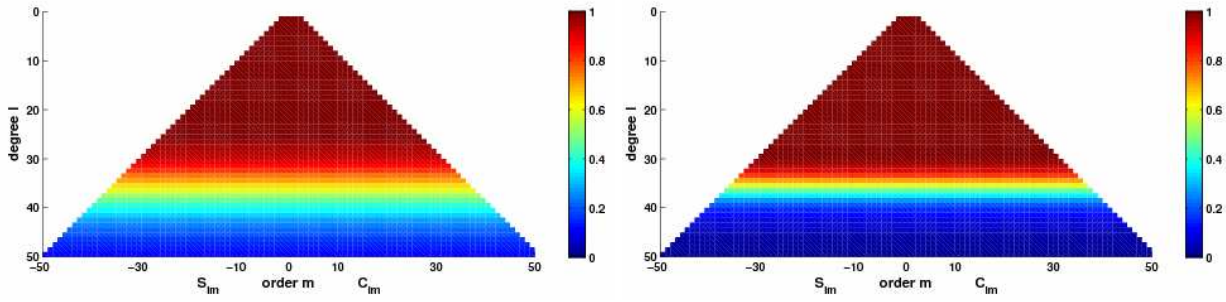

Figure 4.40: Spherical Butterworth filter setups with cut-off degree $l_c=35$ and varying orders (left: order 6, right: order 12)

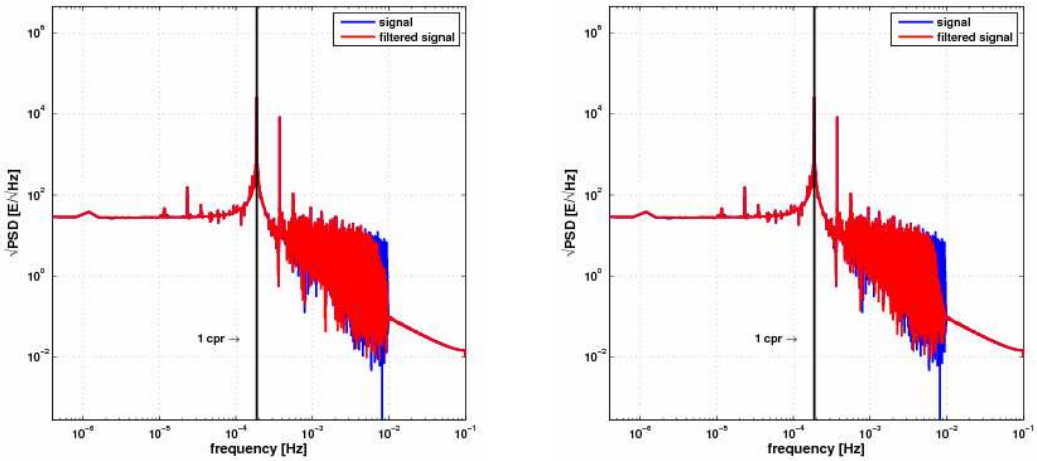

Figure 4.41: √PSD of spherical Butterworth filtering (right: order 6; left: order 12) of V_{zz} with cut-off degree l_c=35 at signal level

Using higher filter orders for spherical Butterworth filters also affects the spectrum of the filtered signal (Figure 4.41). Slightly more √PSD values of the oscillating part of the reference spectrum are reduced if the Butterworth filter of order 12 is applied. This reduced information is reflected in the increasing differences for higher filter orders in Table 4.11. The RMS of the geoid heights is increasing from *15.4cm* for a filter order of 2 to *23.6cm* for a filter order of 12. This trend can also be stated for the gravity anomalies with a rise from *0.89mGal* to *1.51mGal* and for the gravity gradients rising from *0.06E* to *0.11E*. In this case, the Butterworth filter of order 12 leads to RMS values which are only slightly smaller than those of the boxcar filter with *26.4cm* for the geoid heights, *1.68mGal* for the gravity anomalies and *0.12E* for the gravity gradients, respectively.

Table 4.11: RMS values for spherical Butterworth filtering with varying orders and with cut-off degree l_c=35 for V_{zz}

Butterworth filter order	RMS of ΔN [cm]	RMS of $\Delta(\Delta g)$ [mGal]	RMS of ΔT_{rr} [E]
2	15.436	0.885	0.062
6	19.408	1.230	0.091
12	23.643	1.507	0.111

Obviously, the increase of the Butterworth filter order will amplify the high-frequency ringing and ripple structures in the model difference plots on a grid (see Figure 6.36 in appendix) as they have already been discovered for the boxcar filter (Figure 4.25). The reason is that the transition within the Butterworth filter design is becoming steeper for higher filter orders (Figure 4.40) and is approaching the boxcar filter design.

4.6 Empirical transfer functions

Up to now, the influences of applying the along-track as well as spherical filters have been assessed relatively independent of each other. Therefore, this section will try to find a relationship between one-dimensional along-track and two-dimensional spherical filtering. For the sake of this objective, empirical filter transfer functions have to be investigated as explained in section 3.3.4. Even though an explicit analytical relation between these two filter types seems to be far from obvious, these transfer functions make it at least empirically possible to express an along-track filter in the signal domain as a corresponding spherical filter in the model domain and a spherical filter in the model domain as a corresponding along-track filter in the signal domain.

4.6.1 TRANSFER FUNCTIONS IN THE MODEL DOMAIN (ALONG-TRACK FILTERING)

In the case of along-track filtering applied to the simulated GOCE signal along the orbit, it is very interesting to know how a corresponding spherical filter would look like. This can be empirically solved by computing the ratio of along-track filtered and reference model (see Eq. 3.1). This ratio is referred to as empirical transfer function in the model domain. It represents the empirical realization of a spherical filter which has to be applied to the global model in order to achieve the same filter effects as its associated along-track filter applied to the synthetic signal.

The empirical transfer functions have been computed for all different along-track filter properties introduced in section 4.5, i.e., for boxcar as well as Butterworth filters with varying cut-off frequencies and varying filter orders. They are shown in the form of SH triangles in the following figures according to the triangular representation of spherical filter factors. For comparison purposes, it should be carefully noted that some of the plots have differently ranged colorbars and that the values of the transfer functions in the triangles are shown as they are. They are not presented as logarithmic values as it was done for the difference triangular plots above.

Applying along-track filters in the signal domain is realized by multiplying the DFTs of the signal with filter factors lying in a range from one to zero. The spectrum of the signal is modified and some frequencies are attenuated. Thus, it is expected that applying the corresponding transfer function in the model domain to a reference model, will also only attenuate some coefficients but will never amplify them. This would mean that the transfer function also contains values between one and zero. If we take a look at the following figures (Figure 4.42 - Figure 4.46), it is however evident that some values are even higher than one. Filtering one specific frequency of the reference signal does not automatically mean that only one specific coefficient of the reference model will be influenced. It is likely that the along-track filter will affect more than one SH filter coefficient. Some coefficients will be amplified while others will be attenuated. Consequently, some filter factors in the transfer functions are higher than one and others are lower than one.

The following paragraphs will analyse the transfer function plots in the model domain (Figure 4.42- Figure 4.46) which were computed based on different along-track filter properties.

For the transfer functions of the boxcar and Butterworth filters (order 2) and a cut-off frequency of *20mHz* (Figure 4.42), it can be stated that most of the SH filter factors have values which are very close to one. This corresponds to the fact that the signal is not significantly filtered by applying this filter design with a relatively high cut-off frequency of *20mHz*. Since the differences between reference and global models are also very small with geoid height differences at μm level, it can be easily understood why especially the boxcar filter factors are not much deviating from one. If they are applied to the reference global model, in fact, very small differences will be achieved. In the case of the Butterworth filter, significant structures can be seen in the triangles. Most of the sectorial coefficients as well as some other tesseral coefficients running in a parallel tight band are also very close to one. The other tesseral coefficients seem to form semi circles of decreasing values running concentrically to a midpoint at degree 50 and order zero. Thus, the model coefficients of a high degree and a low order will be attenuated mostly. Particularly in the plot for the radial component V_{zz} and also a little bit less for the along-track component, slightly higher values can be recognized for the zonal coefficients. Some are even bigger than one. All in all, the Butterworth filter factors are more diverging from one than the boxcar filter factors.

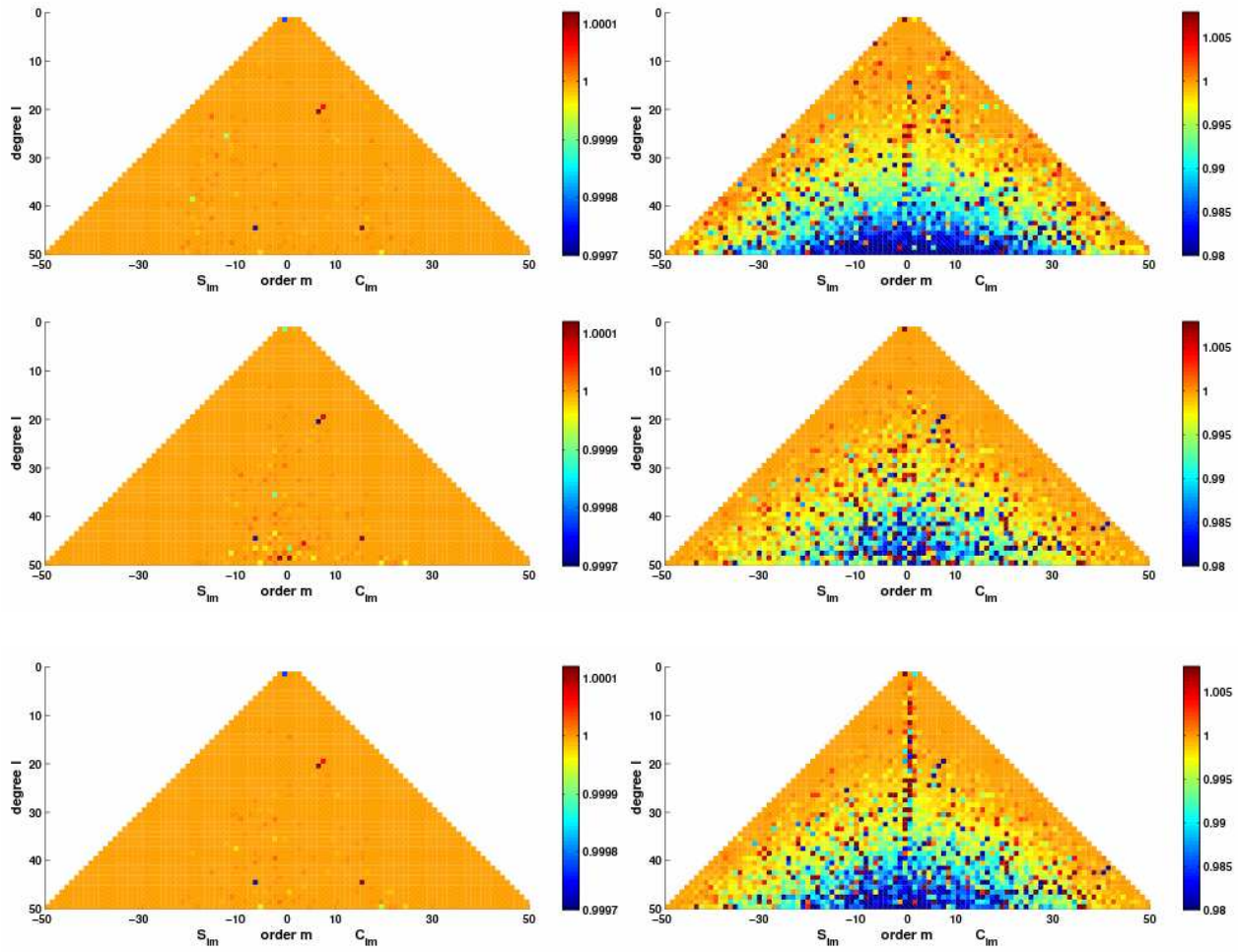

Figure 4.42: Transfer functions in model domain for along-track filtering in signal domain (left: boxcar, right: Butterworth, order 2) with cut-off frequency 1/5 of Nyquist frequency (*20mHz*) for V_{xx}, V_{yy}, V_{zz} (top to bottom)

Decreasing the cut-off frequency to *10mHz* leads to the empirical transfer functions in Figure 4.43. Their structures are very similar to those of the filters with a cut-off frequency of *20mHz*. The only difference for the boxcar filter is that there are now more values which are deviating from one. In the plot for the radial component V_{zz}, one can even assume a structure of higher values for the zonal coefficients. For the Butterworth filter, it can be recognized that the range of deviations is increasing and is still much bigger than the range of deviations for the boxcar filter.

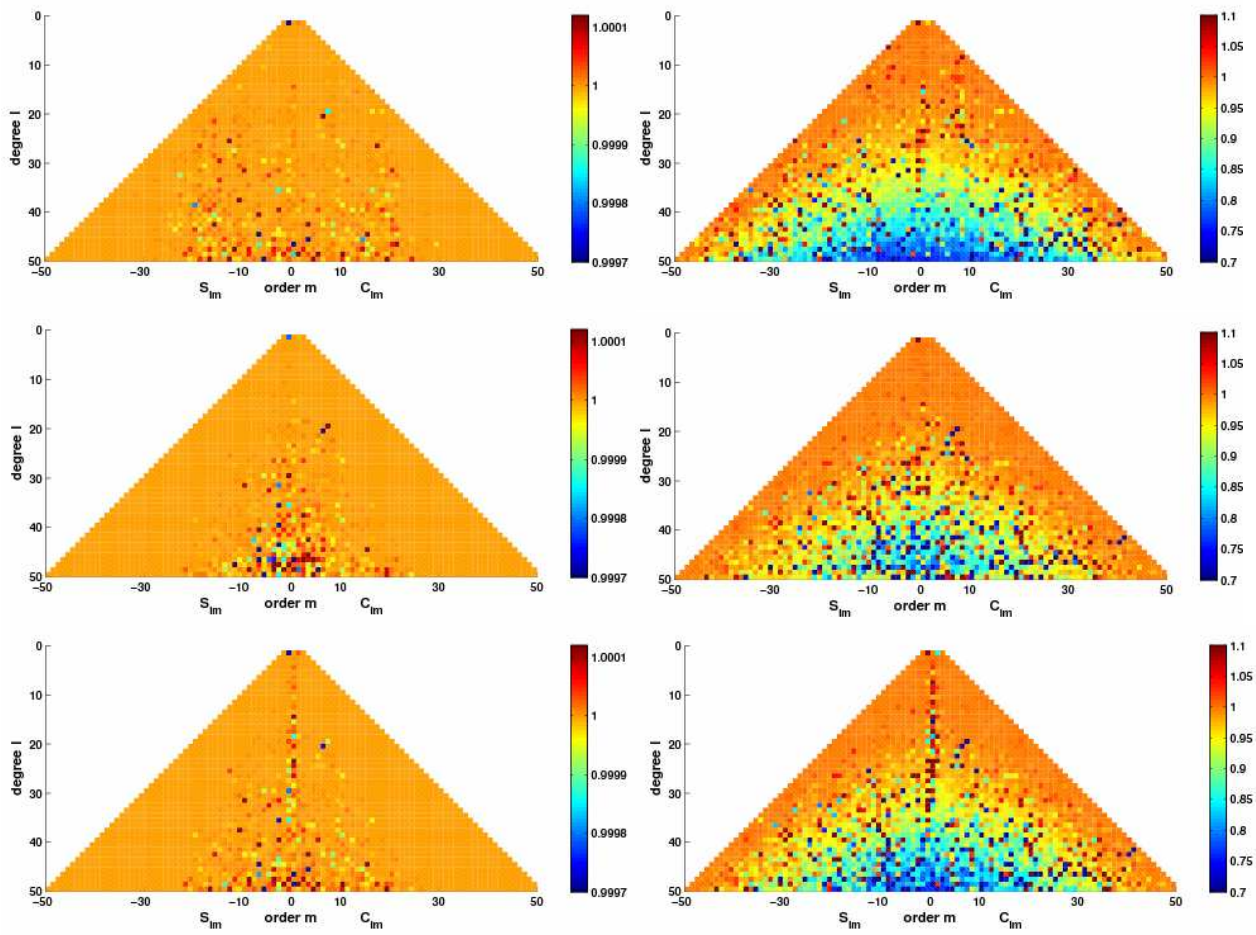

Figure 4.43: Transfer functions in model domain for along-track filtering in signal domain (left: boxcar, right: Butterworth, order 2) with cut-off frequency 1/10 of Nyquist frequency (*10mHz*) for V_{xx}, V_{yy}, V_{zz} (top to bottom)

For a cut-off frequency of *5mHz* (Figure 4.44), this trend of higher deviations for the Butterworth filter than for the boxcar filter is reversed. The maximum values for the boxcar filter are higher than those for the Butterworth filter and its minimum values are smaller, respectively, but the overall structures in the boxcar transfer functions become very similar to the structures in the Butterworth triangles. However, the transition from maximum to minimum values is much smoother for the Butterworth than for the boxcar filter where almost a sharp edge from values close to one to values close to zero can be recognized. This edge follows a semi-circle passing a degree of about 25 for zero order.

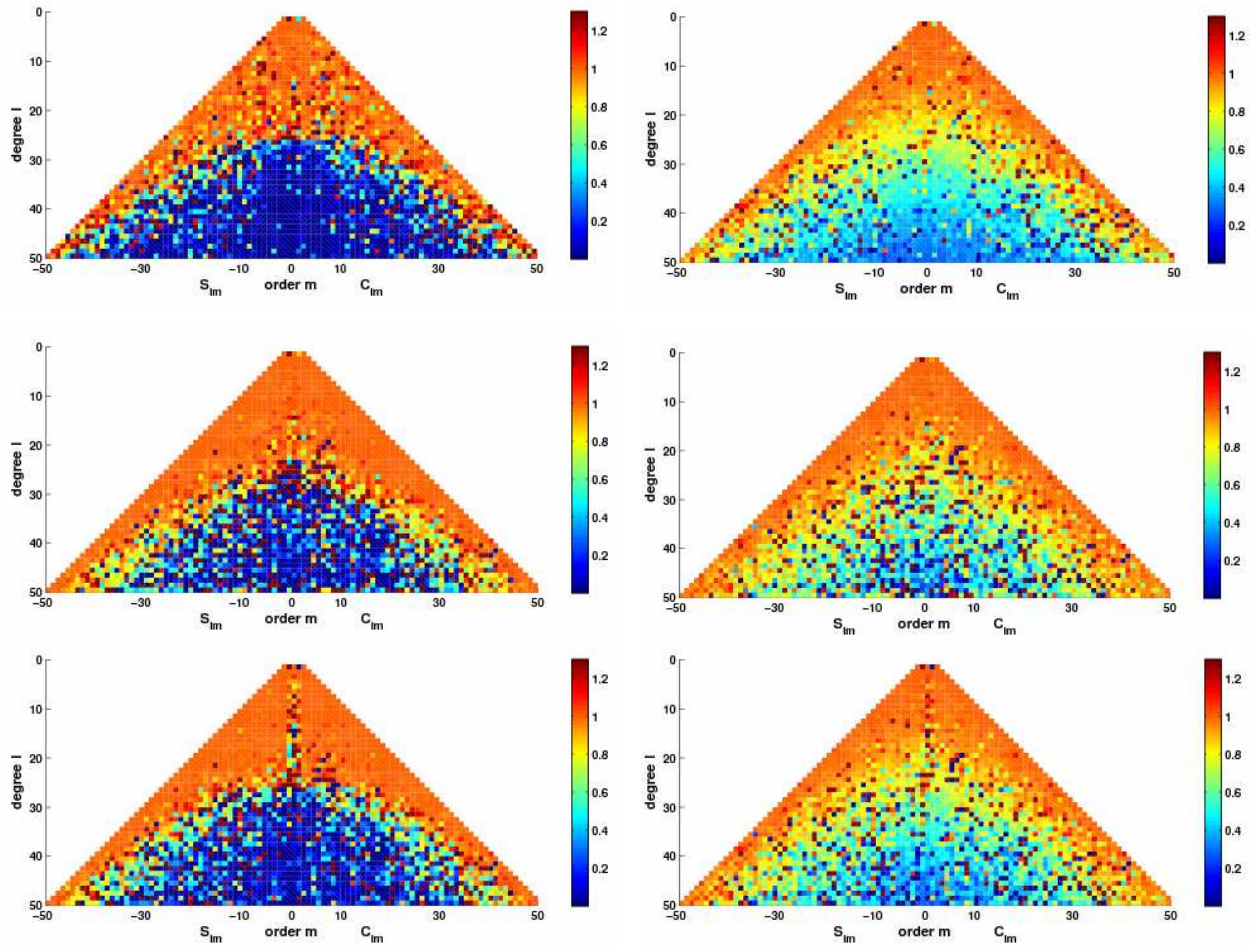

Figure 4.44: Transfer functions in model domain for along-track filtering in signal domain (left: boxcar, right: Butterworth, order 2) with cut-off frequency 1/20 of Nyquist frequency (*5mHz*) for V_{xx}, V_{yy}, V_{zz} (top to bottom)

If the cut-off frequency is further reduced to *0.5mHz*, the corresponding plots of the transfer functions in Figure 4.45 start to look rather random. They are dominated by values close to zero which means that these transfer functions reduce many SH coefficients of the filtered model to zero. This corresponds to a radical along-track filter. For lower degrees, the Butterworth transfer functions contain values that are all in all slightly higher than those of the boxcar filter. This means that the Butterworth filter affects the reference model a little bit less which can be also recognized in the corresponding statistics of the differences between reference and filtered models. If the plots of the different signal components are compared to each other, it can be seen that the values for the along-track component are in general closer to zero than those of the cross-track and radial components. The feature of values higher than one for some zonal coefficients is still vaguely present in the boxcar transfer function for the radial component.

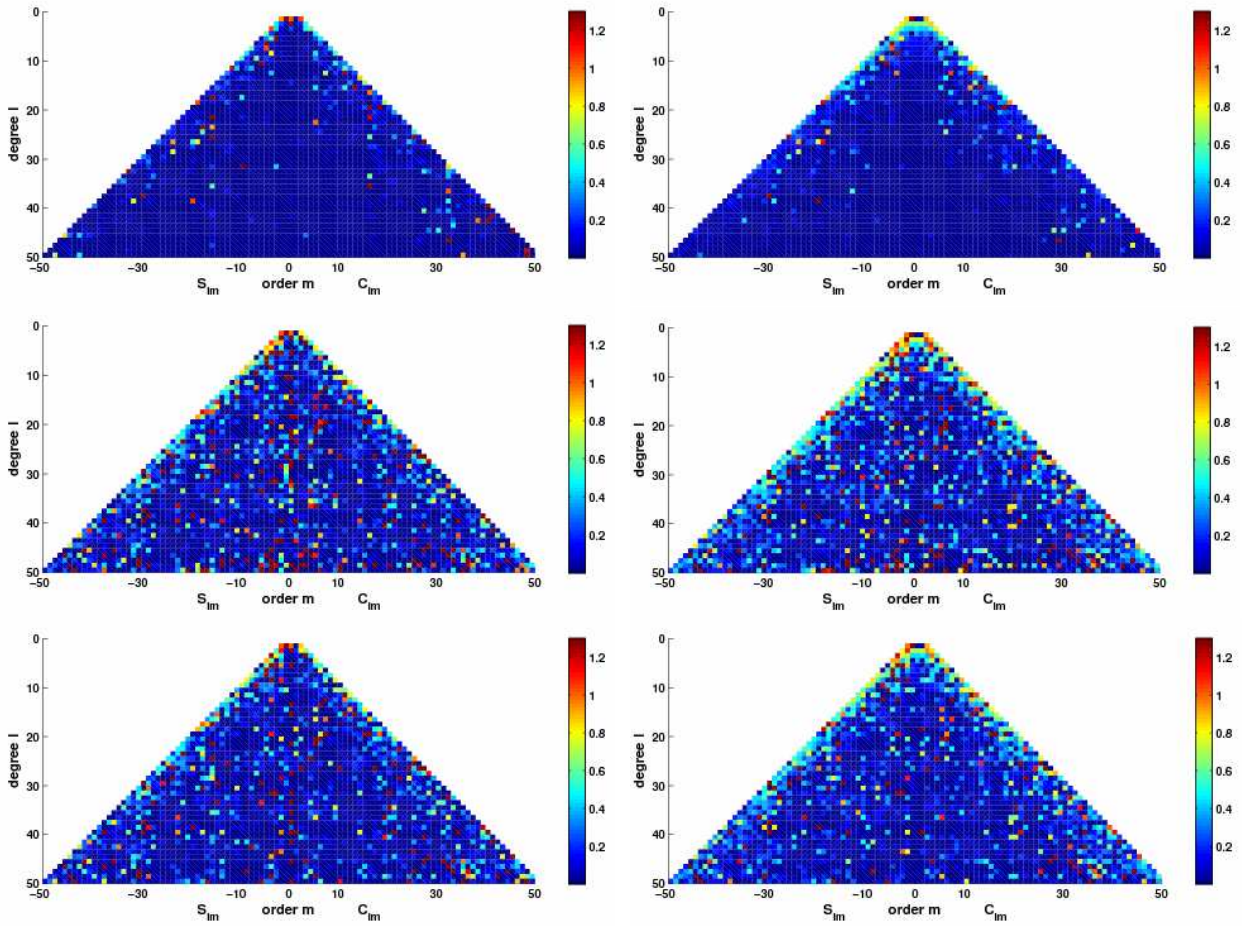

Figure 4.45: Transfer functions in model domain for along-track filtering in signal domain (left: boxcar, right: Butterworth, order 2) with cut-off frequency 1/200 of Nyquist frequency (*0.5mHz*) for V_{xx}, V_{yy}, V_{zz} (top to bottom)

Figure 4.46 shows the transfer functions based on Butterworth filters with filter orders of 6 and 12 and a cut-off frequency of *10mHz*. It can be seen that by increasing the order, more and more coefficients are approaching the value one. The concentric features of decreasing values are limited to just a few values of around zero order and maximum degree of 50 for a filter order of 12. If we compare these plots with the transfer functions of the boxcar filter with the same cut-off frequency in Figure 4.43, it becomes evident that the transfer functions of Butterworth filters with increased order are approaching those ones of the boxcar filter.

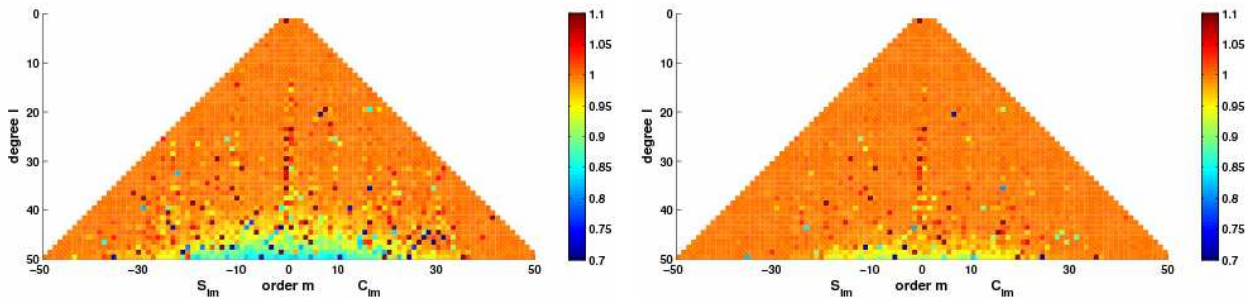

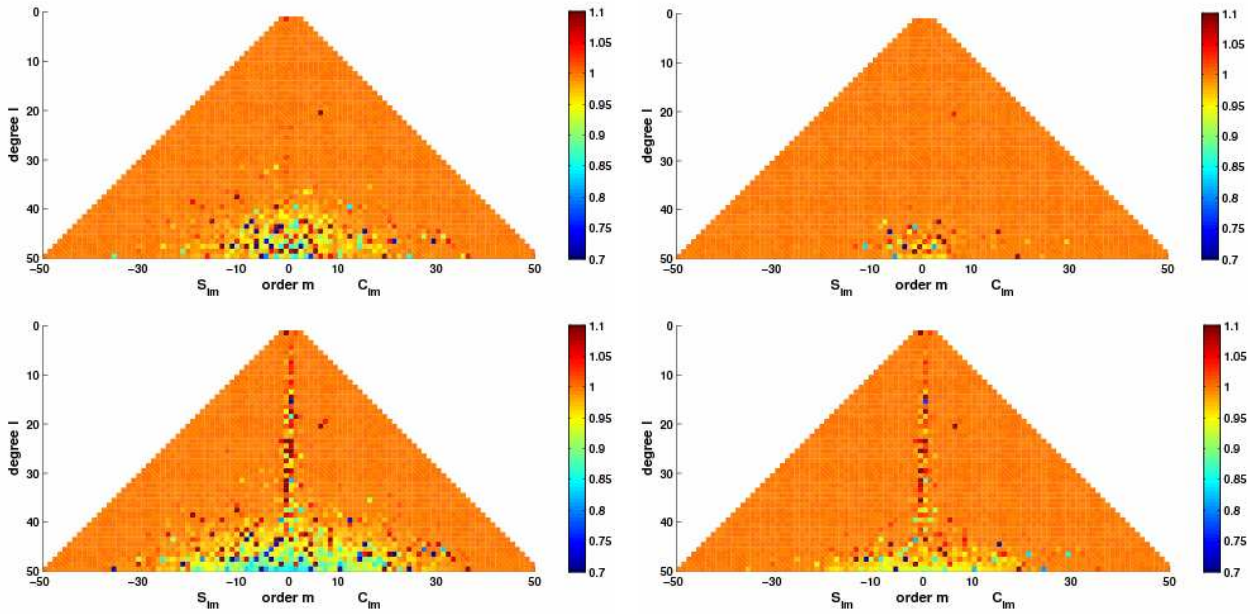

Figure 4.46: Transfer functions in model domain for along-track filtering in signal domain (left: Butterworth, order 6; right: Butterworth, order 12) with cut-off frequency 1/10 of Nyquist frequency (*10mHz*) for V_{xx}, V_{yy}, V_{zz} (top to bottom)

In conclusion, the empirical investigation of the transfer functions in the model domain give information of how a spherical filter needs to be designed in order to achieve the same filter effects as a corresponding along-track filter. However, it becomes also evident that it is very difficult to implement such empirical transfer functions in practice. Alternatively, the only other way is to derive an analytical expression for these transfer functions in order to find an explicit conversion from an along-track filter into a spherical filter.

4.6.2 TRANSFER FUNCTIONS IN THE SIGNAL DOMAIN (SPHERICAL FILTERING)

This section deals with the counterpart of the previous section. It derives an empirical along-track transfer function in the signal domain which is based on the application of a spherical filter to the reference model. By computing the ratio of the √PSD of the spherical filtered signal to the √PSD of the reference signal, the resulting transfer function determines how an along-track filter in the signal domain would have to be designed so that it affects the reference data in the same way as a corresponding spherical filter applied in the model domain.

The along-track transfer functions have been computed empirically for all different spherical filter properties introduced in section 4.5 and are put together in the following figures. These include boxcar as well as Butterworth filters with varying cut-off degrees (Figure 4.47 and Figure 4.48) and increasing orders for the Butterworth filter (Figure 4.49). All plots are presented in the form of amplitudes over frequencies ranging from the fundamental to the Nyquist frequency on a logarithmic scale. Due to better visualization of possible trends, the amplitudes of each transfer

function will be additionally smoothened by a moving average. The original transfer function is shown in blue and the smoothened transfer function in red.

In all plots, oscillating features in the frequency range from *0.1mHz* to *10mHz* are present. The amplitudes before and after these oscillations are situated on a relatively constant line of values close to one. By smoothing the transfer functions, a slightly decreasing trend of the oscillations can be stated in all plots. This corresponds to the attenuation of SH coefficients if applying spherical lowpass filters in the model domain. Consequently, as these transfer functions in the signal domain only significantly modify a limited frequency band, one could assume that applying a spherical lowpass filter in the model domain leads to an along-track bandstop filter in the signal domain. For the signal component V_{xx}, the oscillations are generally starting a little bit later than for the other components but are achieving amplitude maxima in the same range as the other components at around *10mHz*. This is why the trend curve (red) shows a slightly steeper decreasing curve in this frequency region. The oscillating features are achieving amplitudes of almost 10^{-3} to 10^{3} with increasing range for increasing frequencies up to around *10mHz*. Thus, the empirical along-track transfer function in the signal domain contains amplitudes higher than one, although the corresponding spherical filter design only holds values between one and zero. This is similar to the spherical transfer functions with inherent filter factors which are higher than one. The reason for this phenomenon is again that a two-dimensional spherical filter can not be converted into a one-dimensional along-track filter by a simple one to one conversion. That means that modifying one coefficient of the reference model by spherical filtering will not just yield the modification of one specific value in the spectrum of the reference signal. It will rather introduce changes over the whole spectrum.

As the oscillations for the Butterworth filters are smaller than for the boxcar filters, it is assumed that this effect is partly due to the Gibbs' phenomenon. This phenomenon is particularly introduced by the boxcar filter design which contains an abrupt jump from one to zero. Since the transition is smoother for the Butterworth filters, the range of the oscillations will be obviously smaller. As it was expected, the range is increasing with increasing filter orders as the Butterworth filter of higher orders is approaching the features of a boxcar filter (Figure 4.49). Varying the cut-off degree, on the other hand, does not significantly change the overall range of the oscillations, but rather some single amplitudes (compare Figure 4.47 and Figure 4.48).

It should be kept in mind that the application of these empirical transfer functions to the reference signal will cause the same filter effects as the corresponding spherical filters applied to the reference model. In summary, it can be stated that these transfer functions can be derived empirically if the spherical filter influences on the synthetic reference signal are known. However, it seems to be a very difficult task to find a corresponding analytical solution.

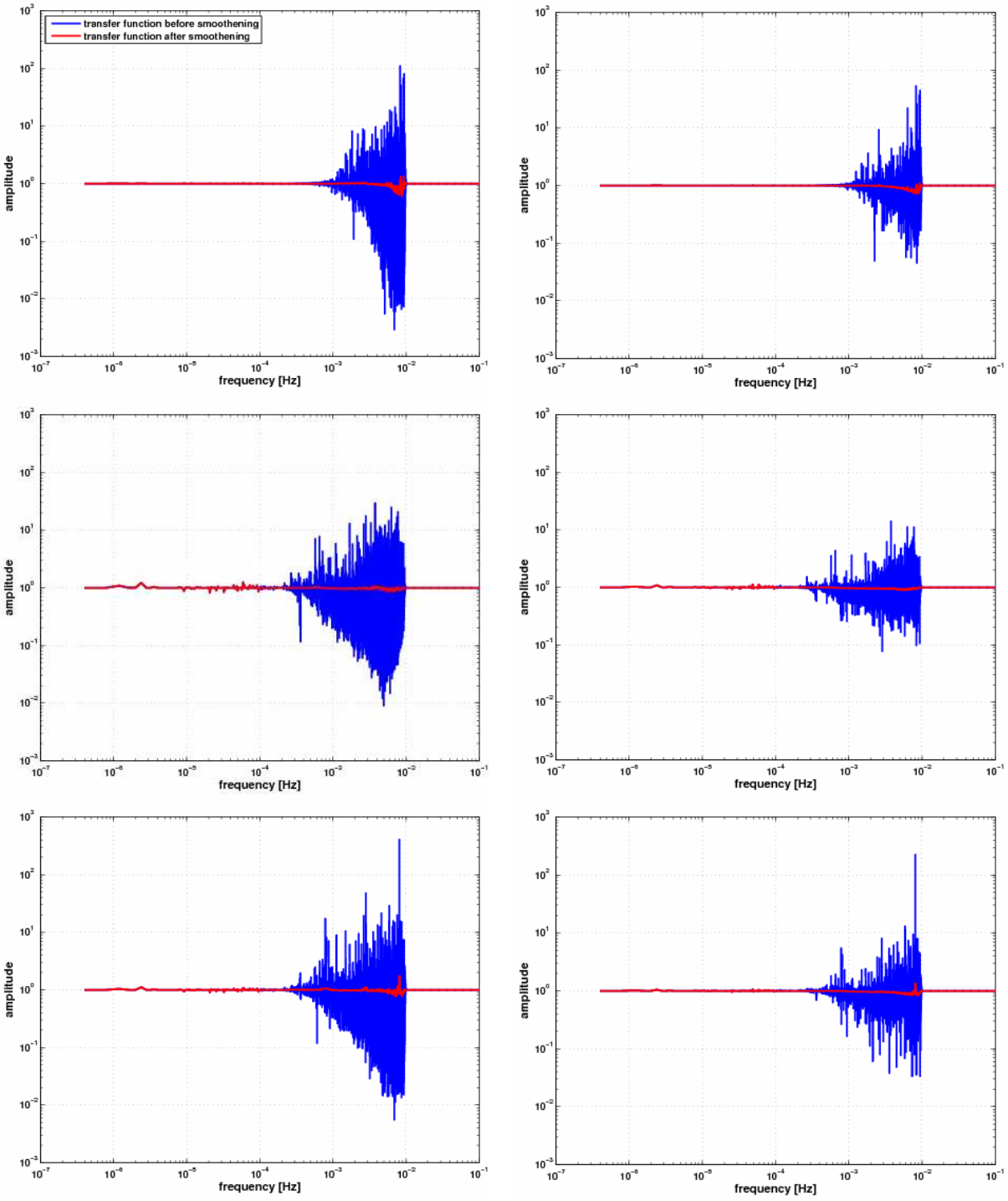

Figure 4.47: Transfer functions in signal domain (blue: before smoothing, red: after smoothing) for spherical filtering in model domain (left: boxcar; right: Butterworth, order 2) with cut-off degree $l_c=35$ for V_{xx}, V_{yy}, V_{zz} (top to bottom)

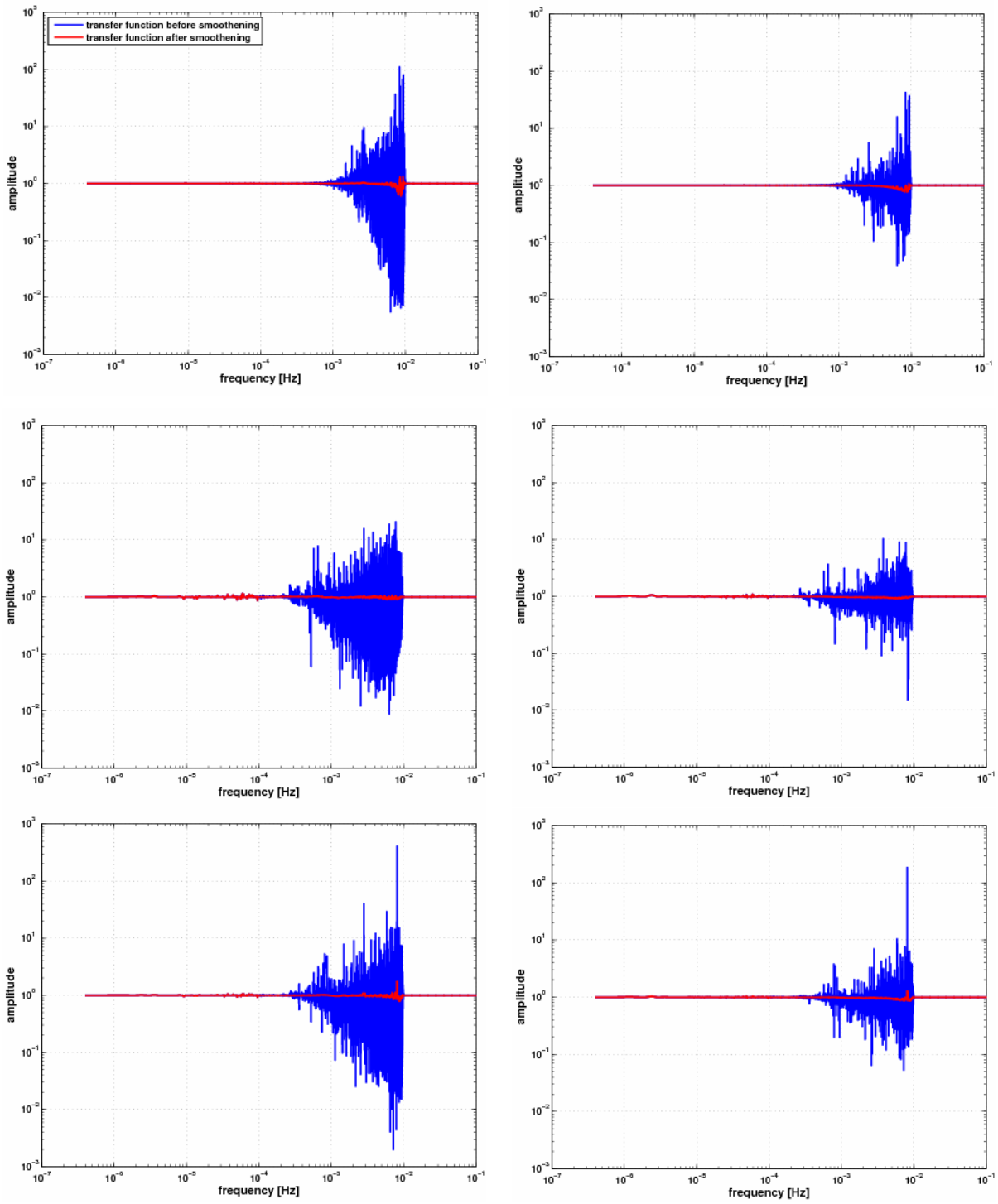

Figure 4.48: Transfer functions in signal domain (blue: before smoothing, red: after smoothing) for spherical filtering in model domain (left: boxcar; right: Butterworth, order 2) with cut-off degree $l_c=40$ for V_{xx}, V_{yy}, V_{zz} (top to bottom)

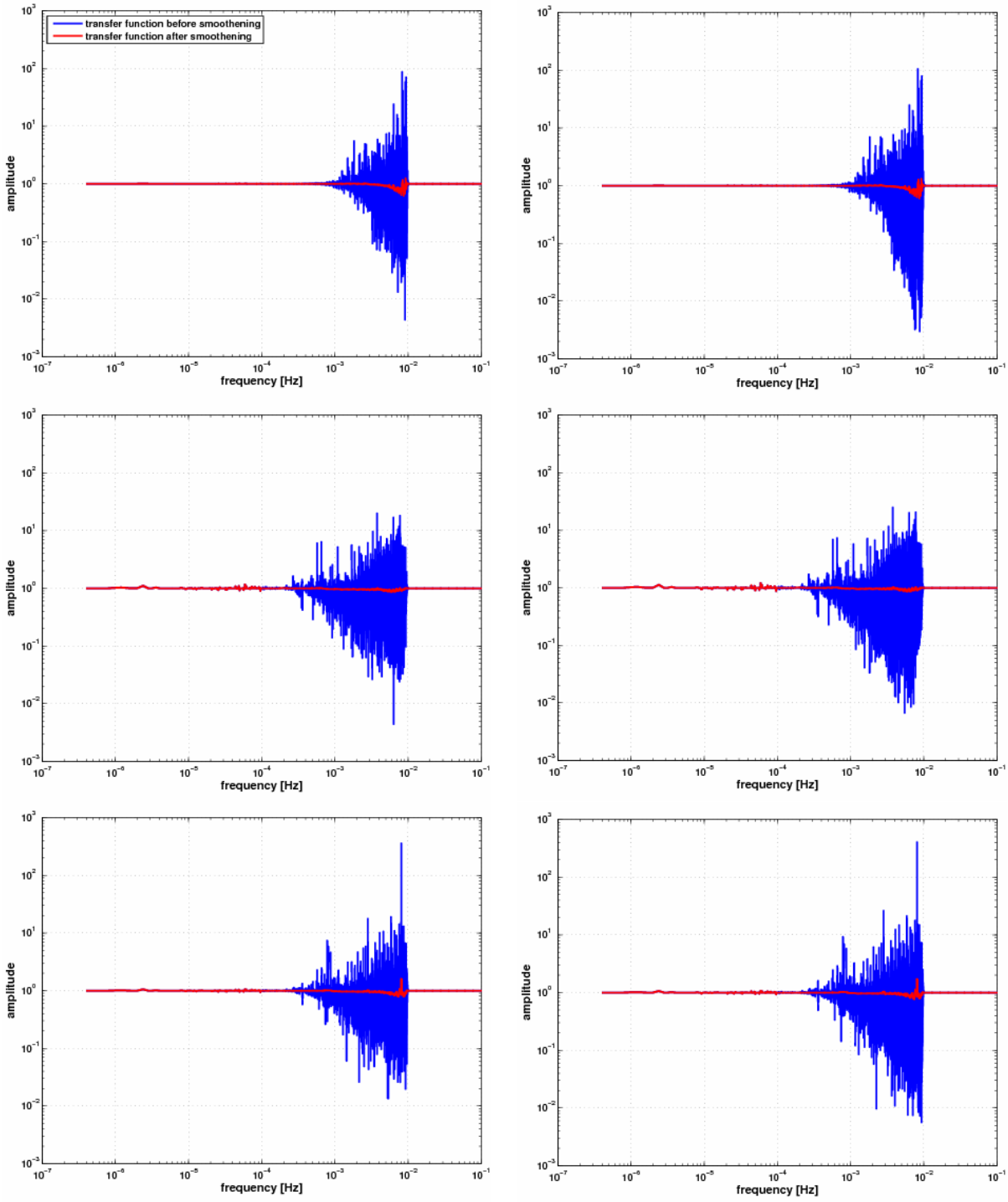

Figure 4.49: Transfer functions in signal domain (blue: before smoothing, red: after smoothing) for spherical filtering in model domain (left: Butterworth, order 6; right: Butterworth, order 12) with cut-off degree $l_c=35$ for V_{xx}, V_{yy}, V_{zz} (top to bottom)

5 CONCLUSIONS AND FUTURE WORK

This final chapter summarizes the main contents and achievements of this study. Additionally, some suggestions for further investigations with respect to the GOCE data processing are provided.

The main objective of this work was to investigate the different influences of one-dimensional along-track and two-dimensional spherical filters on simulated GOCE data. Furthermore, an empirical relation between these two filter types was investigated. All computations were based on the EGM96 reference model and the synthetic reference signal which was generated along a simulated GOCE orbit.

CLOSED-LOOP TESTS In order to prove the consistency and correctness of the software used and the dataset, closed-loop tests were implemented. They indicate that the differences between the reference EGM96 and the estimated model are within the numerical accuracy of the computer. This is true no matter which signal component (V_{all}, V_{xx}, V_{yy} or V_{zz}) is used for the analysis step.
For the cross-track component, the RMS values of the differences are slightly higher than for the other signal components. Even in this case, however, the closed-loop error still lies below the noise-level of GOCE and can just be recognized in the noise-free scenario within these testing procedures. Consequently, the software packages *'create'* and *'adjust'* as well as the implied dataset can be deemed to be an appropriate basis for the further application of filters. It should be kept in mind that all resulting differences between unfiltered and filtered data contain filter effects as well as closed-loop errors whereas the latter are negligibly small.
One interesting outcome of these tests is that using the along-track component in a noise-free scenario leads to more accurate models than using a combined solution with all signal components. It is likely that this effect is caused by the polar gaps which could be probably reduced by using weighting for different signal components within the analysis step. This outcome needs further investigation and could be part of a future work based on the presented closed-loop results

ALONG-TRACK FILTERING The purpose of the one-dimensional along-track filtering tests was to modify the synthetic satellite signal by applying one-dimensional along-track filters to each of the three main signal components. First, the effects of a boxcar and a Butterworth filter (order 2) with a cut-off frequency of one tenth of the Nyquist frequency were investigated. The conclusions of a comparison between various filter properties will be presented later on.
Applying along-track filters introduces transient oscillation or so-called warm up effects which can be reduced by cutting-off the filtered signal at the beginning and at the end. The transient effect is even stronger for the boxcar than for the Butterworth filter and can not be totally eliminated by shortening the signal. This introduces an additional error source for the analysis.
As the radial component of the signal has the highest power, the signal itself and its estimated model are more influenced than the other components by applying an along-track filter. This leads to higher RMS values if taking the difference between the original EGM96 and the estimated filtered model.
Thus, the variations in the features of relative geoid heights, gravity anomalies and gravity gradients between the three different signal components are mainly caused by the transient filter effects and by the different power levels of the components. It should be noted that this is especially the case for cut-off frequencies higher than 1/10 of the Nyquist frequency.
It is evident that the Butterworth filter design of low order is much smoother than the boxcar filter design. It does not contain such a jump in contrast to the boxcar filter. That is why the triangle

plots of the Butterworth filtered SH coefficients present a much more homogenous surface than those of the boxcar filtered SH coefficients. Therefore, it is expected that the application of the boxcar filter has a bigger influence on the reference data than the Butterworth filter. However, it should be kept in mind that the Butterworth filter manipulates already frequencies smaller than the cut-off frequency. Thus, depending on the power of the signal in the modified frequency band that can have the consequence that the Butterworth filter is more aggressive than the boxcar filter. This is indubitably the case for this specific cut-off frequency of 1/10 of the Nyquist frequency.

SPHERICAL FILTERING The two-dimensional spherical filtering of the EGM96 model was implemented by designing a spherical boxcar filter and a spherical Butterworth filter of order 2 with a cut-off degree of 35. Applying these spherical filters leads to major differences between reference and filtered data which do not significantly change if one or the other signal component is used. The reason for this behaviour is that the slightly varying spectra of the signal components do not play a role as the filter is not applied directly to the signal but to the SH coefficients. This is also the reason why filtering SH coefficients does not suffer from transient oscillation effects. Thus, visible features in the geoid heights, gravity anomalies and radial gradients based on taking the difference between EGM96 and estimated filtered model, are all directly coming from applying a spherical filter to the SH coefficients.
In the same way as it was already recognized for the along-track filters, it is obvious that the Butterworth filter is much smoother than the boxcar filter but also manipulates the coefficients already for smaller degrees. Since the Butterworth filter, however, is applied to the relative homogenous SH coefficients and not directly to a varying signal spectrum, its influence is much smaller than the one of the boxcar filter. Consequently and in the case of spherical filtering, the boxcar filter is always more aggressive than the Butterworth filter.
An aggressive boxcar filter with a cut-off degree of 35 can cause geoid height differences of almost *26.5 cm*.

COMPARISON OF DIFFERENT FILTER PROPERTIES In order to get a better general view, further filter properties with varying cut-off frequencies (*$1/5 f_{Ny}$ = 20mHz*, *$1/10 f_{Ny}$ = 10mHz* *$1/20 f_{Ny}$ = 5mHz* and *$1/200 f_{Ny}$ = 0.5mHz*) in the case of along-track filtering and cut-off degree of 40 in the case of spherical filtering were analysed. Additionally, the orders of the Butterworth filters were changed from 2 to 6 and 12. The filters with the relatively high cut-off frequencies of *10mHz* and *20mHz* have a minor influence on the reference data as they filter parts of the signal spectrum which only contain little information.
With decreasing cut-off frequencies, the filters get more aggressive. This means that the filtered signal will contain less and less high frequencies and will therefore become smoother which leads to higher differences between reference and filtered data. These differences reach a maximum of about *4.4m* in geoid heights for the boxcar filter with a cut-off frequency of *0.5mHz.*
For the two lower cut-off frequencies (*5mHz* and *0.5mHz*), the boxcar filters leads to higher differences than the Butterworth filter but vice versa for the higher cut-off frequencies (*10mHz* and *20mHz*). The reason is that the Butterworth filter design does not contain such an abrupt jump between the maximum and minimum amplitude, but rather a smoother transition. However, the Butterworth filter modifies all frequencies in some way. Thus, depending on the signal spectrum, it can actually happen that the Butterworth filter starts to filter parts of the signal which contain more information than the parts which are attenuated by a corresponding boxcar filter. It also has to be mentioned that this aggressive edge in the boxcar filter design leads to the so-called Gibbs'

phenomenon. This effect causes features of ringing and ripples in the geoid heights, gravity anomalies and gravity gradients which are partly reduced by applying a Butterworth filter instead. Varying the cut-off degree in the case of spherical filtering leads to similar conclusions as varying the cut-off frequency in the case of along-track filtering. If the cut-off degree is decreased, the filter has a higher influence on the reference data and therefore yields increasing differences for geoid heights, gravity anomalies and gravity gradients. Furthermore, the spherical Butterworth filter of order 2 has a considerably smaller influence on the reference dataset than the boxcar filter with the same cut-off degree. The reason is that the transition in the Butterworth filter design is much smoother without inherent jump and that none of the coefficients is completely attenuated as it is the case in the boxcar filter design.
In general, it can be said that the increase of the filter orders in the Butterworth filter design, will approach the boxcar filter design. That is why Butterworth filters of high orders affect the reference data in a similar way as a boxcar filter.
Moreover, filtering the GOCE dataset, either by applying along-track or spherical filters, can lead to differences which can not be neglected and are far above the noise-level.

EMPIRICAL TRANSFER FUNCTIONS Finally, an empirical relation between along-track and spherical filters was investigated. For this purpose, transfer functions of the filters have been derived as the ratio between reference and filtered model. They represent spherical filters in the model domain which correspond to one-dimensional along-track filters in the signal domain. On the other hand, computing the ratio between reference and filtered signal estimated from the spherical filtered reference model converts the two-dimensional filters from the model domain into one-dimensional along-track filters in the signal domain. The spherical transfer functions presented as filter factors in the form of coefficient triangles show rather random structures. Modifying one specific frequency of the signal spectrum by applying an along-track filter does not automatically mean that only one specific coefficient of the transfer function in the model domain will be affected. It is evident that the along-track filter effect will be mapped into more than one value of the transfer function which even leads in some cases to values larger than one. Other coefficients in the model domain are reduced. That makes it very difficult to find an explicit relation between the derived spherical transfer function and the corresponding along-track filter design.
In a second attempt, along-track transfer functions are derived empirically in the signal domain. They are representing an along-track filter design which has to be applied to the reference signal in order to achieve similar filter effects as its corresponding spherical filter applied to the reference model. Apart from some random oscillating structures, there are again no obvious features visible in these transfer functions. In general, it is possible to find an empirical way of expressing spherical filters in the form of transfer functions in the signal domain. However, there cannot be made any assumptions about an explicit analytical relation between these along-track transfer functions and a corresponding spherical filter.

In conclusion, this study assessed the influences of various one-dimensional along-track and two-dimensional spherical filter properties on a time-series of synthetic gradiometer data as well as on the corresponding spherical harmonic spectrum. Empirical transfer functions were established in order to find a link between both filter types.
The derivation of a direct relation in an analytical way is theoretically possible and could be part of a future work based on the presented results. One way to try to solve this objective could be for example the application of inclination functions and torus approaches. Other topics which need

further investigation with respect to the results of this study and the processing of GOCE data are, for example, the implementation of along-track and spherical testing procedures for real scenarios including noise and for scenarios following HPF processing chains. Additionally, it is also possible to apply the presented tests to other data types and satellite missions, such as SWARM for example. The development and assessment of new mathematical approaches, as for instance wavelets for regional models instead of spherical harmonic series, could provide an alternative for presenting and filtering the gravity field. Finally, the outcome of the study might also be helpful for explaining some of the differences between current global model retrieval philosophies in the future.

6 APPENDIX

This appendix is a subsidiary arrangement of the difference plots and tables for various filter properties at model level. It visualizes the results which were analysed in section 4.5. In each figure, the differences between reference and filtered model will be presented with respect to the following quantities:

- top left: spherical harmonic (SH) coefficient triangles
- top right: geoid heights, N, in meters *[m]*
- bottom left: gravity anomalies, Δg, in milligal *[mGal]*
- bottom right: gravity gradients, T_{rr}, in Eötvös *[E]*

For each filter property, three different figures are shown: one for the along-track component, the next one for the cross-track component and the last one for the radial component. After these three plots, a table will present the corresponding RMS values for all signal components.
This arrangement of three figures with a summarizing table in the end will be repeated for every single filter design.

Appendix A shows the differences between reference and estimated models for along-track filtering with varying cut-off frequencies f_c in the following order:

- boxcar filter and Butterworth (order 2) filter with $f_c = 1/200\ f_{Ny} = 0.5$ *mHz*
- boxcar filter and Butterworth (order 2) filter with $f_c = 1/20\ f_{Ny} = 5.0$ *mHz*
- boxcar filter and Butterworth (order 2) filter with $f_c = 1/5\ f_{Ny} = 20.0$ *mHz*

Appendix B shows the differences between reference and estimated models for the application of a spherical boxcar and a spherical Butterworth filter (order 2) with a cut-off degree of $l_c = 40$.

Appendix C shows the differences between reference and estimated models for the application of along-track and spherical Butterworth filters with varying filter orders as follows:

- along-track Butterworth filter with $f_c = 1/10\ f_{Ny} = 10.0$ *mHz* and filter order 6
- along-track Butterworth filter with $f_c = 1/10\ f_{Ny} = 10.0$ *mHz* and filter order 12
- spherical Butterworth filter with $l_c = 35$ and filter order 6
- spherical Butterworth filter with $l_c = 35$ and filter order 12

APPENDIX A: VARIATION OF CUT-OFF FREQUENCY FOR ALONG-TRACK FILTERING

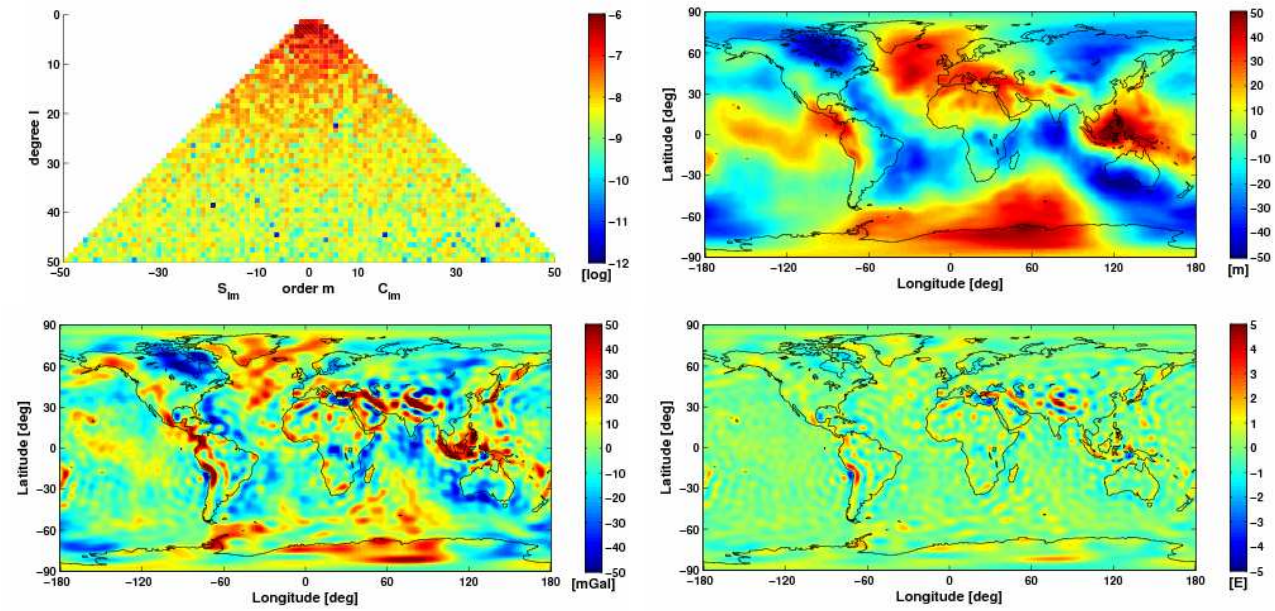

Figure 6.1: Along-track boxcar filtering of V_{xx} with cut-off frequency 1/200 of Nyquist frequency at model level

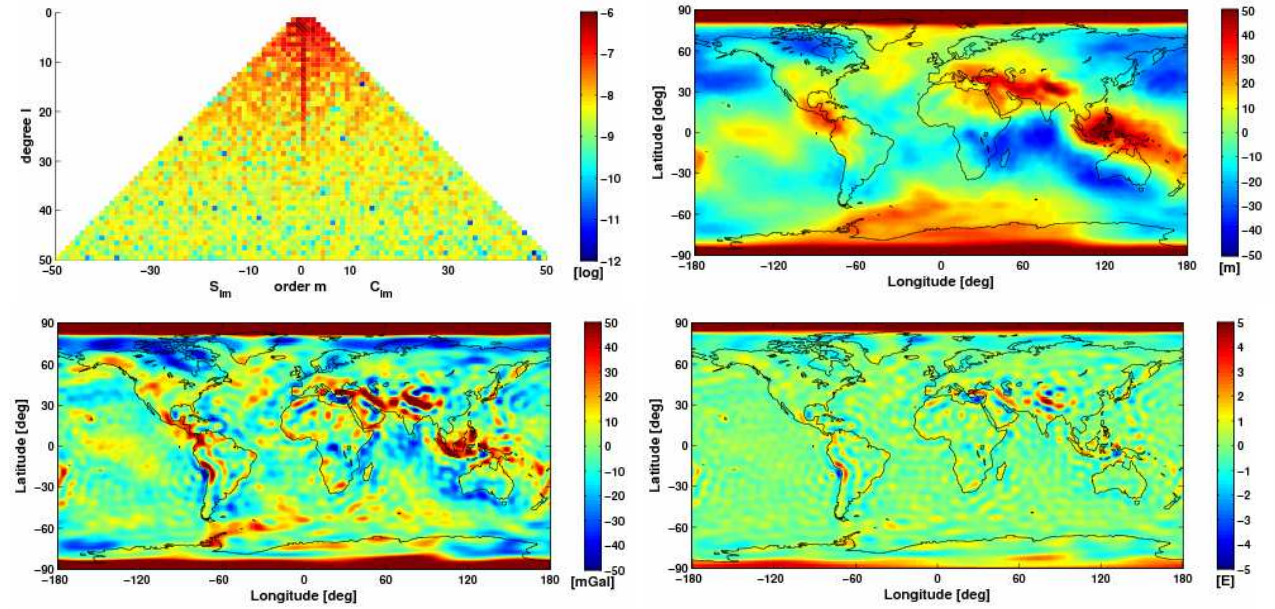

Figure 6.2: Along-track boxcar filtering of V_{yy} with cut-off frequency 1/200 of Nyquist frequency at model level

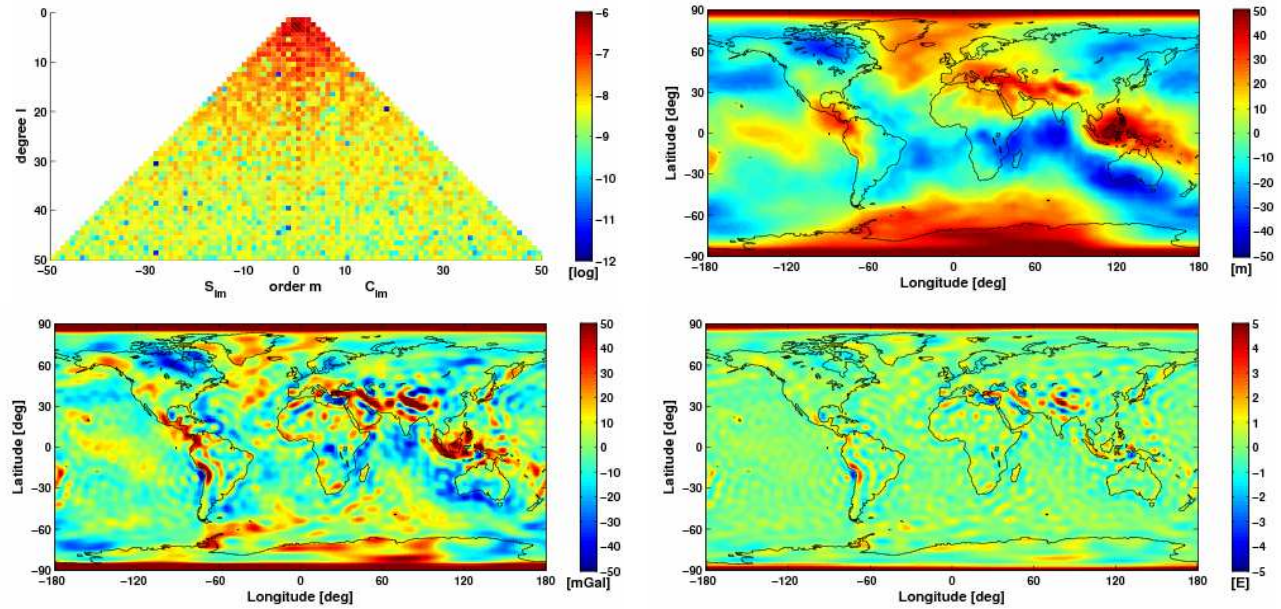

Figure 6.3: Along-track boxcar filtering of V_{zz} with cut-off frequency 1/200 of Nyquist frequency at model level

Table 6.1: RMS values for along-track boxcar filtering with cut-off frequency 1/200 of Nyquist frequency

signal components	RMS of ΔN [m]	RMS of $\Delta(\Delta g)$ [mGal]	RMS of ΔT_{rr} [E]
along-track V_{xx}	4.186	3.534	0.176
cross-track V_{yy}	8.979	10.628	0.298
radial V_{zz}	4.382	3.283	0.186

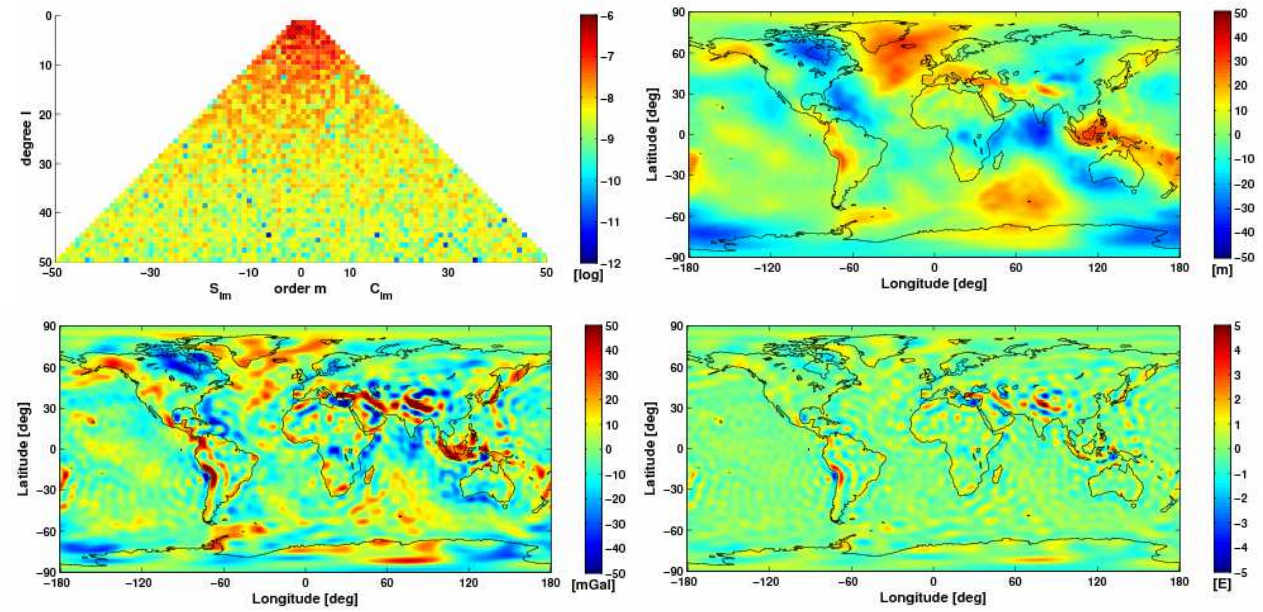

Figure 6.4: Along-track Butterworth filtering (order 2) of V_{xx} with cut-off frequency 1/200 of f_{Ny} at model level

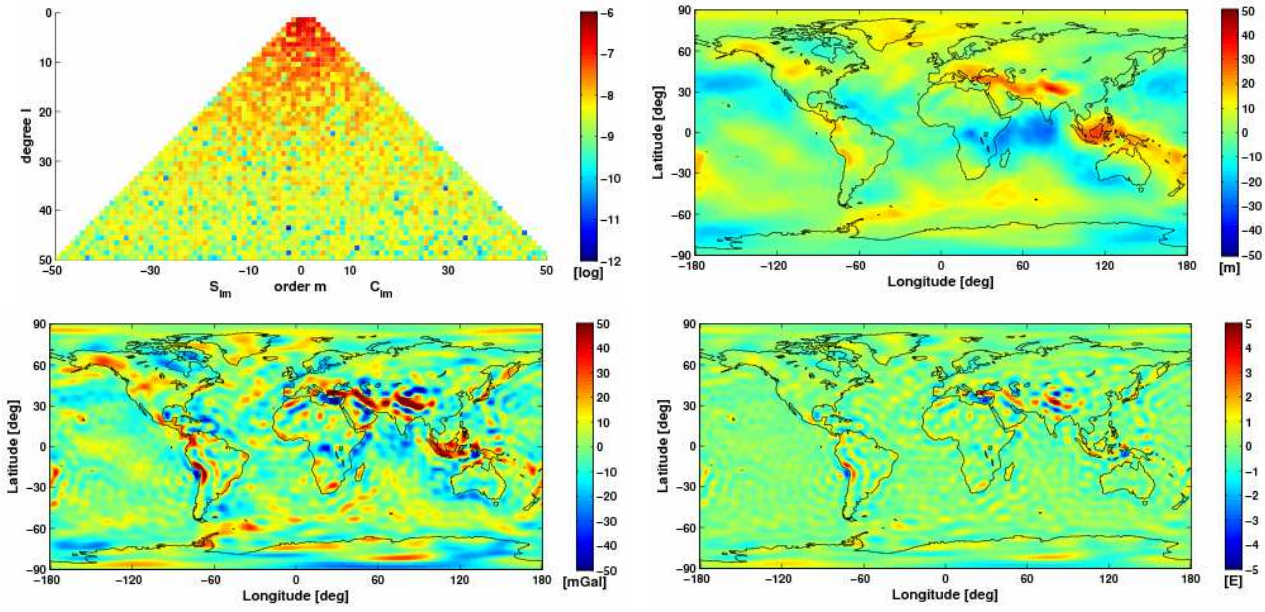

Figure 6.5: Along-track Butterworth filtering (order 2) of V_{yy} with cut-off frequency 1/200 of f_{Ny} at model level

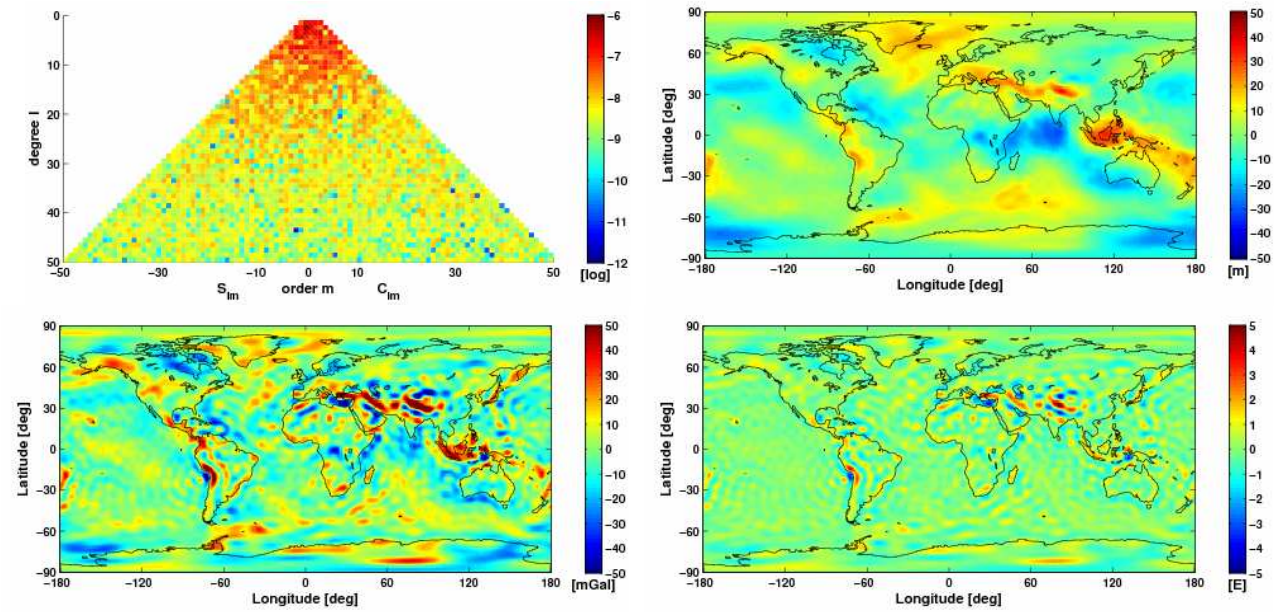

Figure 6.6: Along-track Butterworth filtering (order 2) of V_{zz} with cut-off frequency 1/200 of f_{Ny} at model level

Table 6.2: RMS values for along-track Butterworth filtering (order 2) with cut-off frequency 1/200 of Nyquist frequency

signal components	RMS of ΔN [m]	RMS of $\Delta(\Delta g)$ [mGal]	RMS of ΔT_{rr} [E]
along-track V_{xx}	2.060	2.792	0.172
cross-track V_{yy}	1.896	2.627	0.162
radial V_{zz}	1.790	2.627	0.165

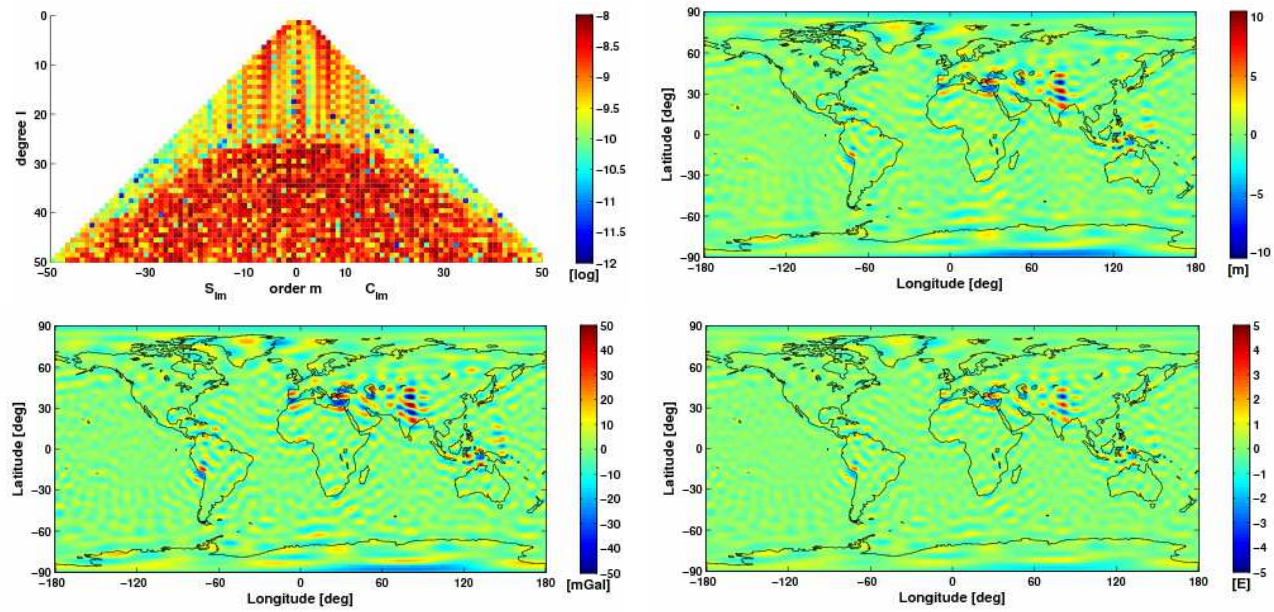

Figure 6.7: Along-track boxcar filtering of V_{xx} with cut-off frequency 1/20 of Nyquist frequency at model level

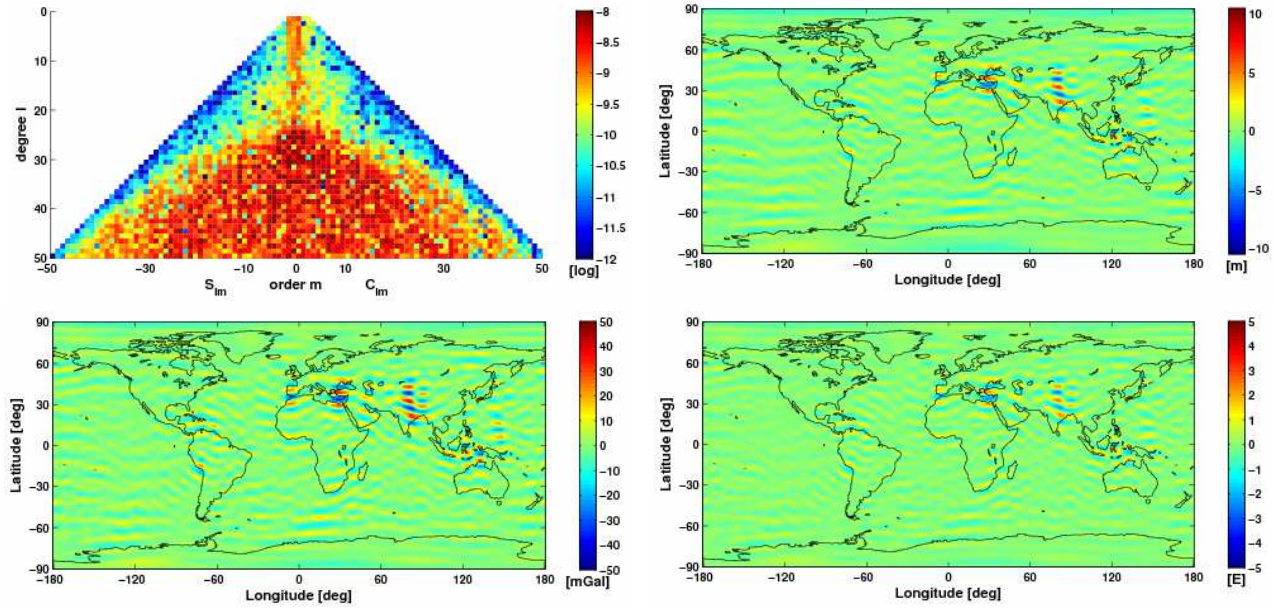

Figure 6.8: Along-track boxcar filtering of V_{yy} with cut-off frequency 1/20 of Nyquist frequency at model level

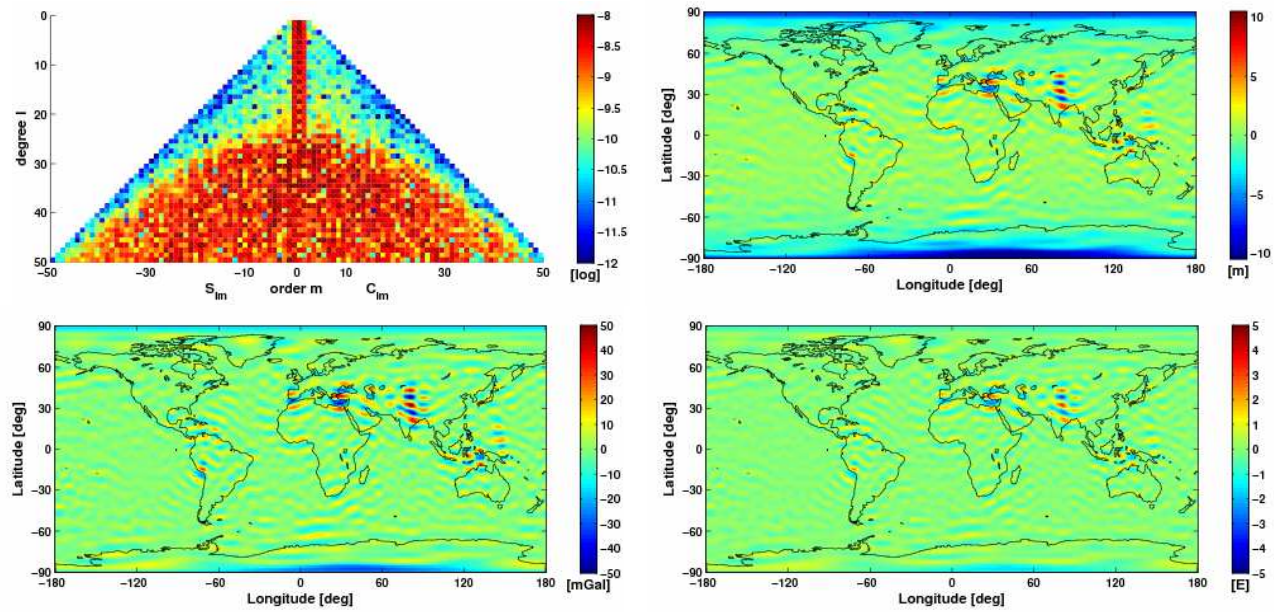

Figure 6.9: Along-track boxcar filtering of V_{zz} with cut-off frequency 1/20 of Nyquist frequency at model level

Table 6.3: RMS values for along-track boxcar filtering with cut-off frequency 1/20 of Nyquist frequency

signal components	RMS of ΔN [m]	RMS of $\Delta(\Delta g)$ [mGal]	RMS of ΔT_{rr} [E]
along-track V_{xx}	0.384	1.961	0.130
cross-track V_{yy}	0.245	1.473	0.105
radial V_{zz}	0.799	1.963	0.122

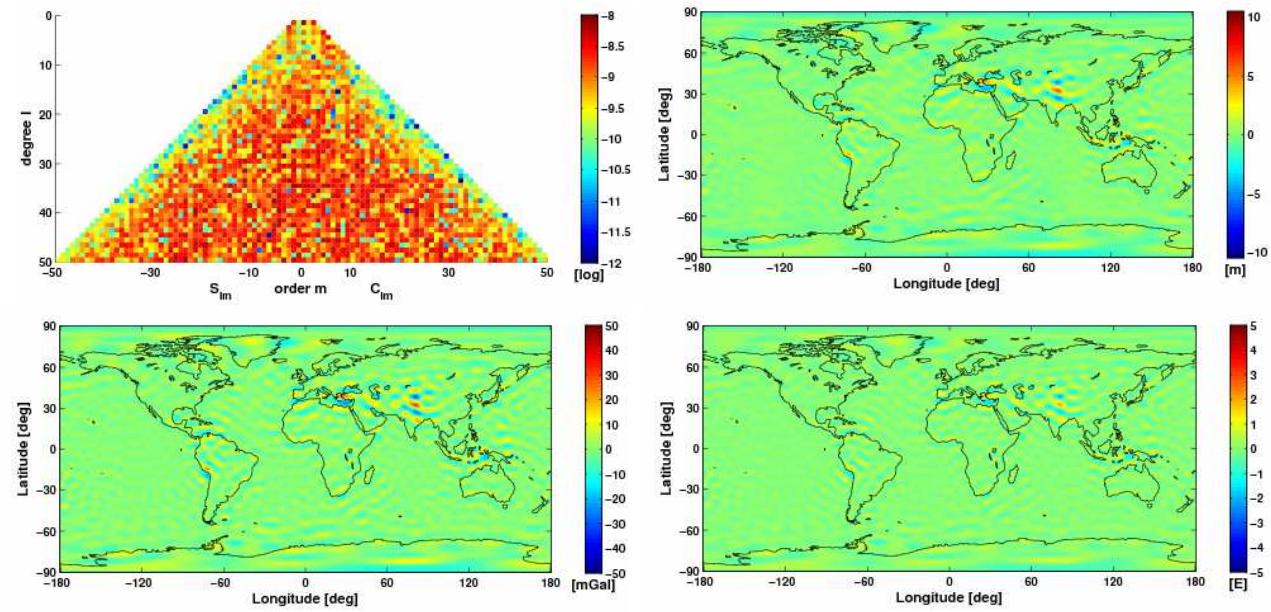

Figure 6.10: Along-track Butterworth filtering (order 2) of V_{xx} with cut-off frequency 1/20 of f_{Ny} at model level

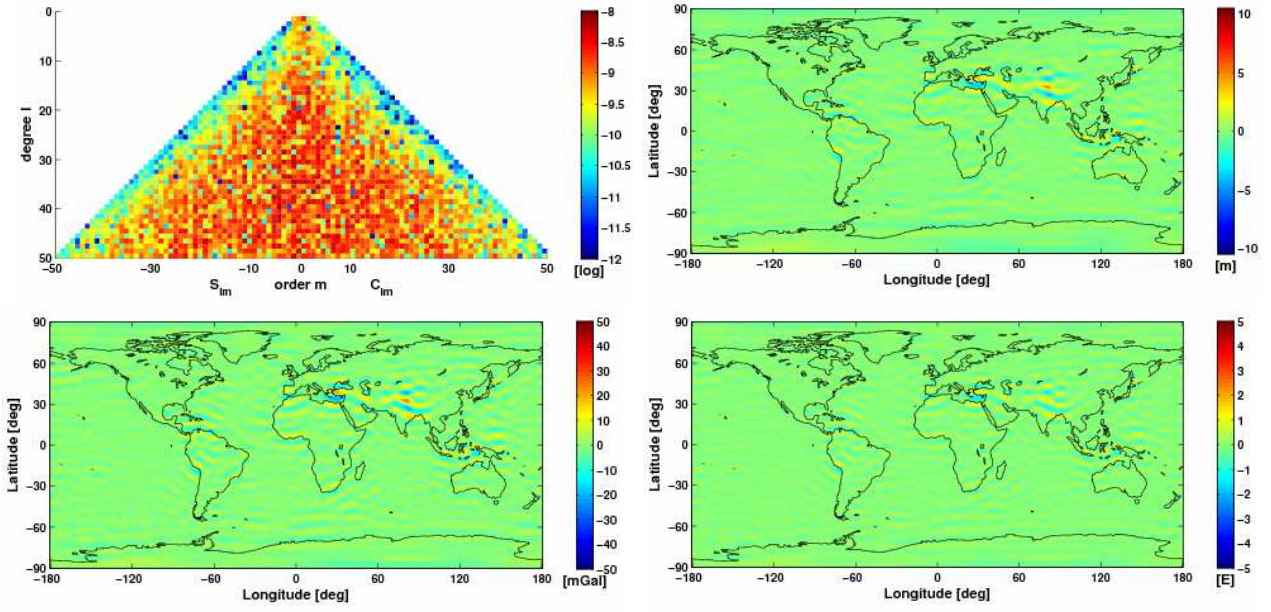

Figure 6.11: Along-track Butterworth filtering (order 2) of V_{yy} with cut-off frequency 1/20 of f_{Ny} at model level

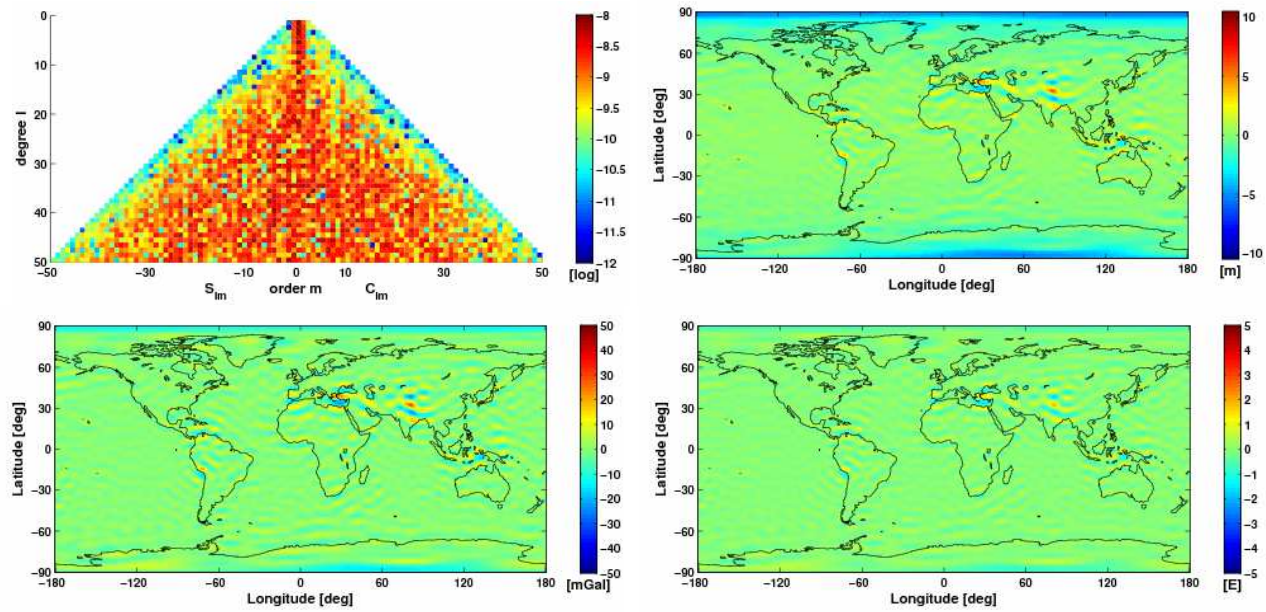

Figure 6.12: Along-track Butterworth filtering (order 2) of V_{zz} with cut-off frequency 1/20 of f_{Ny} at model level

Table 6.4: RMS values for along-track Butterworth filtering (order 2) with cut-off frequency 1/20 of Nyquist frequency

signal components	RMS of ΔN [m]	RMS of $\Delta(\Delta g)$ [mGal]	RMS of ΔT_{rr} [E]
along-track V_{xx}	0.202	1.026	0.070
cross-track V_{yy}	0.157	0.885	0.061
radial V_{zz}	0.438	1.011	0.066

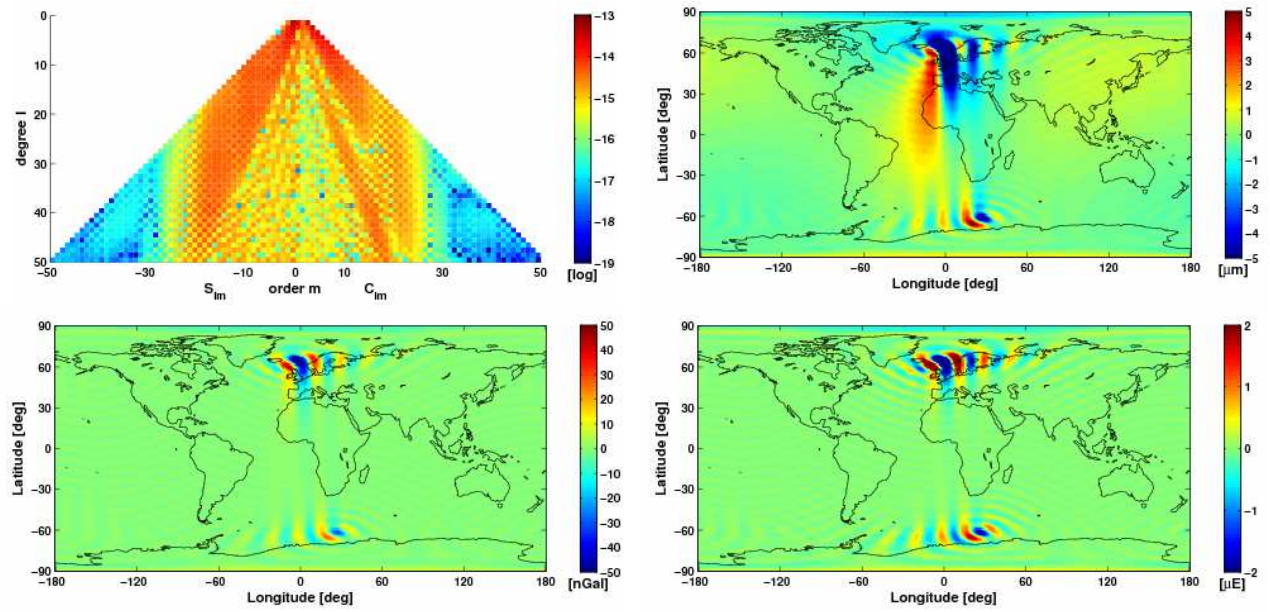

Figure 6.13: Along-track boxcar filtering of V_{xx} with cut-off frequency 1/5 of Nyquist frequency at model level

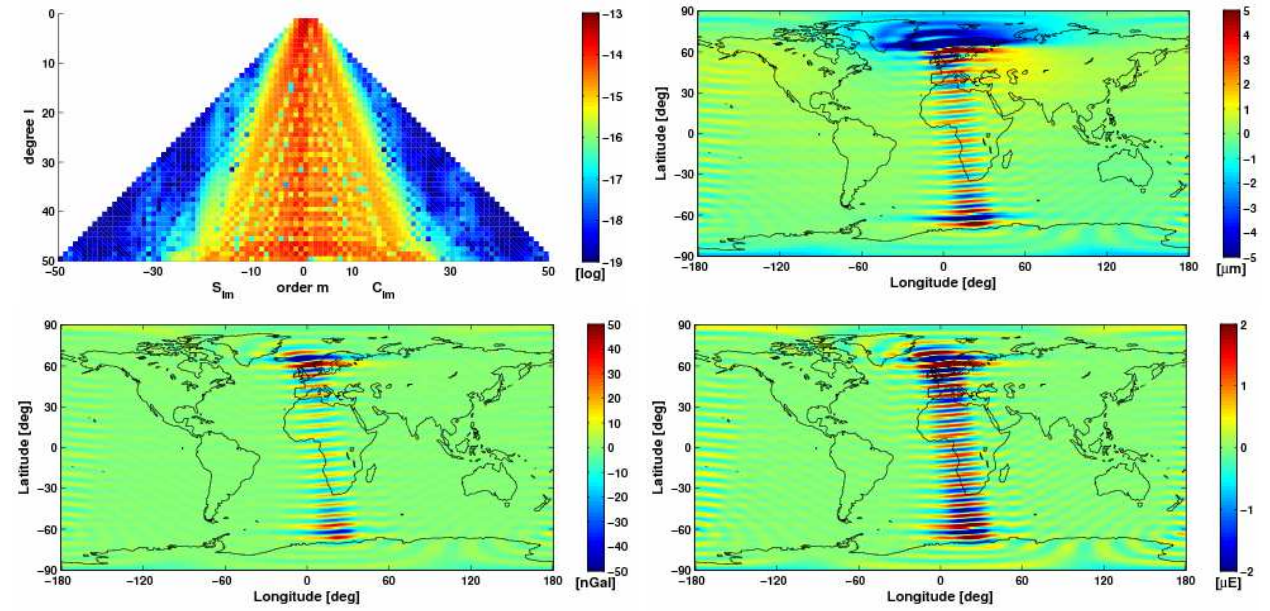

Figure 6.14: Along-track boxcar filtering of V_{yy} with cut-off frequency 1/5 of Nyquist frequency at model level

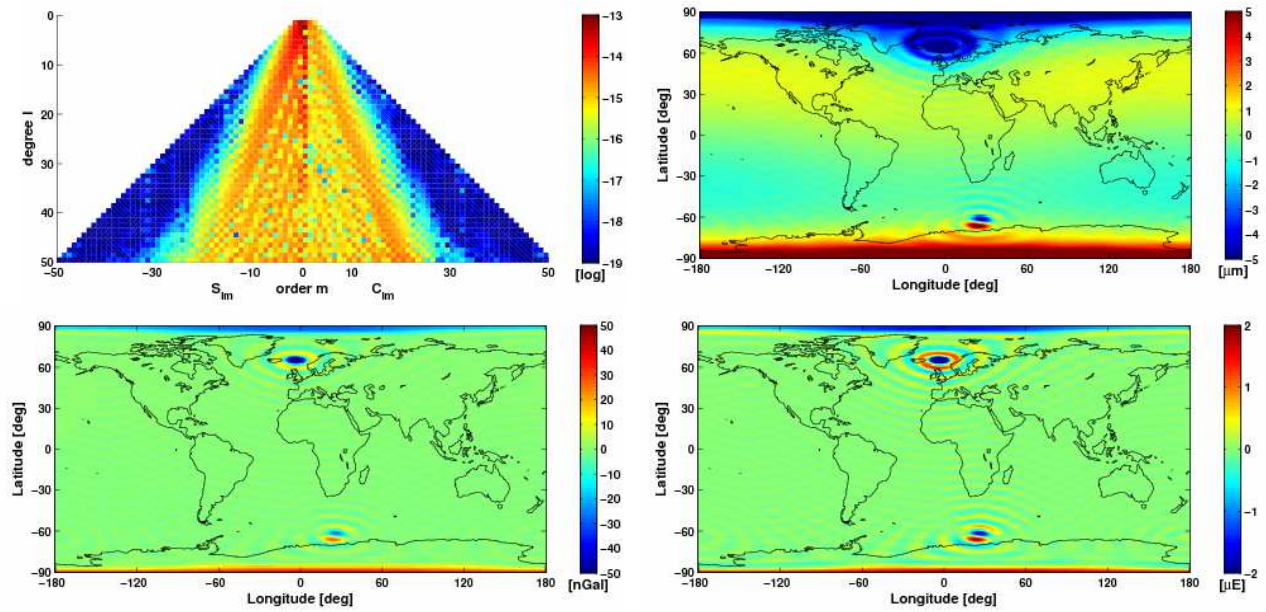

Figure 6.15: Along-track boxcar filtering of V_{zz} with cut-off frequency 1/5 of Nyquist frequency at model level

Table 6.5: RMS values for along-track boxcar filtering with cut-off frequency 1/5 of Nyquist frequency

signal components	RMS of ΔN [µm]	RMS of $\Delta(\Delta g)$ [nGal]	RMS of ΔT_{rr} [µE]
along-track V_{xx}	0.687	2.407	0.152
cross-track V_{yy}	0.890	4.225	0.309
radial V_{zz}	0.493	1.492	0.094

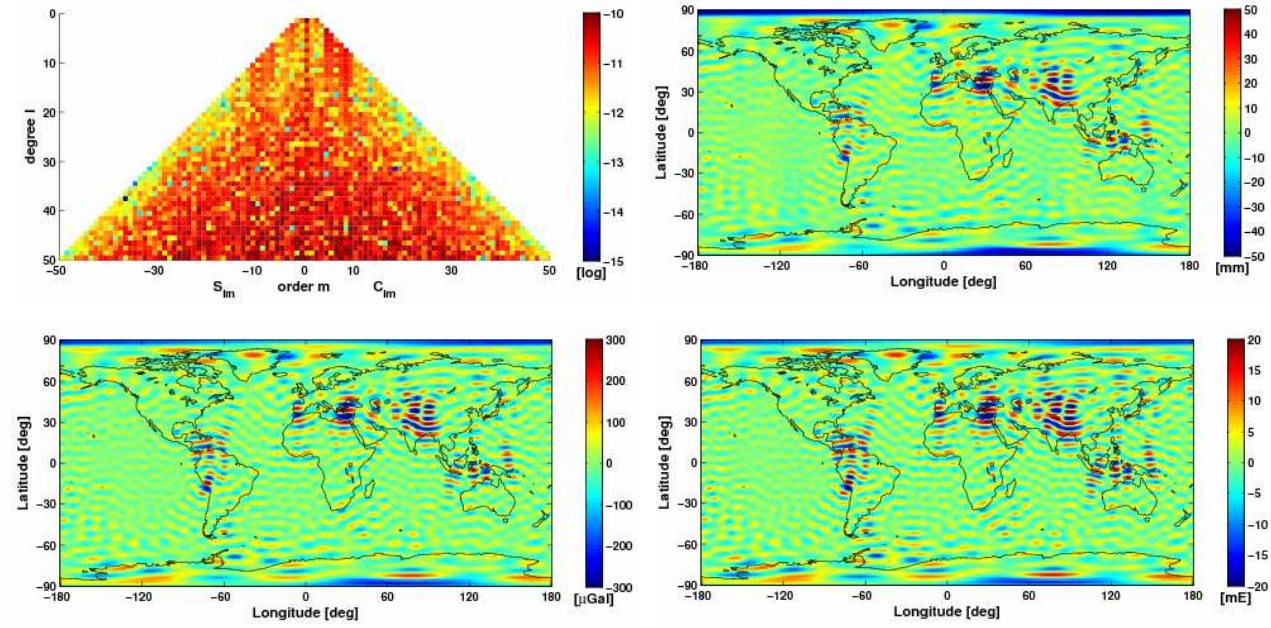

Figure 6.16: Along-track Butterworth filtering (order 2) of V_{xx} with cut-off frequency 1/5 of f_{Ny} at model level

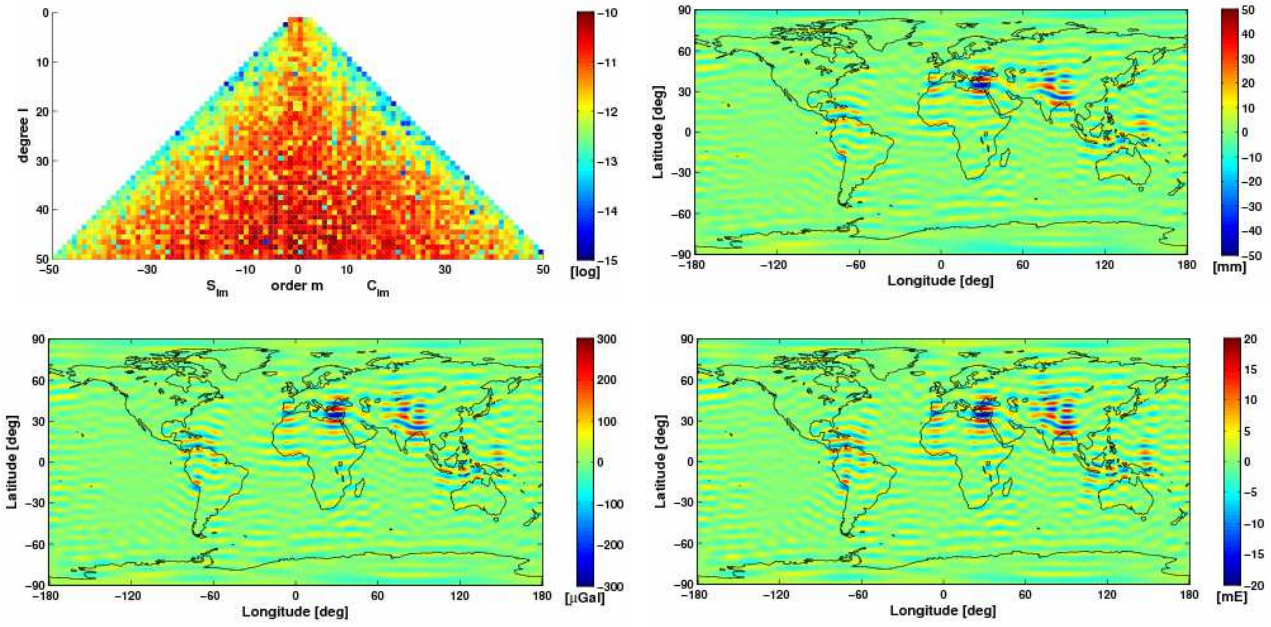

Figure 6.17: Along-track Butterworth filtering (order 2) of V_{yy} with cut-off frequency 1/5 of f_{Ny} at model level

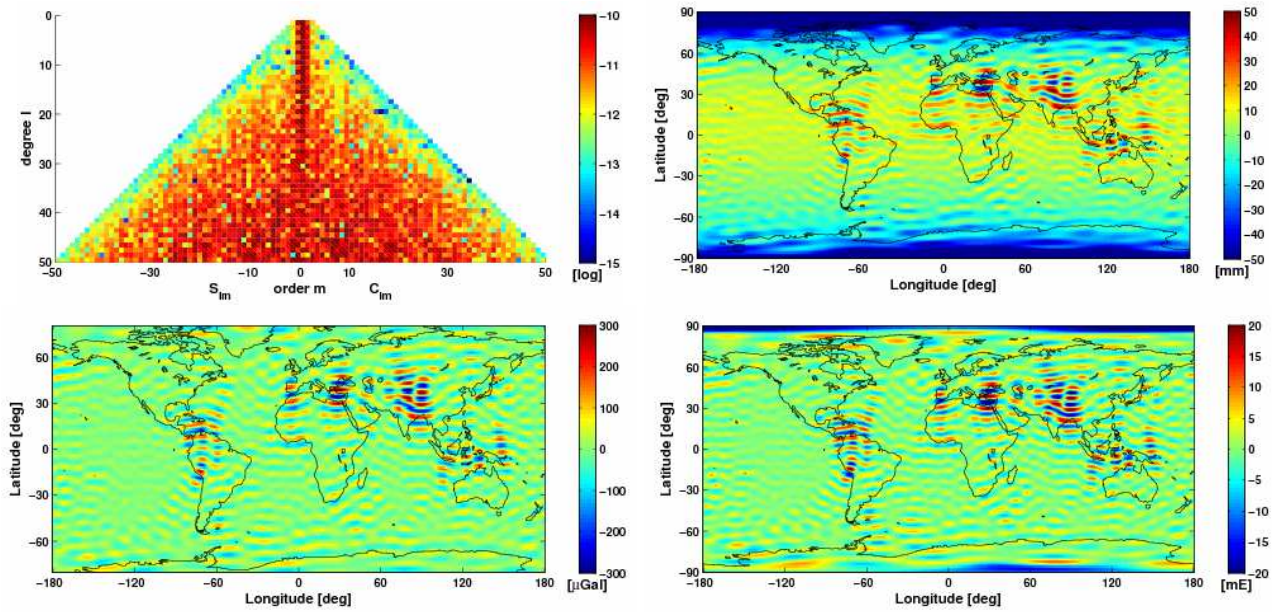

Figure 6.18: Along-track Butterworth filtering (order 2) of V_{zz} with cut-off frequency 1/5 of f_{Ny} at model level

Table 6.6: RMS values for along-track Butterworth filtering (order 2) with cut-off frequency 1/5 of Nyquist frequency

signal components	RMS of ΔN [mm]	RMS of $\Delta(\Delta g)$ [µGal]	RMS of ΔT_{rr} [mE]
along-track V_{xx}	2.655	14.957	1.131
cross-track V_{yy}	1.974	12.632	0.945
radial V_{zz}	13.001	17.246	1.066

APPENDIX B: VARIATION OF CUT-OFF DEGREE FOR SPHERICAL FILTERING

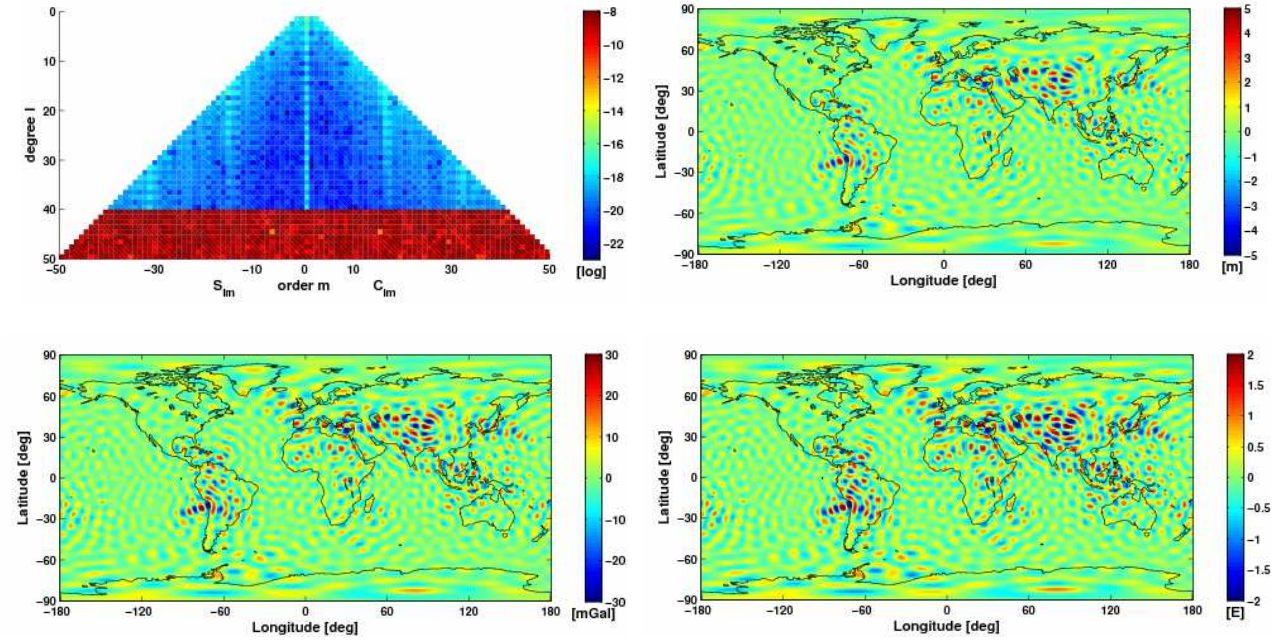

Figure 6.19: Spherical boxcar filtering (V_{xx}) with cut-off degree of $l_c=40$ at model level

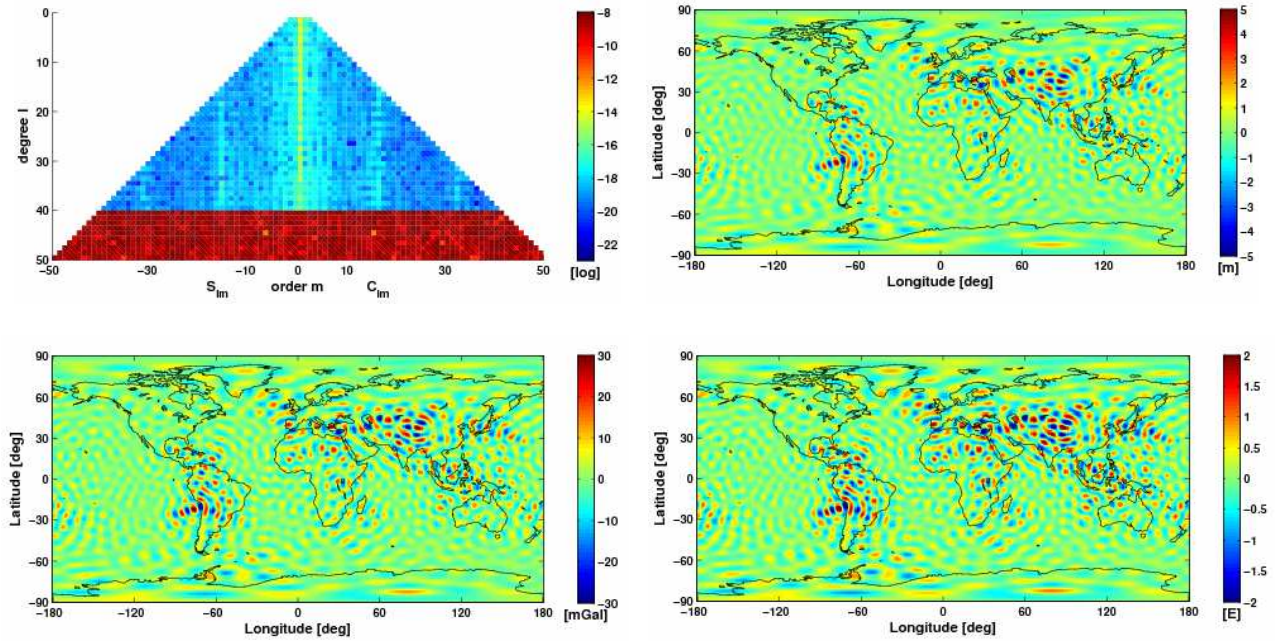

Figure 6.20: Spherical boxcar filtering (V_{yy}) with cut-off degree of $l_c=40$ at model level

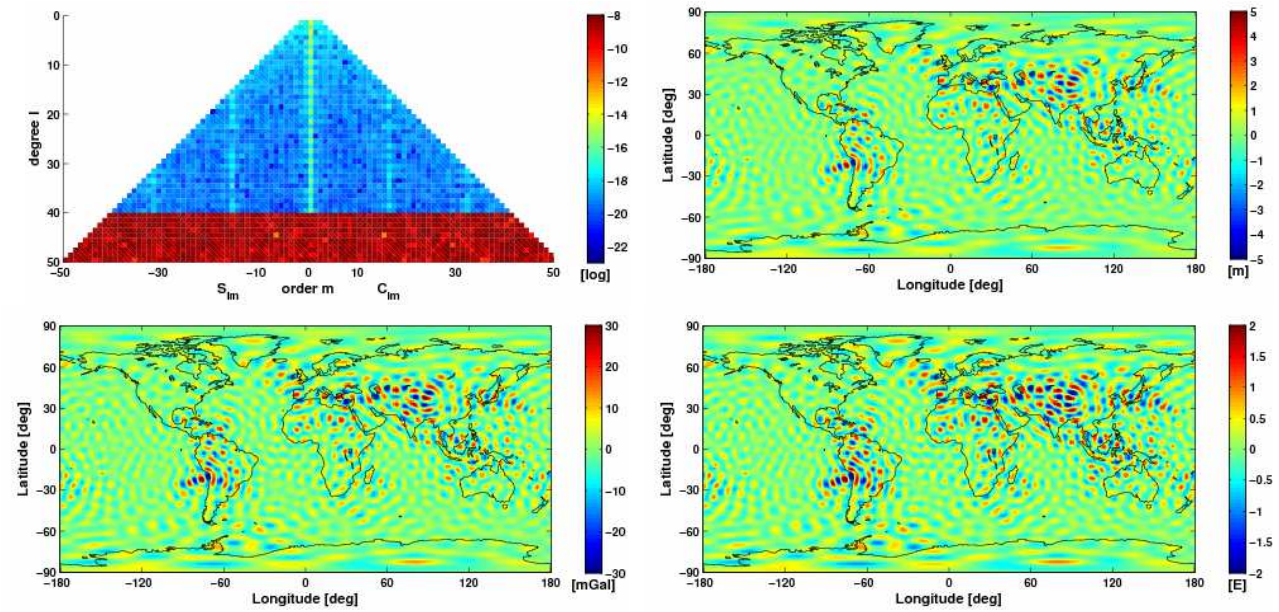

Figure 6.21: Spherical boxcar filtering (V_{zz}) with cut-off degree of $l_c=40$ at model level

Table 6.7: RMS values for spherical boxcar filtering with cut-off degree of $l_c=40$

signal components	RMS of ΔN [cm]	RMS of $\Delta(\Delta g)$ [mGal]	RMS of ΔT_{rr} [E]
along-track V_{xx}	18.753	1.268	0.098
cross-track V_{yy}	18.753	1.268	0.098
radial V_{zz}	18.753	1.268	0.098

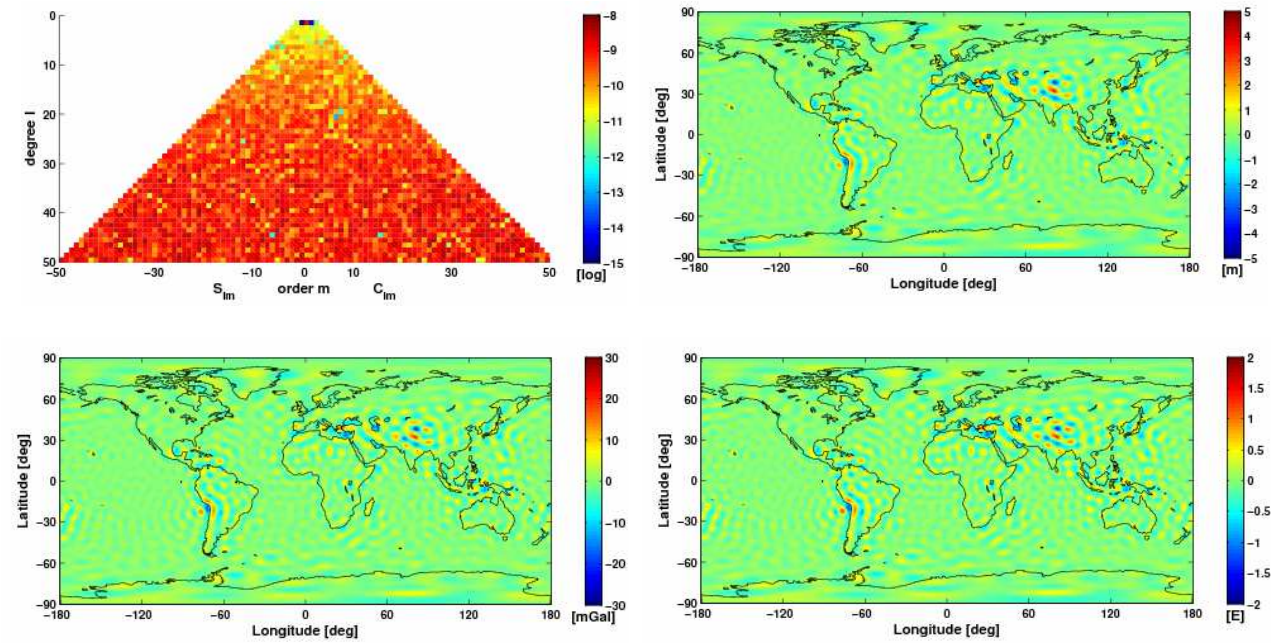

Figure 6.22: Spherical Butterworth filtering (order 2, V_{xx}) with cut-off degree $l_c=40$ at model level

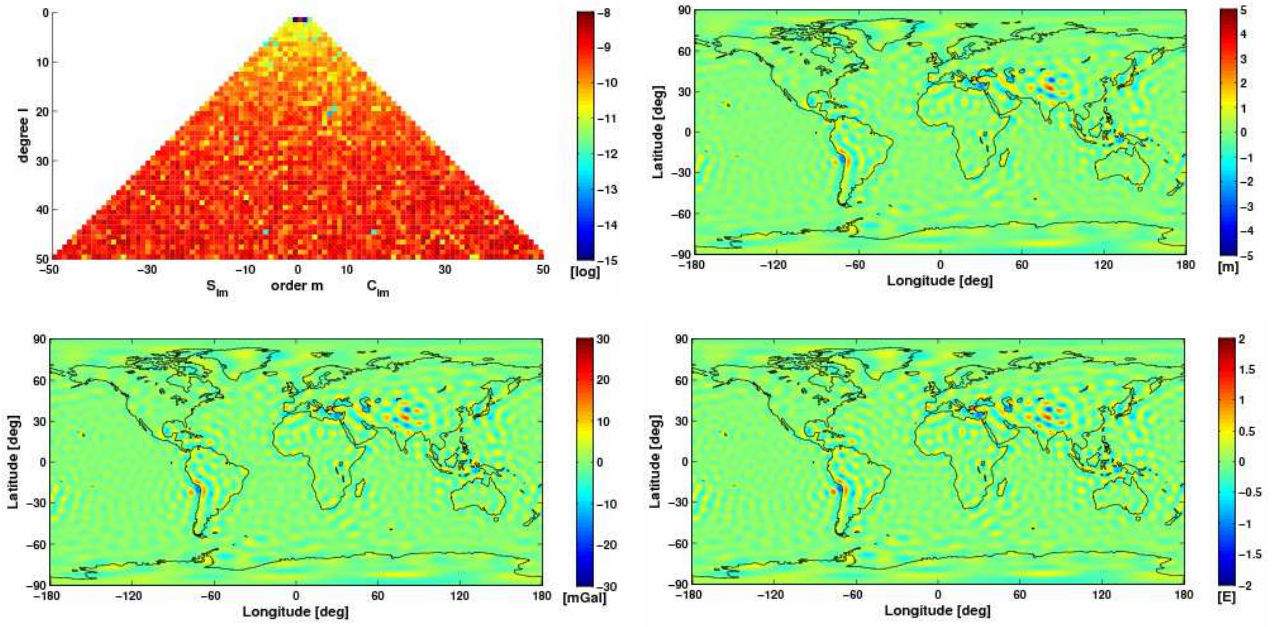

Figure 6.23: Spherical Butterworth filtering (order 2, V_{yy}) with cut-off degree $l_c=40$ at model level

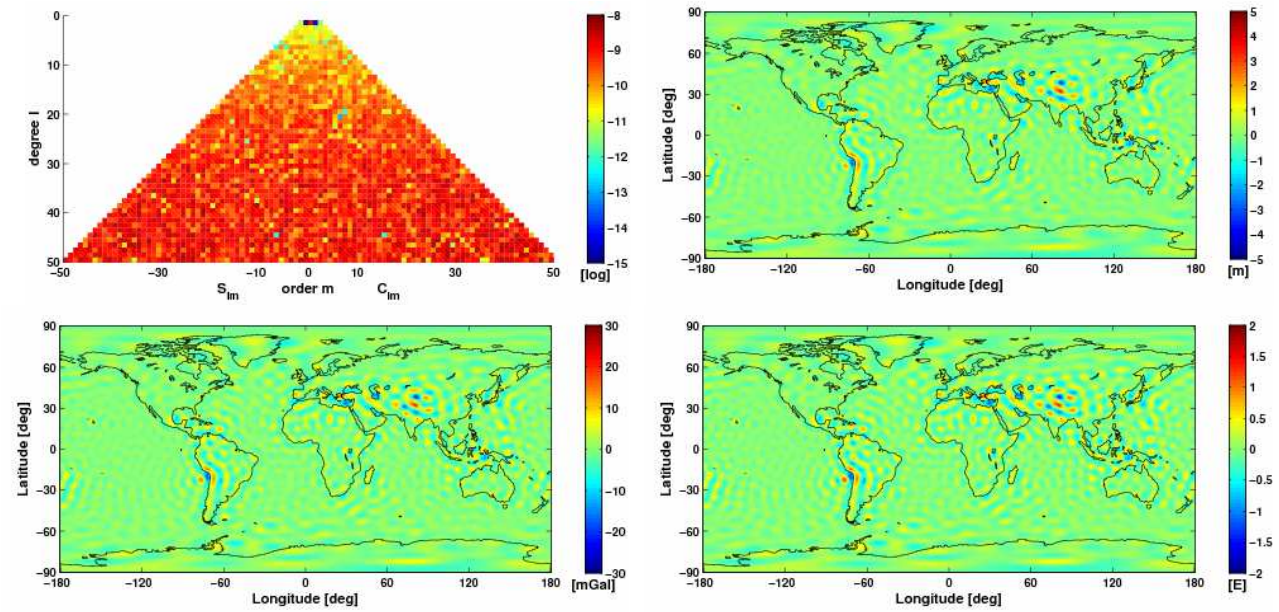

Figure 6.24: Spherical Butterworth filtering (order 2, V_{zz}) with cut-off degree $l_c=40$ at model level

Table 6.8: RMS values for spherical Butterworth filtering (order 2) with cut-off degree of $l_c=40$

signal components	RMS of ΔN [cm]	RMS of $\Delta(\Delta g)$ [mGal]	RMS of ΔT_{rr} [E]
along-track V_{xx}	11.288	0.663	0.047
cross-track V_{yy}	11.288	0.663	0.047
radial V_{zz}	11.288	0.663	0.047

APPENDIX C: VARIATION OF ORDER OF BUTTERWORTH FILTER

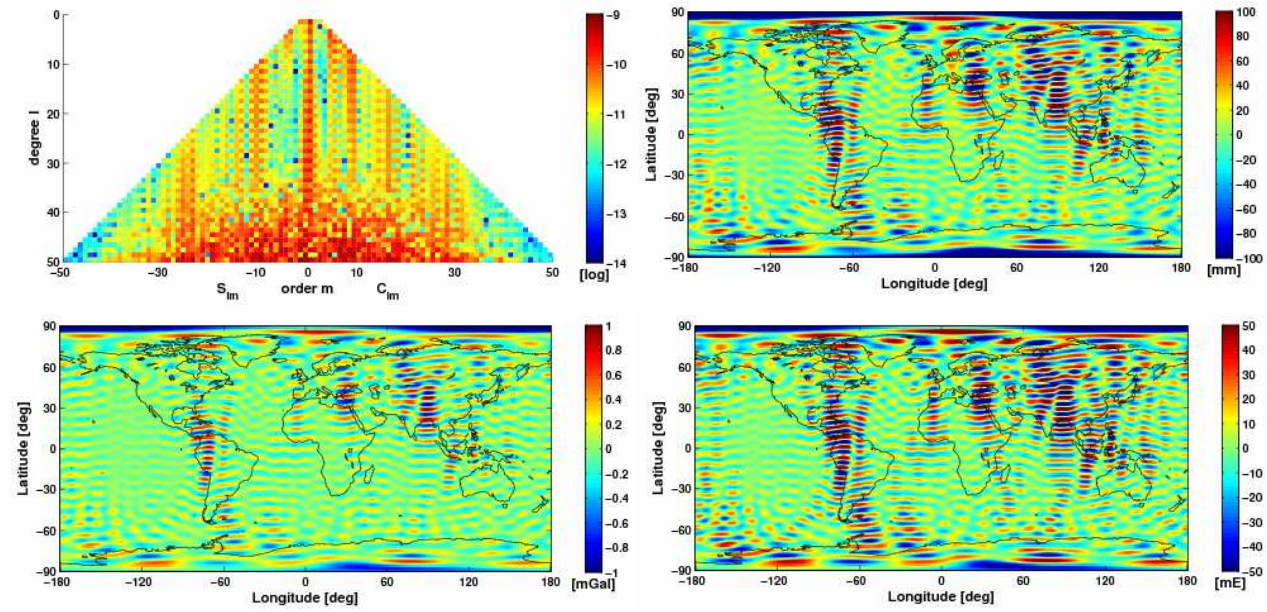

Figure 6.25: Along-track Butterworth filtering (order 6) of V_{xx} with cut-off frequency 1/10 of f_{Ny} at model level

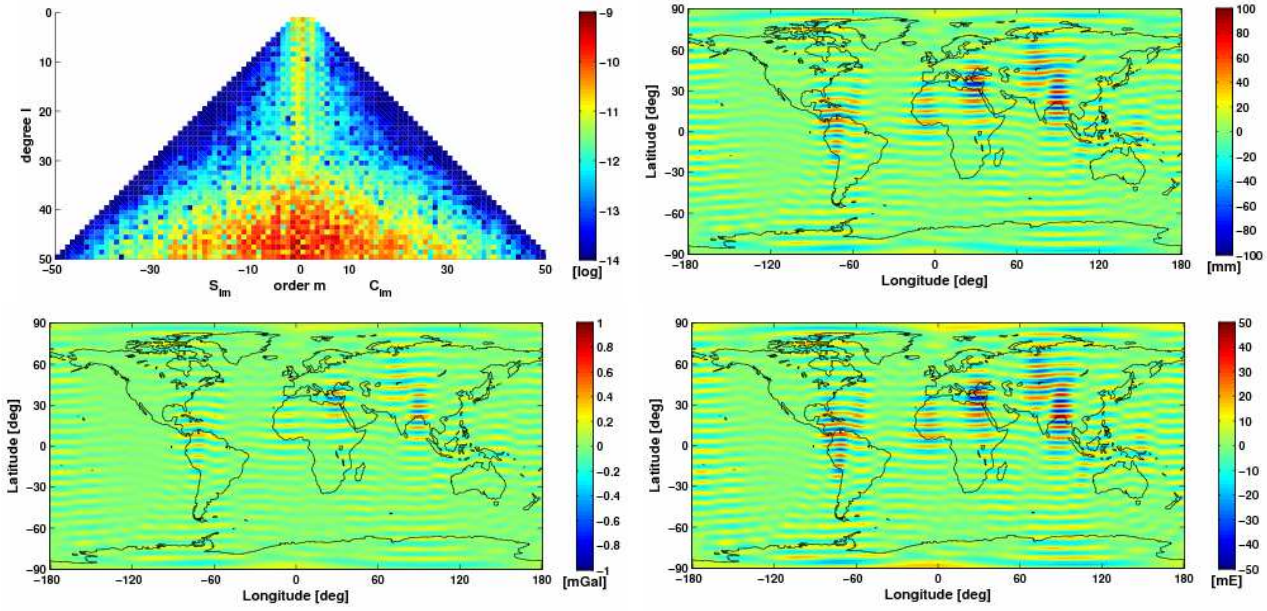

Figure 6.26: Along-track Butterworth filtering (order 6) of V_{yy} with cut-off frequency 1/10 of f_{Ny} at model level

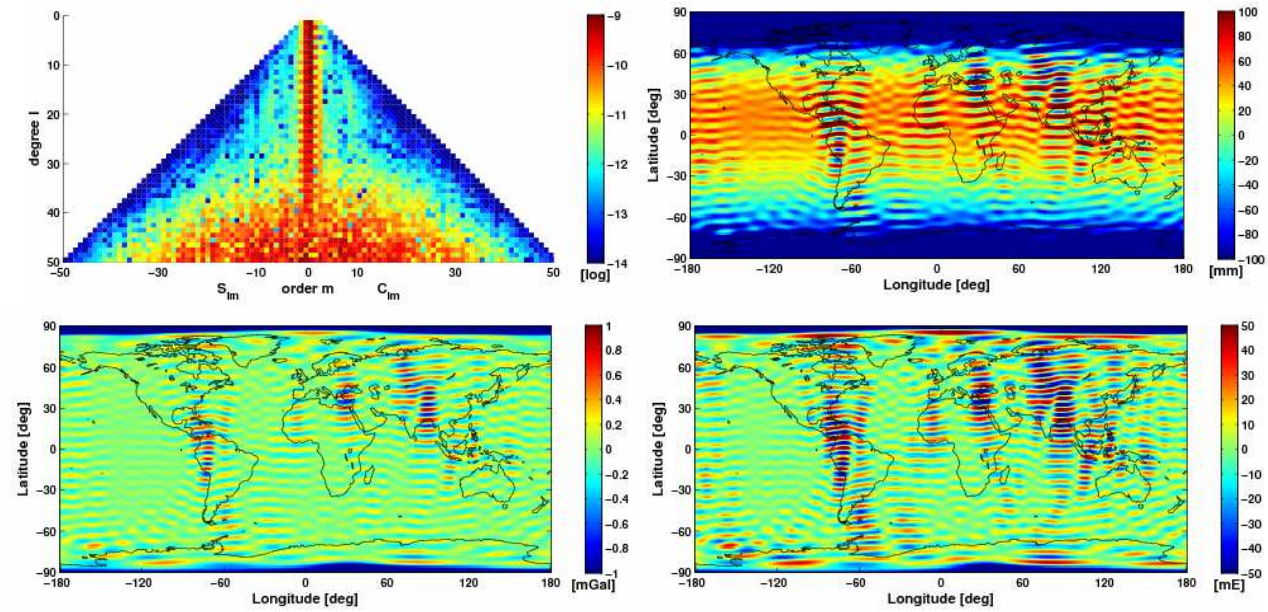

Figure 6.27: Along-track Butterworth filtering (order 6) of V_{zz} with cut-off frequency 1/10 of f_{Ny} at model level

Table 6.9: RMS values for along-track Butterworth filtering (order 6) with cut-off frequency 1/10 of Nyquist frequency

signal components	RMS of ΔN [mm]	RMS of $\Delta(\Delta g)$ [µGal]	RMS of ΔT_{rr} [mE]
along-track V_{xx}	10.220	53.563	4.297
cross-track V_{yy}	5.178	36.016	2.858
radial V_{zz}	85.113	109.088	5.035

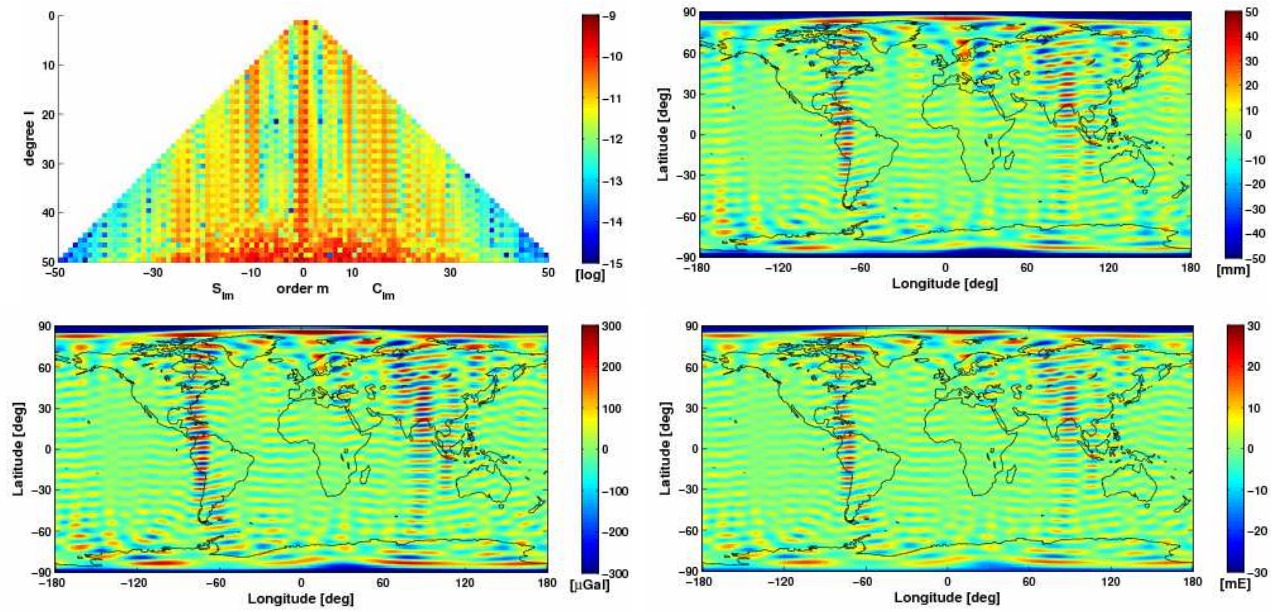

Figure 6.28: Along-track Butterworth filtering (order 12) of V_{xx} with cut-off frequency 1/10 of f_{Ny} at model level

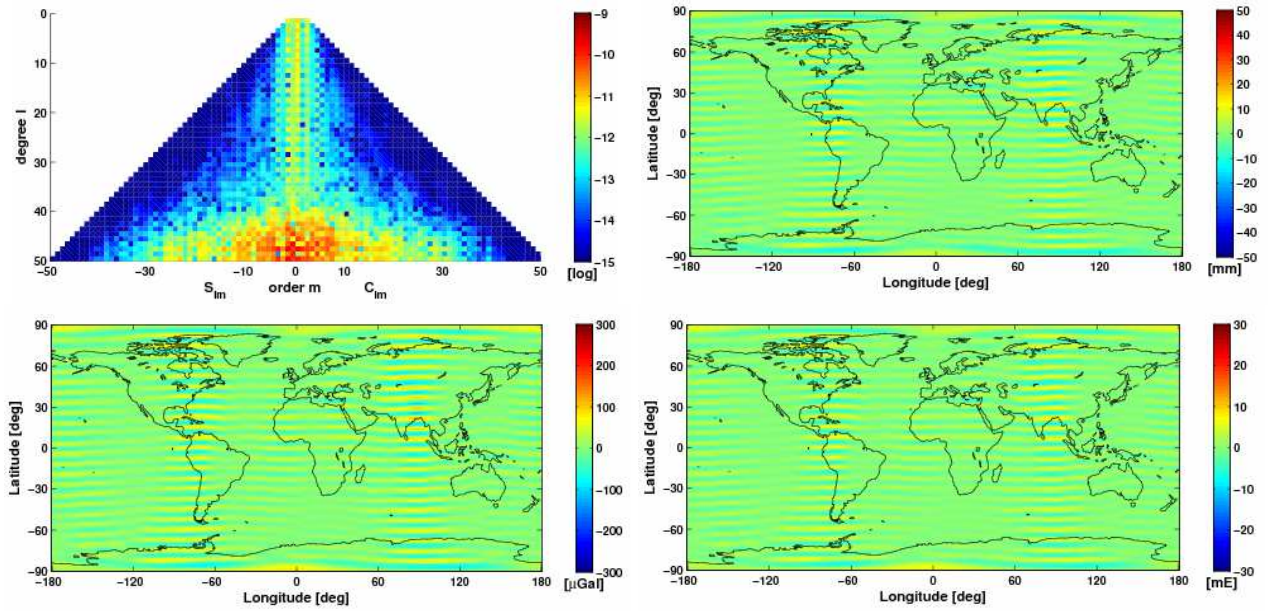

Figure 6.29: Along-track Butterworth filtering (order 12) of V_{yy} with cut-off frequency 1/10 of f_{Ny} at model level

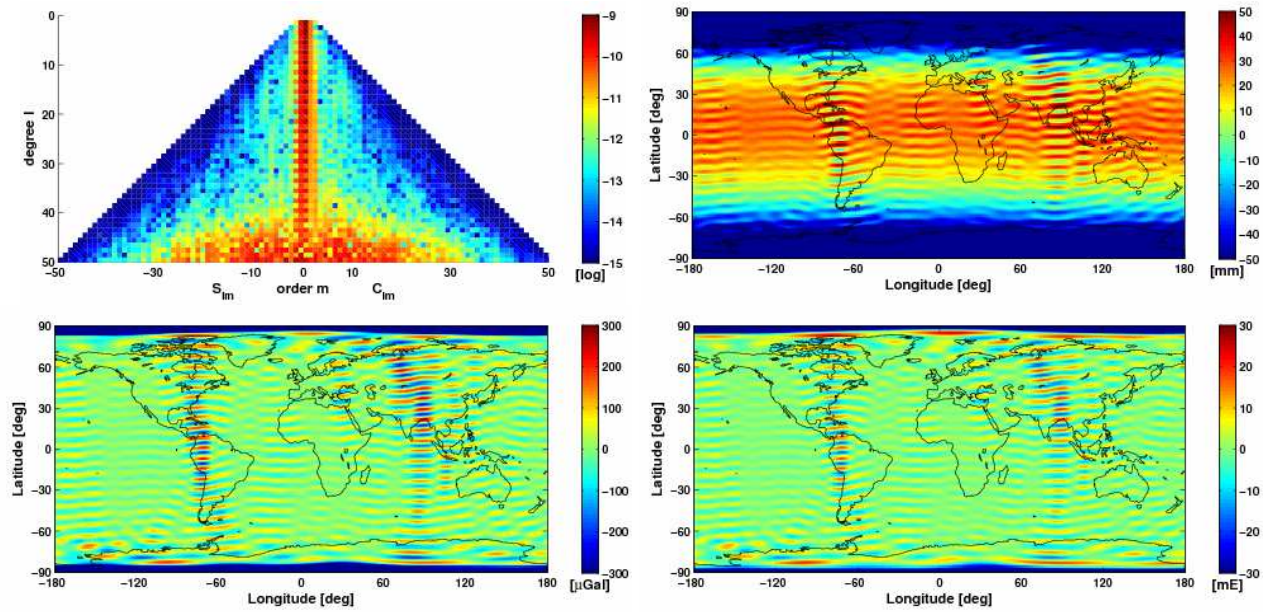

Figure 6.30: Along-track Butterworth filtering (order 12) of V_{zz} with cut-off frequency 1/10 of f_{Ny} at model level

Table 6.10: RMS values for along-track Butterworth filtering (order 12) with cut-off frequency 1/10 of Nyquist frequency

signal components	RMS of ΔN [mm]	RMS of $\Delta(\Delta g)$ [µGal]	RMS of ΔT_{rr} [mE]
along-track V_{xx}	5.153	20.495	1.428
cross-track V_{yy}	1.460	10.392	0.841
radial V_{zz}	51.140	60.129	2.514

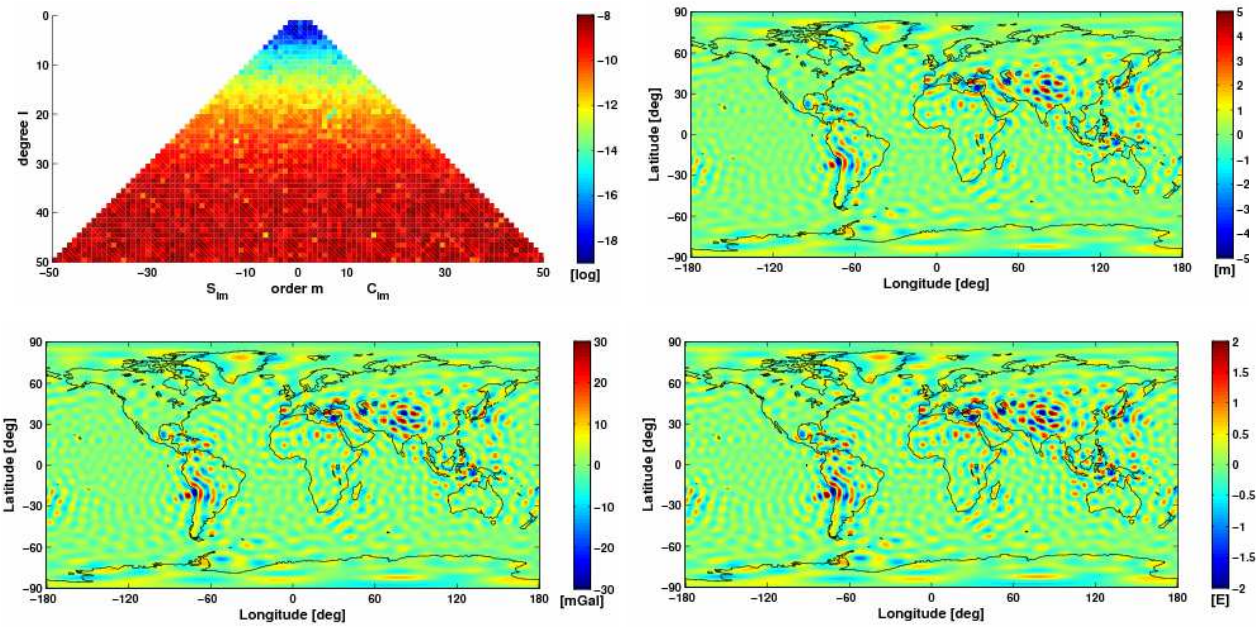

Figure 6.31: Spherical Butterworth filtering (order 6, V_{xx}) with cut-off degree $l_c=35$ at model level

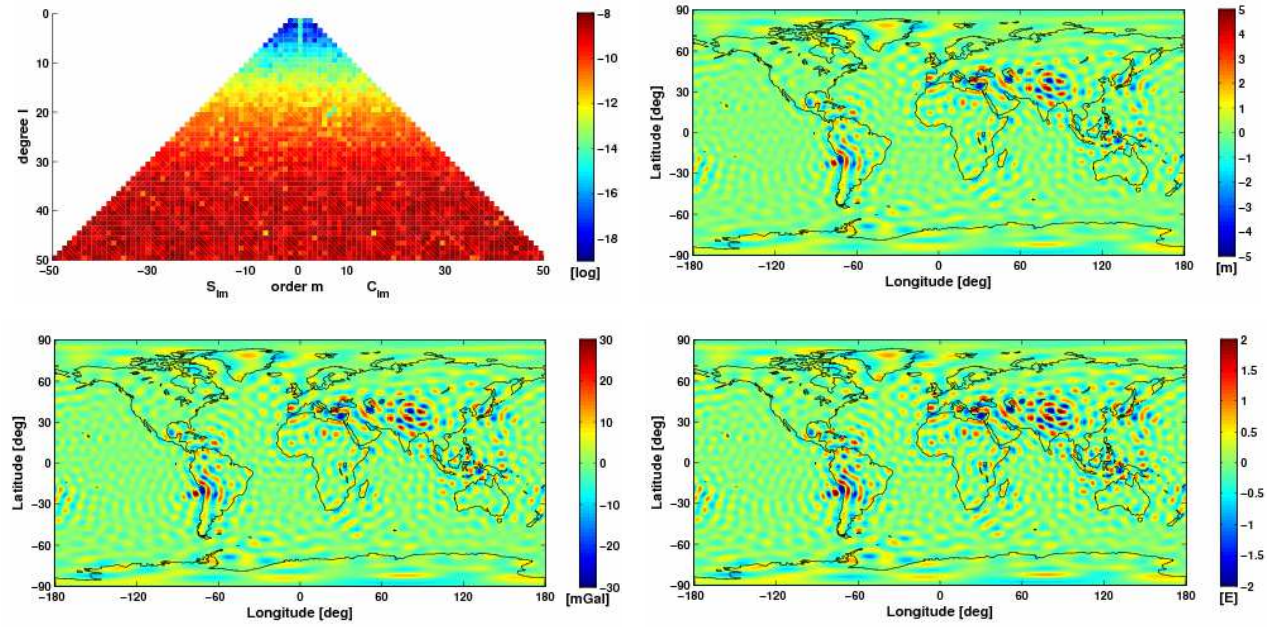

Figure 6.32: Spherical Butterworth filtering (order 6, V_{yy}) with cut-off degree $l_c=35$ at model level

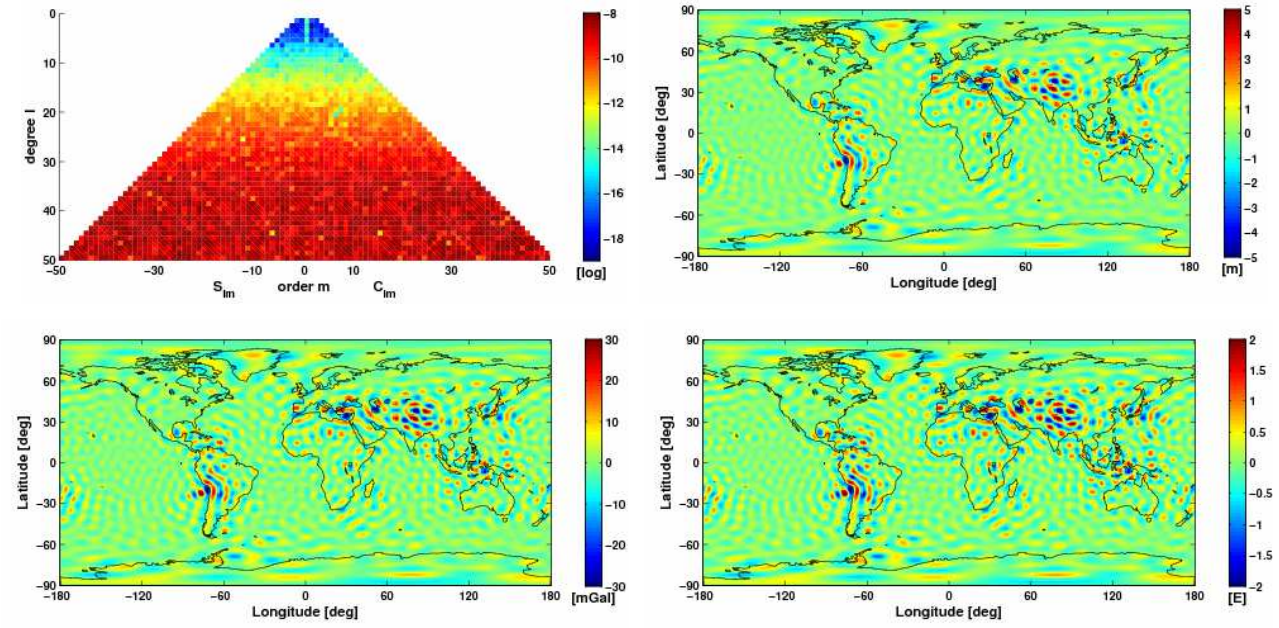

Figure 6.33: Spherical Butterworth filtering (order 6, V_{zz}) with cut-off degree $l_c=35$ at model level

Table 6.11: RMS values for spherical Butterworth filtering (order 6) with cut-off degree of $l_c=35$

signal components	RMS of ΔN [cm]	RMS of $\Delta(\Delta g)$ [mGal]	RMS of ΔT_{rr} [E]
along-track V_{xx}	19.408	1.230	0.091
cross-track V_{yy}	19.408	1.230	0.091
radial V_{zz}	19.408	1.230	0.091

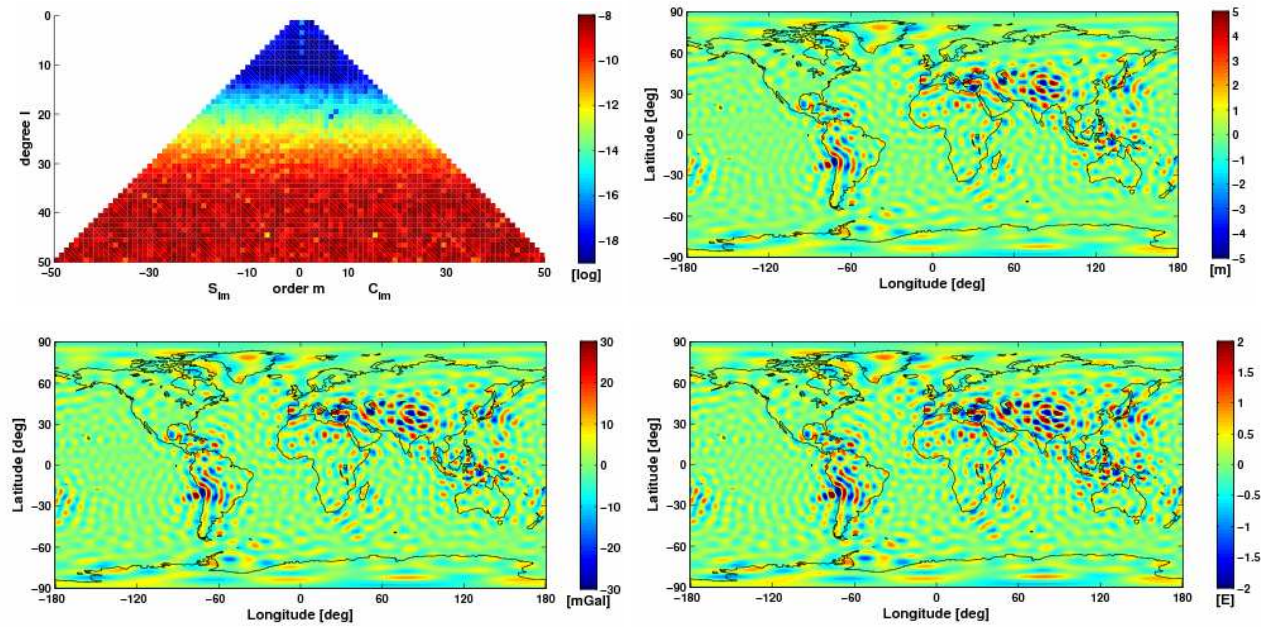

Figure 6.34: Spherical Butterworth filtering (order12, V_{xx}) with cut-off degree $l_c=35$ at model level

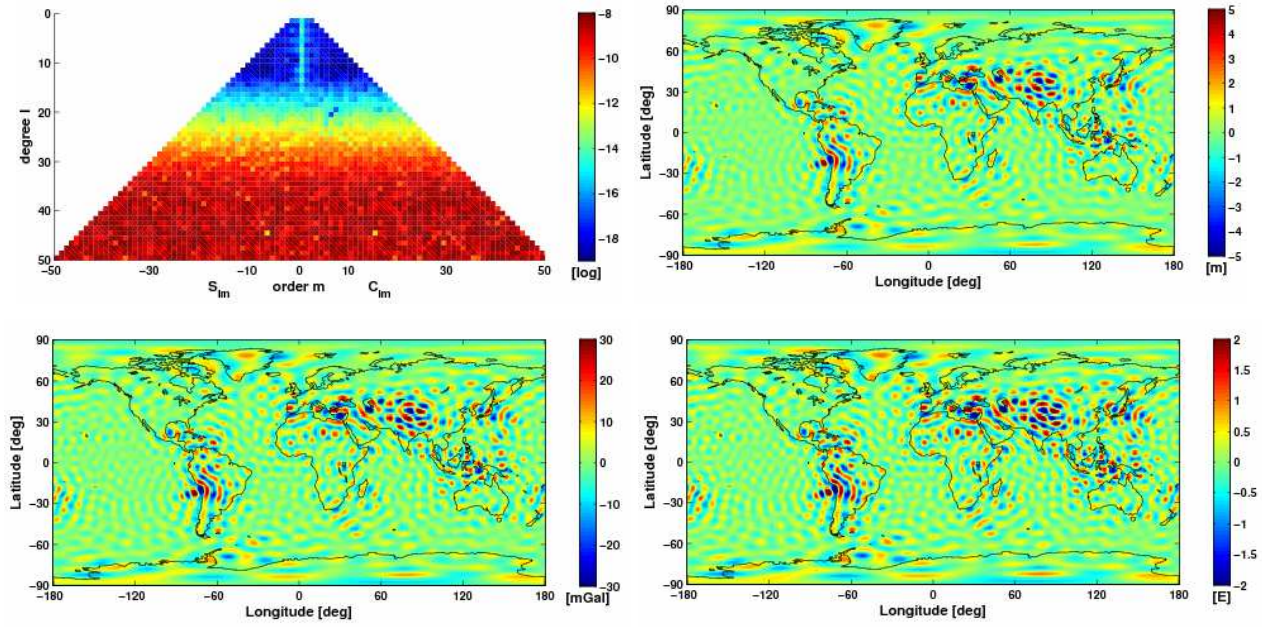

Figure 6.35: Spherical Butterworth filtering (order 12, V_{yy}) with cut-off degree $l_c=35$ at model level

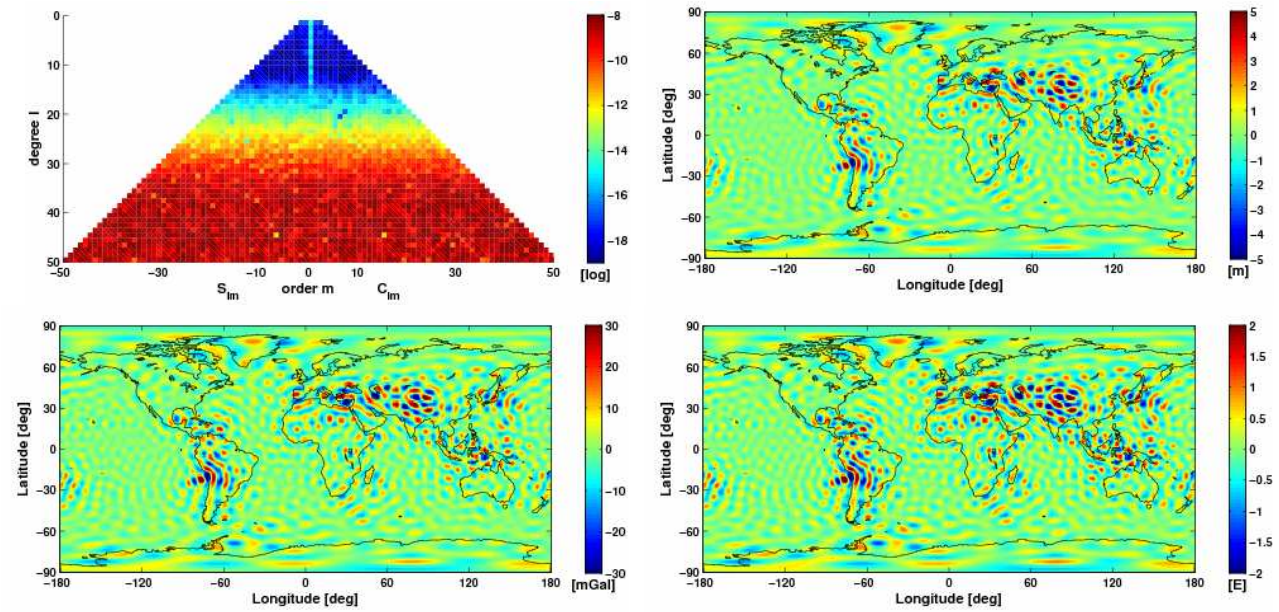

Figure 6.36: Spherical Butterworth filtering (order 12, V_{zz}) with cut-off degree $l_c=35$ at model level

Table 6.12: RMS values for spherical Butterworth filtering (order 12) with cut-off degree of $l_c=35$

signal components	RMS of ΔN [cm]	RMS of $\Delta(\Delta g)$ [mGal]	RMS of ΔT_{rr} [E]
along-track V_{xx}	23.643	1.507	0.111
cross-track V_{yy}	23.643	1.507	0.111
radial V_{zz}	23.643	1.507	0.111

REFERENCES

Drinkwater MR, Haagmans R, Muzi D, Popescu R, Floberghagen R, Kern M, and Fehringer, M (2007): The GOCE Gravity Mission: ESA's first Core Earth Explorer. *Proceedings of the 3rd International GOCE User Workshop*, 6-8 November, 2006, Frascati, Italy, ESA Special Publication, SP-627 (2007) 1-8

ESA (1999). Gravity Field and Steady-State Ocean Circulation Mission. Reports for Mission Selection. The four candidate Earth-explorer core missions, SP-1233(1) (1999)

ESA (2006). ESA's Gravity Mission: GOCE. Brochure BR-209 (2006)

ESA, GOCE Mission Web Site, http://www.esa.int/livingplanet/goce

GFZ Potsdam, CHAMP Mission Web Site, http://op.gfz-potsdam.de/champ

GFZ Potsdam, GRACE Mission Web Site, http://op.gfz-potsdam.de/grace

Hofmann-Wellenhof B, and Moritz H (2005): Physical Geodesy. SpringerWienNewYork, Wien (2005)

Ingle VK, and Proakis JG (2000): Digital Signal Processing using Matlab. Brooks/Cole Publishing Company, Canada (2000)

Johannessen JA, Balmino G, Le Provost C, Rummel R, Sabadini R, Sünkel H, Tscherning CC, Visser P, Woodworth P, Hughes CW, Legrand P, Sneeuw N, Perosanz F, Aguirre-Martinez M, Rebhan H, and Drinkwater MR (2003): The European Gravity Field and Steady-State Ocean Circulation Explorer Satellite Mission: Its Impact on Geophysics. *Surveys in Geophysics* 24 (2003) 339–386

Lynn PA (1982): An Introduction to the Analysis and Processing of Signals. Second Edition, Macmillan Publishers LTD, Hong Kong (1982)

NASA/TP-1998-206861: Lemoine FG, Kenyon SC, Factor JK, Trimmer RG, Pavlis NK, Chinn DS, Cox CM, Klosko SM, Luthcke SB, Torrence MH, Wang YM, Williamson RG, Pavlis EC, Rapp RH and Olson TR (1998).:The Development of the Joint NASA GSFC and NIMA Geopotential Model EGM96, NASA Goddard Space Flight Center, Greenbelt, Maryland, 20771 USA, July 1998.

Oppenheim AV, and Schafer RW with Buck JR (1999): Discrete-Time Signal Processing. Second Edition, Prentice-Hall, Inc.: Upper Saddle River, NJ (1999)

Press WH, Teukolsky SA, Vetterling WT, and Flannery BP (1992): Numerical Recipes in Fortran: The Art of Scientific Computing. Second Edition, Cambridge University Press (1992)

Rummel R, van Gelderen M (1995): Meissl scheme – spectral characteristics of physical geodesy". *manuscripta geodetica* 20 (1995) 379 - 385

Rummel R, Sanso F, Van Gelderen M, Brovelli M, Koop R, Migliaccio F, Schrama EJO, and Sacerdote F (1993): Spherical Harmonic Analysis of Satellite Gradiometry. *Neth. Geodetic Commission*, N. 39 (1993) (New Series)

Wenzel H-G (1995): Spektralanalyse und Digitale Filterung. Unpublished Lecture Notes, Geodetic Institute, University of Karlsruhe, Karlsruhe 1995

Zenner L, (2006): Zeitliche Schwerefeldvariationen aus GRACE und Hydrologiemodellen. Diploma thesis, Institute for Astronomical and Physical Geodesy, Technical University Munich, Munich 2006